Experimental Study of Current-Driven Turbulence During Magnetic Reconnection

by

William Randolph Fox, II

A.B., Princeton University (2001)

Submitted to the Department of Physics
in partial fulfillment of the requirements for the degree of

Doctor of Philosophy

at the

MASSACHUSETTS INSTITUTE OF TECHNOLOGY

June 2009

Author .....
Department of Physics
May 22, 2009

Certified by .....
Miklos Porkolab
Professor of Physics
Thesis Supervisor

Accepted by .....
Thomas Greytak
Professor of Physics, Associate Department Head for Education

Experimental Study of Current-Driven Turbulence During Magnetic Reconnection

by

William Randolph Fox, II

Submitted to the Department of Physics
on May 22, 2009, in partial fulfillment of the
requirements for the degree of
Doctor of Philosophy

Abstract

Magnetic reconnection is an important process in magnetized plasmas ranging from the laboratory to astrophysical scales. It enables the release of magnetic energy believed to power solar flares and magnetospheric substorms. Reconnection also controls the evolution of the topology of the magnetic field, enabling deleterious instabilities, such as the sawtooth instability in fusion experiments, to transport plasma across the experiment's minor radius. Notably, simple estimates of the finite reconnection rate due to classical resistivity fail to explain the fast and explosive nature of reconnection observed in these systems. A major goal of reconnection research is to determine which mechanisms enable "fast" reconnection to occur.

This thesis studied the fluctuations arising in the plasma during magnetic reconnection experiments on the Versatile Toroidal Facility (VTF), with a primary goal of testing whether "anomalous resistivity" due to micro-instabilities can speed the reconnection process. Fluctuations were studied using impedance-matched, high-bandwidth Langmuir probes. Strong, broadband fluctuations, with frequencies extending from near the lower-hybrid frequency $[f_{LH} = (f_{ce}f_{ci})^{1/2}]$ to the electron cyclotron frequency f_{ce} were found to arise during the reconnection events. Based on frequency and wavelength measurements, lower-hybrid waves and Trivelpiece-Gould waves were identified. The lower-hybrid waves appear to be driven by strong perpendicular drifts or gradients which arise due to the reconnection events; an appealing possibility is strong temperature gradients. The Trivelpiece-Gould modes were found to result from kinetic, bump-on-tail instability of a runaway electron population energized by the reconnection events. Nonlinear, spiky turbulence was also observed, and attributed to the creation of "electron phase-space holes," a class of nonlinear solitary wave known to evolve from a strong beam-on-tail instability.

Overall, these instabilities were found to be a *consequence* of reconnection, specifically the strong energization of electrons, leading to steep gradients in both coordinate- and velocity-space. However, it was not established that these modes had a strong feedback on the reconnection process: fluctuation power varied strongly between discharges and was observed to systematically trail the reconnection events. Finally, crude estimates (using quasi-linear theory) of the anomalous resistivity due to these modes did not appear large enough to substantially impact the reconnection process.

Thesis Supervisor: Miklos Porkolab
Title: Professor of Physics

Acknowledgments

I would first like to thank my thesis advisor, Prof. Miklos Porkolab, for his guidance over the past few years, and for supplying an excellent role model in the simple and frank scientific rigor he brings to his work. I would also like to thank the two other members of my thesis committee, Dr. Richard Temkin and Prof. Bruno Coppi, first for their insightful questions and comments on this work. Prof. Coppi's classes (three semesters!) provided an excellent, if challenging, course in plasma physics, and I admire how Dr. Temkin runs his research group and I hope to be able to emulate him. Most of all, I would like to thank Prof. Jan Egedal, who has conceived and guided the reconnection experiments on VTF. He and I have worked together nearly every day of my graduate career, and in this time he has taught me a great deal about the process of scientific research. I will be happy if I have managed to pick up a small fraction of his physics intuition along the way. Miklos and Jan have also inspired me by the way experiment and theory is combined in their work, a path I hope to continue on in my own career.

My fellow graduate students on the VTF experiment, Noam Katz, Ari Lê, and most recently Arturs Vrublevskis, have been excellent co-workers over the past few years. Thanks are also in order for a few MIT undergraduates, Anthony Kesich, Jeff Bonde, and Elizabeth Zhang, who constructed many of the diagnostics in regular use on VTF. Of everyone on the team, I would like to thank Noam in particular for his great dedication through the many evenings we spent pondering the mysteries of the VTF data acquisition system, magnetic flux arrays, and Langmuir probes.

I have enjoyed working on a small-scale physics experiment for the diverse and interesting set of lab experiences that it has provided. However, I now also appreciate the importance of being part of the larger MIT Plasma Science and Fusion Center, and in particular having, just down the hall, a major experiment (Alcator C-Mod) and an associated "critical-mass" of researchers. In particular, I would like to thank a few members of the C-Mod engineering staff, Ed Fitzgerald, Willy Burke, and Bill Parkin, who provided useful advice for many of my projects along the way.

This work was partly funded by a Department of Energy Fusion Energy Sciences Graduate Fellowship and the DOE/NSF Center for Multi-Scale Plasma Dynamics, and I gratefully acknowledge support from these. One summer of the DOE fellowship was spent at

the Princeton Plasma Physics Lab, and I would like to thank Prof. Russell Kulsrud and Dr. Hantao Ji for their hospitality and for teaching me a great deal about plasma instability calculations. Hantao was also my undergraduate thesis advisor, and originally nudged me toward studying basic plasma physics, and I thank him for guidance and advice over the years.

Finally, I would like to thank my parents, Bill and Becky, my brother, Tyler, my parents-in-law, Dan and Jane, and my new, extended family in the Boston area—Dan and Lise, John, Maren, and Eliza, Andrew and MC, and Krista and Franklin. They have all been an incredible source of support and love over the past few years. Tyler, we are very excited that Caterina will be joining our family.

The most thanks of all goes to my wife, Sarah Jane, for bringing me great joy every day. Here's to exploring the world together!

In liberty from the bonds of attachment, do therefore the work to be done: for the man whose work is pure attains indeed the Supreme.

—The Bhagavad Gita—

Contents

List of Figures

List of Tables

Chapter 1

Introduction

Magnetic reconnection [1, 2] is an important physical process in magnetized plasmas ranging from the laboratory to astrophysical scales, governing the storage and explosive release of magnetic energy. It is believed to thereby power solar flares [3] and magnetospheric substorms [4]. More crucially, it also controls coupling of plasma between regions of different magnetic topology. This "opens" the magnetosphere to the solar wind, and, in fusion devices, allows macroscopic tearing and sawtooth instabilities to transport plasma across the minor radius of the device [5].

This chapter begins with a review of the problem of reconnection in highly conducting plasmas, focusing on basic theory and experimental results. These motivate the goals of this thesis research, which is an experimental study of the role of plasma turbulence in reconnection in a laboratory plasma.

1.1 Magnetic reconnection

Plasmas are generally excellent conductors of electricity; a plasma with a temperature of 1 keV has about the same conductivity as copper. They are generally well-described by the theory of ideal magnetohydrodynamics [6] (Ideal MHD), especially on large length scales. In this theory, the magnetic field is "frozen-in" to the plasma flow, and the equations of motion for the magnetic field are given by Faraday's law,

$$\nabla \times \mathbf{E} = -\frac{\partial \mathbf{B}}{\partial t}, \tag{1.1}$$

combined with the "Ideal" Ohm's Law,

$$\mathbf{E} + \mathbf{v} \times \mathbf{B} = 0. \tag{1.2}$$

Here $\mathbf{v}$ is the plasma flow velocity, and $\mathbf{E}$ and $\mathbf{B}$ are the electric and magnetic fields. The Ideal Ohm's law here takes the limit of plasma with zero resistivity, so that electric fields in the plasma reference frame must remain very close to zero. Ideal MHD applies a very strong constraint to the plasma—the magnetic field is "frozen-in" to the fluid flow, and motions which break and change the topological connection of magnetic field lines are forbidden.

An example of what is meant by magnetic topology is shown in a cartoon in Fig. 1-1. In 2-D, magnetic field lines can be conveniently labeled by the flux function ψ, such that $\mathbf{B} \cdot \nabla\psi = 0$. In 2-D, in rectilinear geometry, $\mathbf{B} = \hat{z} \times \nabla\psi$, where $\hat{z}$ is the unit vector coming out of the page. (In Chapter 2 a slightly different definition is presented for use in cylindrical coordinates.) Thus, contours of constant ψ, also called "flux surfaces," trace magnetic field lines.

Figure 1-1(a) plots the magnetic field lines created by two current-carrying conductors (surrounded by vacuum—the plasma case is considered momentarily). One particular field line is highlighted in blue; it has the topology of encircling both conductors. There are also magnetic field lines encircling only one of the individual conductors, which therefore have a different topology than the highlighted surface. Separating the regions of differing magnetic topology is an "x point," where the component of the magnetic field in the plane reverse. In vacuum, where $\nabla \times \mathbf{B} = 0$, the magnetic field lines will meet here at a 90° angle. This "x point" is often called an "x line" or "neutral line," when generalized to 3-D geometry.

Next, topology change occurs when a particular flux surface is pushed from one side of the x point to the other. Physically, this is accomplished by changing the magnitude of current in the conductors, illustrated in the change from Fig. 1-1(a) to (b). As a result, the flux surfaces contract toward the conductors, and the topology of the flux surfaces labeled in solid blue changes from encircling both conductors together to encircling only one of them.

An important point is that inductive electric fields are always involved with this topology change. From Faraday's law, in this geometry, $E_z = -\partial\psi/\partial t$, where E_z is the component of $\mathbf{E}$ coming out of the page. Therefore all motion of flux surfaces requires this inductive

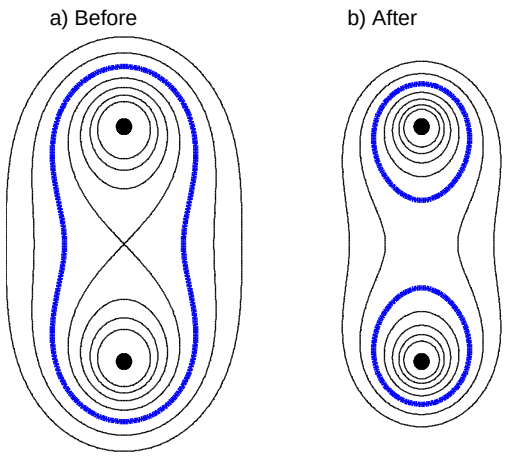

Figure 1-1: Cartoon of topology change of a vacuum magnetic field. From (a) to (b) the solid conductors have changed currents, which changes the topological linkage of the magnetic field labeled by the flux function ψ.

E_z, and topology change requires finite E_z at the x line. Another view is that this electric field is required for the $E \times B$ Poynting flux of magnetic energy from one side of the x line to the other.

This rearrangement of magnetic field-line topology is "reconnection." The story becomes more interesting, however, if, instead of vacuum, the conductors are surrounded by highly conductive plasma. A perfectly conducting fluid does *not* allow the topological rearrangement of field described in Fig. 1-1, because it does not permit the required, finite electric field at the x-line. Such a finite E_z at the x-point contradicts the Ideal MHD Ohm's law in Eq. 1.2, because the magnetic field is zero at the x line, so $\mathbf{v} \times \mathbf{B}$ must go through zero there as well. In 3-D, this generalizes to the vanishing of the vector components of $\mathbf{v} \times \mathbf{B}$ along the x line, but again with the conclusion that Ideal MHD prohibits this topology change.

In order to prevent the topology change, the plasma responds by creating a "current sheet," a thin region with intense current. A cartoon of current sheet formation is shown in Fig. 1-2. This time, the conductors are imagined to be immersed in a perfectly conducting plasma. (This geometry—a pair of conductors immersed in plasma—is just what is used in laboratory study of reconnection.) As before, we vary the currents in the pair of conductors. This time, however, the plasma responds with its own electric current (out of the page, along the x line), enough to keep the electric field at the x line at zero. However, if the plasma current flows only as a line-current along the original neutral point, two new x points would appear immediately above and below. By this same argument, then, current should now

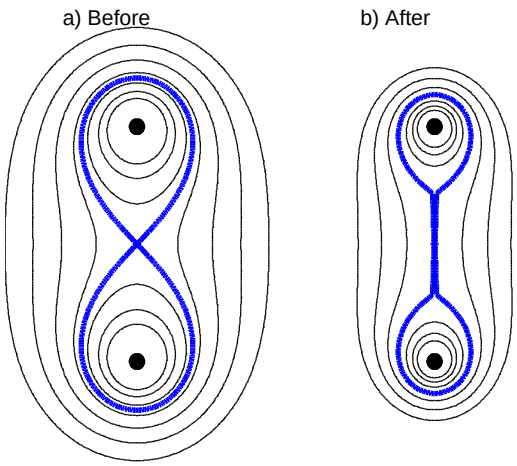

Figure 1-2: Cartoon of attempted topology change in a highly conducting plasma. From (a) to (b) the solid conductors have changed currents. However, this time a current sheet has formed at the original neutral point to prevent ψ from changing there.

flow at these new x points, too. This proceeds *ad infinitum*, and in the end one sees that a whole *sheet* of current should actually exist. The result is that the initial x point is replaced by a current sheet.

To summarize, current sheet formation is the generic Ideal MHD plasma response to an attempted change in topology. This MHD theory of current sheet formation was first due to Syrovatskii [7]. It has since largely been substantiated in numerical simulations [8], and in laboratory experiments on reconnection [9, 10].

Current sheets are highly stressed magnetic field configurations, and thus store magnetic energy. Figure 1-3 shows a picture of magnetic loops taken by the TRACE spacecraft, which observes the surface of the sun over a number of wavelength bands, here in the extreme ultraviolet (171 Å, a useful band because it sees emission from hot plasma of the solar corona but not from the cooler but immensely brighter photosphere). These loops are protrusions of the sun's internal magnetic field and are constantly pushed and churned by turbulent convection beneath the sun's surface. Often two loops will be pushed together, creating stressed magnetic field and a current sheet. Similarly, the earth's magnetotail is a large current sheet trailing the earth for up to 60–80 earth radii; the magnetic field is stressed from the constant forcing of the earth's dipole field from the solar wind.

Current sheets are the generic structures in which magnetic field stress is stored in large-scale, high-conductivity plasmas. If plasmas truly were perfect conductors, the current sheets would simply store energy and only release it (slowly, and reversibly, back to its

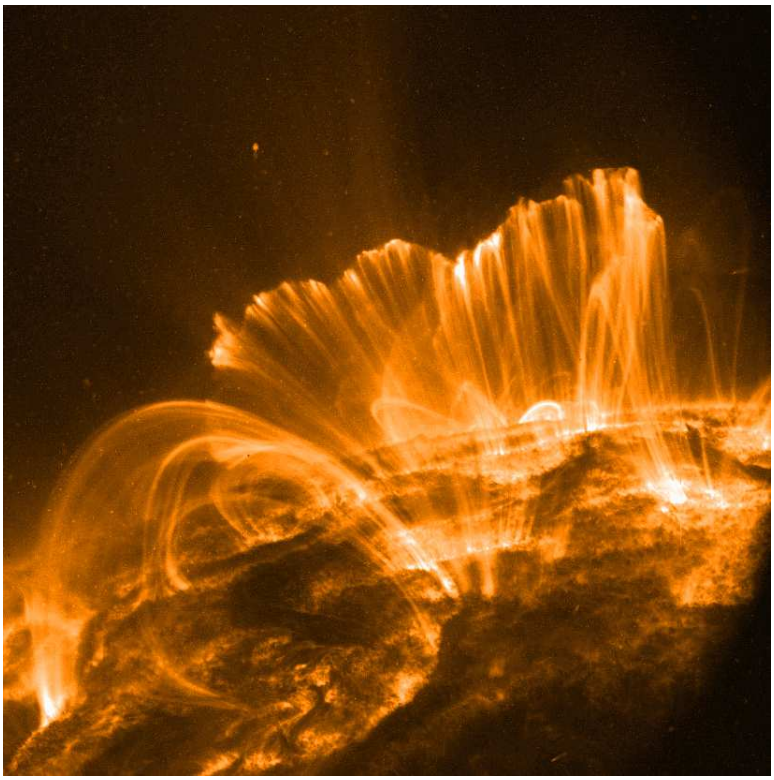

Figure 1-3: Arcade of "post-flare" loops on the surface of the sun, as observed by the Transition Region and Coronal Explorer spacecraft. TRACE is a mission of the Stanford-Lockheed Institute for Space Research, and part of the NASA Small Explorer program.

source) when forcing was removed. Instead, however, they are observed to explosively release this stored energy through "reconnection events." The current sheets store substantial energy, and the subsequent release of this energy by reconnection events is believed to underlie solar flares [11] and magnetospheric substorms [4]. Solar flares furthermore can launch huge volumes of plasma flow off the surface of the sun (and toward the earth) in a "coronal mass ejection," and the decoupling of this plasma from the sun is further evidence that the magnetic field lines have been reconfigured. Dissipation of magnetic energy in "nanoflares"—small scale current sheets between the flux loops in the solar corona—is also a leading candidate to explain why the solar corona is so much hotter than the surface of the sun below it [12].

Some solar flare models are not based on the instability of the current sheet *per se*, but based on other MHD instabilities or catastrophic loss of equilibrium of the plasma [1, 13]. Even these however, are believed to drive the creation of current sheets and eventually drive reconnection during their nonlinear evolution. In this way, those models are similar to sawtooth instabilities in tokamaks—the sawtooth is not initiated by a current sheet instability, but involves reconnection in the nonlinear evolution of a separate instability. Reconnection allows the instability to reconfigure the magnetic field over a macroscopic volume of the plasma, leading to loss of confinement of plasma.

A common feature of all cases is that the phenomena proceed quite rapidly, and a primary challenge to theory and experiment has been to explain the rapid topology change in high-conductivity plasma.

The Sweet-Parker theory of magnetic reconnection was an early attempt at modeling the finite reconnection rate through these current sheets [14, 15]. This theory, in the end, predicts a very slow leaking of energy out of the current sheet, far too slow to explain the fast release observed in solar flares or substorms. (It is also too slow to explain the speed of reconnection events in fusion devices.) From a modern perspective, Sweet-Parker may be best thought of as a minimum, basal rate of reconnection, and its smallness as the reason that current sheets are efficient storers of energy.

The ingredients of the theory include pressure balance of the current sheet, mass conservation of the flows through the current sheet, and an Ohm's law generalized from Eq. 1.2 to include finite resistivity in the plasma. The latter is found to play an essential role in determining the geometry of the current sheet. For the Sweet-Parker model, classical,

collisional resistivity η is assumed, and the Ohm's law is taken to be

$$\mathbf{E} + \mathbf{v} \times \mathbf{B} = \eta \mathbf{j}, \tag{1.3}$$

where $\mathbf{j}$ is the plasma current density. When combined with Faraday's and Ampere's law this gives an evolution equation for the magnetic field (assuming the resistivity is spatially homogeneous for simplicity),

$$\frac{\partial \mathbf{B}}{\partial t} = \nabla \times (\mathbf{v} \times \mathbf{B}) + \frac{\eta}{\mu_0} \nabla^2 \mathbf{B}. \tag{1.4}$$

The first term on the RHS describes advection (and stretching) of the magnetic field by the fluid flow, and the second describes its resistive diffusion—the magnetic diffusion coefficient is $\mathcal{D}_M = \eta/\mu_0$, where η is the resistivity and μ_0 the permeability of free space. Comparing the typical magnitudes of the two terms on the right-hand side gives a dimensionless measure of the smallness of the effects of resistivity on macroscopic scales. The common dimensionless parameter used here is the "Lundquist" number $S = v_A L/\mathcal{D}_M$, which uses a velocity scale of the Alfvén velocity $v_A = (B^2/\mu_0 n m_i)^{1/2}$, and estimates gradients from the macroscopic length L of the system. In the Alfvén velocity, n is the typical plasma number density, and m_i the mass of the ions; it is the velocity derived if magnetic energy $B^2/2\mu_0$ is converted into plasma flow energy $n m_i v^2/2$. Typically the Lundquist number is very large, indicating the smallness of resistive diffusion. For solar flares, for instance, it is $\sim 10^{12}$–10^{14}. Estimates of the Lundquist number, along with other relevant parameters for reconnection in solar flares, the magnetosphere, and the Versatile Toroidal Facility (where experiments reported in this thesis were conducted) are presented in Table 1.1.

The largeness of the Lundquist number explains why the Ideal MHD model discussed earlier is typically a good model for these plasmas on large space scales—resistive diffusion truly is a negligible effect there. However, the presence of an extra derivative operator in the resistive diffusion term implies that it can become important on *short* length scales; this is exactly what happens in the current sheet in the Sweet-Parker model. This reveals an important aspect of the reconnection problem: it is a "boundary-layer" problem, and a central question of reconnection research is, what is the correct plasma physics to reintroduce to correctly model this boundary layer?

The Sweet-Parker model calculates the maximum speed at which steady reconnection

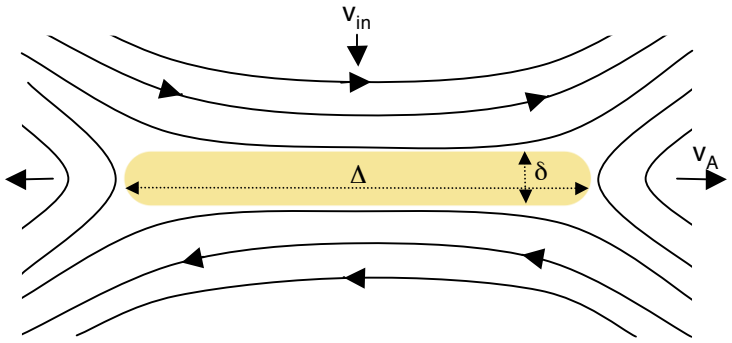

Figure 1-4: Sweet-Parker model of reconnection. The magnetic field reverses across the thin current sheet, which is shaded in yellow. It has a macroscopic length Δ and a microscopic width δ. Plasma and magnetic field flow into the current sheet at speed v_{in} and flow out with $v_{out} \sim v_A \sim (B_{up}^2/\mu_0 n m_i)^{1/2}$.

occurs through a thin current sheet due to classical resistivity alone. The following is a simple, geometrical, order-of-magnitude calculation of the rate of this process, and is illustrated in Fig. 1-4. Plasma and magnetic field flow into the current sheet with a speed v_{in}. There the magnetic field reconnects, and is swept out of the current sheet along with the plasma at a speed v_{out}. The current sheet converts magnetic energy into heat and flow energy of the plasma; based on conversion of the upstream magnetic energy into flow energy, $n m_i v_{out}^2/2 \sim B_{up}^2/2\mu_0$, the outflow speed can be as fast as the Alfvén speed calculated with the magnetic field immediately "upstream" of the current sheet, B_{up}: $v_{out} \sim v_A \sim (B_{up}^2/\mu_0 n m_i)^{1/2}$. (Strictly speaking this is a maximum possible rate, which is used here for simplicity.) Next, conservation of mass flow in and out of the sheet yields $v_{in}/v_{out} \sim \delta/\Delta$, where δ is the width of the current sheet, and Δ the length. Finally, the width is estimated by the criterion that it be small enough so that resistivity balances the reconnection electric field $E_{rec} \sim v_{in} B_{up} \sim \eta j \sim \eta B_{up}/\mu_0 \delta$. Combining these equations, one finds $v_{in}/v_A \sim \delta/\Delta \sim S^{-1/2}$, where S is the Lundquist number evaluated with the length of the current sheet Δ, which is assumed to be a macroscopic length.

The Sweet-Parker theory has been found to be applicable to simulations [8] and also laboratory experiments [10] under appropriate conditions, namely moderately strong resistivity and a short mean-free-path for electron-ion scattering so that other "collisionless" effects (to be discussed next) do not apply. Sweet-Parker does *not* predict the right reconnection rate for solar flares, magnetospheric storms, or tokamak sawteeth—in these systems the time to reconnect a macroscopic amount of magnetic field is very long, $\tau_{SP} \sim \Delta/v_{in} \sim S^{1/2}\tau_A$,

	Solar Flare	Magnetosphere	VTF
Density (m^{-3})	10^{16}	10^{6}	1×10^{18}
Magnetic field (T)	0.1	10^{-8}	3×10^{-3}
Alfvén speed (m/s)	10^{8}	10^{5}	1×10^{4} †
Resistivity (Ω-m)	10^{-6}	10^{-7}	60×10^{-6}
Scale size (m)	6×10^{7} (0.1 $R_{\odot}$)	6×10^{7} (10 $R_{\oplus}$)	0.5
Lundquist S	10^{14}	10^{14}	100
Ion inertial length c/ω_{pi} (m)	10	2×10^{5}	1.5

Table 1.1: Typical scales and dimensionless numbers of systems where reconnection is observed. †For VTF, the Alfvén speed is evaluated with the poloidal component of the magnetic field upstream of the current sheet. Measurement of these parameters in VTF is discussed in greater detail in Chapter 3.

where τ_A is the Alfvén time, Δ/v_A. This is far too slow to explain many observations; under Sweet-Parker solar flares would take a few weeks to complete, rather than the observed time scale of a few hours. The small reconnection rate can be traced, first, to the smallness of the resistivity in those systems; this forces the current sheet thickness to be extremely small. Then, the thinness of the current sheet throttles the mass flow out of the current sheet; this ultimately limits how fast the current sheet can reconnect the field. Extensions to the theory have tried to improve on it both by increasing the effective resistivity and by trying to fix this geometric throttling effect.

However, a more egregious shortcoming of the theory is that current sheets as thin as predicted, and with such an incredible aspect ratio ($\sim S^{1/2}$), will be vulnerable to a number of instabilities long before such a thin current sheet is reached. Some of the most important of these instabilities include resistive [16] and collisionless [17] tearing instabilities. Tearing instabilities break up a long, thin current sheet into a chain of islands, as shown in Fig. 1-5. This is useful for dissipating magnetic energy, as it naturally creates smaller-scale structures where resistive diffusion is more important. Furthermore, tearing instabilities *also* drive reconnection, since island growth necessarily requires additional reconnection of magnetic flux. Therefore, tearing instabilities drive reconnection at yet smaller scales, and these smaller current sheets may themselves be vulnerable to yet smaller tearing instabilities or other instabilities. This has now been observed in resistive MHD simulations [18], as simulations at sufficiently-large Lundquist numbers have become possible. Furthermore, magnetic islands produced by tearing instabilities have now been observed in association

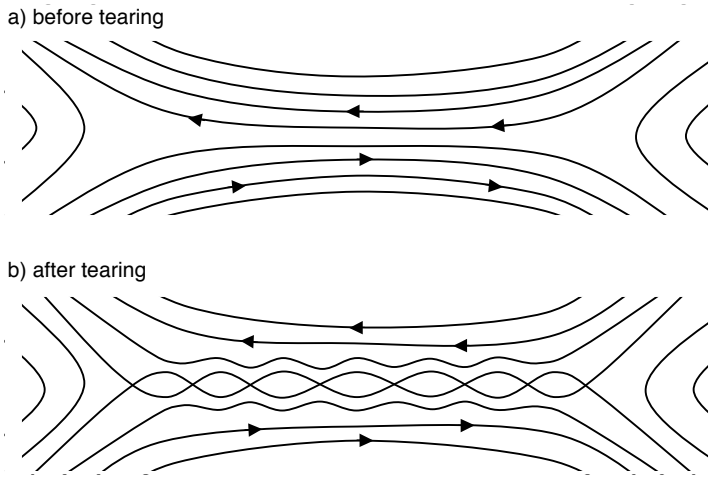

Figure 1-5: Tearing instability of a thin current sheet: the initial thin current sheet (a) is replaced by a chain of islands (b).

with reconnection in the magnetotail (where they were also observed in association with energetic electrons [19]), and there is new evidence of the tearing mode acting on large scales in solar flares [20]. The 3-dimensional tearing of current sheets has also been studied in laboratory plasmas [21].

In addition to being vulnerable to tearing instabilities, the thin current sheets predicted by the Sweet-Parker model can be more narrow than other, fundamental length scales in the plasma, most prominently the ion-inertial length $d_i = c/\omega_{pi}$, where $\omega_{pi} = (ne^2/\epsilon_0 m_i)^{1/2}$ is the ion-plasma frequency, or the ion gyroradius $\rho_i = v_{ti}/\omega_{ci}$, where $v_{ti} = (2T/m_i)^{1/2}$ is the ion thermal speed and $\omega_{ci} = eB/m_i$ is the ion gyrofrequency. These are characteristic lengths in the plasma at which electrons and ions decouple, so that below these scales one really needs to keep track of separate electron and ion flows. (In contrast, in the ideal or resistive MHD pictures, the relative drift of electrons and ions comprising the current must be much smaller than the net plasma velocity.) For instance, a current sheet that is 1 d_i wide will have a relative electron-ion drift of the ion thermal speed. In the magnetotail in particular, this inertial scale is crossed long before any resistive scale is crossed.

This observation leads to the next two branches of reconnection theory: laminar and turbulent "two-fluid" reconnection. In the laminar theories, one further generalizes the resistive Ohm's law above to the "generalized" Ohm's law [1], (which derives from the

electron momentum equation),

$$\mathbf{E} + \mathbf{v} \times \mathbf{B} = \eta \mathbf{j} + \frac{1}{ne}\mathbf{j} \times \mathbf{B} + \frac{1}{ne}\nabla \cdot \mathbf{P} + \frac{m_e}{e^2}\frac{d\mathbf{j}/n}{dt}. \tag{1.5}$$

Here the new term $\mathbf{P}$ is the electron pressure tensor, and m_e is the electron mass. Of the terms in this equation, the most important is the "Hall" term $\mathbf{j} \times \mathbf{B}$, which becomes important when the current sheet becomes of order c/ω_{pi} wide. Including this "Hall" effect in simulations has been found to have a profound effect on the geometry of the current sheet [22], opening it to an "x" geometry compatible with fast inflow and outflow. This substantially increases the reconnection rate over the Sweet-Parker model, allowing for reconnection inflows near $0.1v_A$ rather than $v_A/S^{1/2}$. The decoupling of electron and ion motion on these scales was observed in reconnection experiments by Gekelman *et al* [23], where including the Hall effect was an important consideration for electron momentum balance near the x line. However, in these experiments the ion gyroradius was larger than the scale of the device, so they could not give a complete picture of how these effects could be coupled to a macroscopic, MHD current sheet. More recently, however, experiments that are in an MHD regime (i.e. d_i and ρ_i much smaller than the device size) have been able to find these two-fluid effects within their current sheets [24–26]. Finally, these effects have also been found by spacecraft flying through reconnecting current sheets in the earth's magnetosphere [27].

Experiments on the VTF device are also actively looking for these two-fluid effects. One important difference between VTF and those experiments referenced above is that VTF studies magnetic reconnection in a strong "guide" field regime. Here, the "guide" magnetic field is the component of the magnetic field *parallel* to the neutral line; in VTF this is the strongest component of field by about a factor of 10. (Other experiments, such as the Magnetic Reconnection Experiment (MRX) at Princeton [10], have studied an "anti-parallel" reconnection geometry with zero or very small guide field.) This was not discussed explicitly before; it does not really affect the kinematics of reconnection, but does alter the plasma dynamics near the current sheet. For instance, one point to realize is that the correct Alfvén speed (e.g., for the Sweet-Parker model) is the one calculated based on the upstream, *reconnecting* component of the magnetic field, rather than calculated with the total magnetic field. The guide field also affects the two-fluid effects discussed above: rather than the

inertial length d_i, in the strong-guide field regime the relevant length scale for decoupling is the ion "sound" gyroradius $\rho_s = c_s/\omega_{ci}$, with the sound speed $c_s = (k_B T_e/m_i)^{1/2}$, and ion cyclotron frequency $\omega_{ci} = eB/m_i$ [28]. The sawtooth reconnection problem in tokamaks is in a similar, strong-guide-field regime as VTF.

Besides these laminar two-fluid effects, there are also "turbulent" two-fluid effects. The laminar two-fluid effects are found to set in for thin current sheets, once they reach the d_i or ρ_s scale. However, if the current sheet thins to these levels, it also becomes unstable to a host of current-driven micro-instabilities. These are postulated to speed-up reconnection by imbuing the plasma with "anomalous resistivity," extra scattering of the charge carriers due to a turbulent bath of waves arising in the plasma due to the instability. A large number of these instabilities have been studied in the literature, such as Buneman [29], ion-acoustic [30], ion-cyclotron, and lower-hybrid instabilities [31, 32]. The latter are gradient-driven instabilities which set in when gradients in plasma density or temperature are strong enough so that perpendicular (diamagnetic) drifts exceed the sound speed. This turns out to occur when the current sheet is as narrow as d_i in the anti-parallel reconnection case or ρ_s in the guide field reconnection case.

These instabilities may first aid reconnection simply by increasing the effective resistivity of the plasma—i.e. S becomes smaller. A more subtle point, however, is that a *spatially* dependent resistivity has been found to further speed reconnection by changing the geometry of the current sheet, opening the geometry in a manner similar to the laminar "Hall" mechanism above [33]. (On the other hand, spatially uniform resistivity has proven to allow only reconnection solutions with narrow, Sweet-Parker-like current sheets [34, 35].) This point has been explored, to date, in simulations with *ad hoc* anomalous resistivity [36].

It is therefore an important question which of these two mechanisms can prevail in current sheets. Within naive estimates, they will both set in at similar current sheet widths. Furthermore, standard, 2-D simulations of reconnection suppress these instabilities, as 2-D simulations do not include any modes with components of $\mathbf{k}$ transverse to the 2-D reconnection plane. This direction happens to be the direction of current flow, however, and therefore current-driven instabilities are suppressed. 3-D simulations are still in their infancy, but some important effects have already been found. Notably, Drake *et al* [37] found strong current-driven electron-ion (Buneman) instability in 3-D particle simulations. The instability was strong enough to saturate nonlinearly by trapping electrons, forming "electron hole"

structures; these will be discussed in Chapter 5, as similar nonlinear turbulence has been observed in VTF. These simulations found that these instabilities provided useful anomalous resistivity to the reconnection process, and may also be important in up-scattering electrons to higher energies, and thus may play a role in particle energization. Finally, the laminar Hall mechanism above does not actually provide dissipation to break magnetic field lines. At the smallest scales, therefore, *both* laminar and turbulent mechanisms for fast reconnection may play complementary roles [38].

These questions have inspired significant experimental research on fluctuations and turbulence and their roles in the reconnection process. Some of the earliest research in this vein was conducted by Gekelman and Stenzel, *et al* who found ion-acoustic instabilities, magnetic whistler-wave turbulence, and plasma-wave (ω_{pe}) emission. The plasma waves were attributed to instability of high-energy runaway particles produced during reconnection [39]. Research on the MRX device has also found electrostatic turbulence consistent with lower-hybrid drift instabilities [40, 41] and, more recently, magnetic fluctuations in the same lower-hybrid frequency regime [42]. These are still under study but have been argued to be the electromagnetic generalization of the lower-hybrid instability.

Fluctuations are also known to interact with high energy particles, which are ubiquitously observed to be created by reconnection processes. Solar flares energize electrons, which is inferred from hard x-ray emission associated with the flares [3], and energetic (300 keV) electrons has been observed directly by spacecraft flying through reconnection regions in the earth's magnetotail [43]. Runaway electron production is also a well-known consequence of sawtooth events in tokamaks [44]. Laboratory experiments on reconnection have also reported the creation of energetic ions [45], and anisotropic, super-thermal tails to the electron distributions and the associated anisotropy-driven instabilities[46]. Other recent theoretical work has found that instabilities may play a role in *energizing* particles [37], so much work remains toward understanding the interplay of fast particles, fluctuations, and reconnection.

1.2 Thesis objectives

The main objective of this thesis is the experimental study of high-frequency, current-driven instabilities during reconnection in the Versatile Toroidal Facility (VTF). This entails ob-

servation of instabilities, identification based on frequency and wavelength measurements, and study of the correlation of these modes with reconnection. During the course of these investigations, it appeared likely that a number of the instabilities were driven by a fast "tail" population of energetic electrons. Therefore, this thesis also makes some initial measurements of energetic electron production by reconnection.

1.3 Summary and Outline

This thesis presents an experimental study of the role of turbulent plasma fluctuations during magnetic reconnection. Notable results include the observation of lower-hybrid waves and high-frequency Trivelpiece-Gould modes driven by high-energy electrons produced by the reconnection event. These results also include the first laboratory observation of nonlinear "electron-hole" structures created self-consistently out of beam-driven turbulence [47]. Overall, most fluctuations are observed to have a fast phase-speed and therefore result from *electron-electron* instability. They therefore may play a role in restraining runaway electrons, but likely do not contribute much direct anomalous resistivity to the plasma, for which it is necessary that the modes are strongly coupled to the ions. Furthermore, systematic time lags are observed between reconnection events and the peak fluctuation power, making it further difficult to argue that these modes are *necessary* for the reconnection process in VTF. Instead, it seems more likely that they occur as a consequence of reconnection—in particular, as a consequence of the strong electron energization associated with reconnection. It does not appear that the modes feed back strongly on or substantially control the reconnection process.

This thesis is divided into the following chapters:

Chapter 1 has presented an overview of the main questions in magnetic reconnection research motivating the studies conducted here.

Chapter 2 will discuss the experimental setup, including the VTF device, and diagnostics used for baseline reconnection observations. It presents detailed description and discussion of "fast" Langmuir probes used for fluctuation measurements and gridded energy analyzer probes for measurements of the electron distribution function.

Chapter 3 discusses baseline reconnection results from the VTF experiment, including

observations of the formation of a current sheet and its fast disruption due to "spontaneous" reconnection events. Electric fields during the reconnection events are found to approach the runaway electric field and therefore are capable of creating high energy populations of electrons. Measurements of electron energization are presented from studies with the gridded energy analyzer.

Chapter 4 presents observations of electrostatic fluctuations and their correlation with reconnection events. In general, large fluctuations are seen to arise during the reconnection events. These are analyzed based on frequency spectra and wavelength measurements from multi-probe correlation techniques. Two broad classes of waves are found: lower-hybrid waves and high-frequency Trivelpiece-Gould waves. A number of excitation mechanisms for these waves are reviewed based on linear theory. The lower-hybrid waves can arise from strong cross-field drifts or gradients which arise during the reconnection process; an interesting possibility is the observed steep spatial gradients ("filamentation") of the hot electrons. The high-frequency Trivelpiece-Gould waves are found to arise from bump-on-tail (Čerenkov) instability of a high-energy electron population created by the reconnection events.

Chapter 5 presents observations of nonlinear plasma structures—"electron phase-space holes"—within the turbulence. These are understood to arise in the nonlinear evolution of strong instabilities when the waves grow fast enough to trap electrons in the wave trough. The speed and size of these structures is measured using multiple probe tips; these are compared with available theoretical predictions and spacecraft observations. Based on observation of the hole speed, it is found that they emerge from strong *electron-electron* velocity space instability, and therefore likely do not contribute directly to generating anomalous resistivity.

Chapter 6 will present conclusions from this work and suggest future research.

Appendix A presents a derivation of the quasi-linear estimate of electron-ion momentum exchange due to plasma waves. Appendix B presents experiments which explore the plasma-probe coupling of RF Langmuir probes used in this thesis.

Chapter 2

Experimental Apparatus

This chapter presents background information about the Versatile Toroidal Facility (VTF) where experiments for this thesis were performed. The basics of the experiment are described, including plasma formation, how magnetic fields are applied to the plasma, and how a current sheet is induced in the plasma for reconnection studies. The primary diagnostic used for measuring the reconnection events, the magnetic flux diagnostics, are also described.

The next section describes RF, or "fast," Langmuir probes, which have been designed and constructed to study plasma fluctuations during reconnection events. This begins with a short review of DC operation of Langmuir probes, as this determines the plasma equilibrium near the probe, which is necessary for calculating how plasma fluctuations couple onto the probe. It is found that the coupling can be modeled as a lumped-circuit parallel resistor and capacitor; the capacitor gives the probe a rising response at high frequencies. This effect has been experimentally observed using RF probes on VTF, giving a measure of confidence in the probe models. (These experimental measurements are presented in Appendix B, as they fall outside of the main focus here, which is on the relationship between the fluctuations and the reconnection events.)

The final section describes the design and construction of gridded electron energy analyzers, which have been used to study electron energization by the reconnection events. Original measurements of fast electrons were taken with single-channel energy analyzers, but there are challenges interpreting these measurements because the plasma and reconnection events are not highly reproducible. Therefore, a seven-channel energy analyzer was

designed and constructed (using printed circuit board techniques) to observe electrons at multiple energies simultaneously.

This chapter will largely focus on the design and construction of the probes; physics results from the probes will be presented over the coming chapters.

2.1 Versatile Toroidal Facility

The VTF device is a large toroidal vacuum chamber (major radius $\simeq$ 1 m, chamber volume $\simeq$ 5.4 m^3), with easy access through a large number of ports for installing various diagnostics. Over the years a number of different basic plasma physics experiments have been performed on the low-temperature plasma, including experiments to study ionospheric plasma phenomena [48], and magnetic reconnection experiments in an "open" magnetic field configuration where the magnetic field lines intersect the chamber wall [49–51]. The vacuum chamber is pumped by a 450 L/s Leybold turbo pump backed up by a scroll pump; the scroll pump is also used directly to rough pump the vacuum chamber during pump down. Base pressures of about 2×10^{-6} Torr were attained for experiments reported in this thesis. Pressure is monitored by an ionization gauge and a quadrupole mass-spectrum (residual gas) analyzer, finding predominant base gases of mostly water vapor and nitrogen. For experiments here, argon gas is leaked into the chamber to reach a pressure $\simeq 1 \times 10^{-4}$ Torr. This corresponds to an un-ionized, initial neutral density of about 3×10^{18} m^{-3}.

Figure 2-1 shows a photograph of the VTF device. Highly prominent are the 18, 4-turn, orange toroidal field coils. These apply a dominant toroidal magnetic field to the plasma volume. The magnets are specified for toroidal fields up to 1.2 T and can be water-cooled for this purpose. However for experiments here we use magnetic fields between about 50 and 70 mT at major radius $R = 1$ m, with typical coil currents of 3–5 kA per turn. During the plasma discharges, this field is constant in time, as the L/R time scale for these coils is about 1 sec. (Further, the poloidal fields are typically much smaller than the toroidal field, and the plasma $\beta = 2\mu_0 p/B^2$, where p is the plasma pressure and B the magnetic field strength, is small, $\sim 10^{-3}$, so the plasma perturbation to the toroidal field is also very small.)

This range of toroidal magnetic fields (50–70 mT at $R = 1$ m) locates a 2.45 GHz electron cyclotron resonance (87.5 mT) within the chamber volume. This allows for repro-

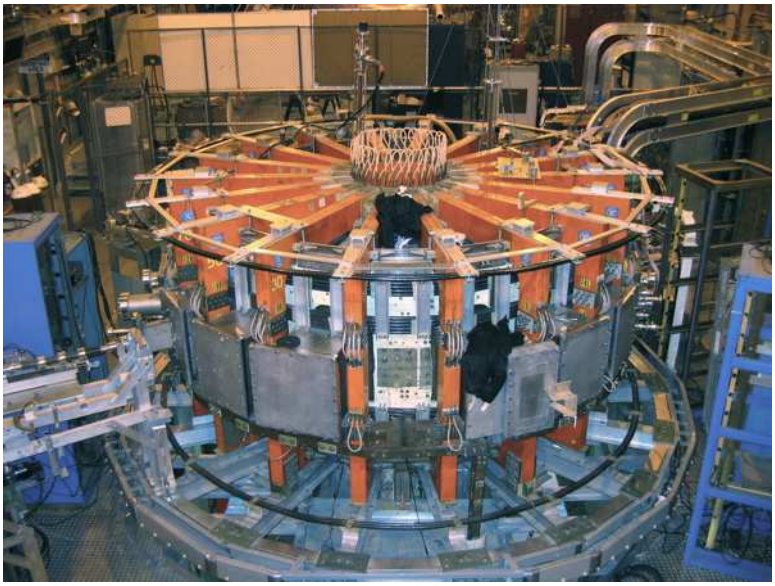

Figure 2-1: Photo of the Versatile Toroidal Facility.

ducible plasma startup with a short burst of microwaves (15 kW, $\lesssim 100$ μs) at this resonant frequency.

An additional set of 4 toroidal conductors fixed within the vacuum vessel carries toroidal current and generates poloidal magnetic field, the component of magnetic field which undergoes reconnection. These 4 conductors (actually 4 coaxial *pairs* of conductors—which will be called the "shell" and "pin" conductors) are central to the reconnection drive scheme, which was first implemented and is discussed in Ref. [52]. The experiment proceeds in two stages, which will be described using Fig. 2-2. After the initial microwave breakdown, the plasma density is built up for 1–1.2 ms in an "ohmic heating" phase. Ohmic heating is driven by an ohmic solenoid, which is wound mostly inside the inner wall of VTF, but also includes some turns on the outer wall to minimize stray magnetic fields within the plasma volume. Ramping current through the solenoid induces a moderate (2 V/m) toroidal electric field within the chamber volume. This drives both a plasma current and currents in the "shell" conductors of each of the 4 internal conductors. (The shell conductors are wired in series so that they carry identical current.) Figure 2-2(a) shows the evolution of total ("shell" + "pin") current in the four conductors. The blue, dashed curve shows current in the inner (closer to mid-plane) pair of conductors, and the red curve shows the current in the outer (further from mid-plane) pair; over the ohmic heating phase the net current in all four are equal.

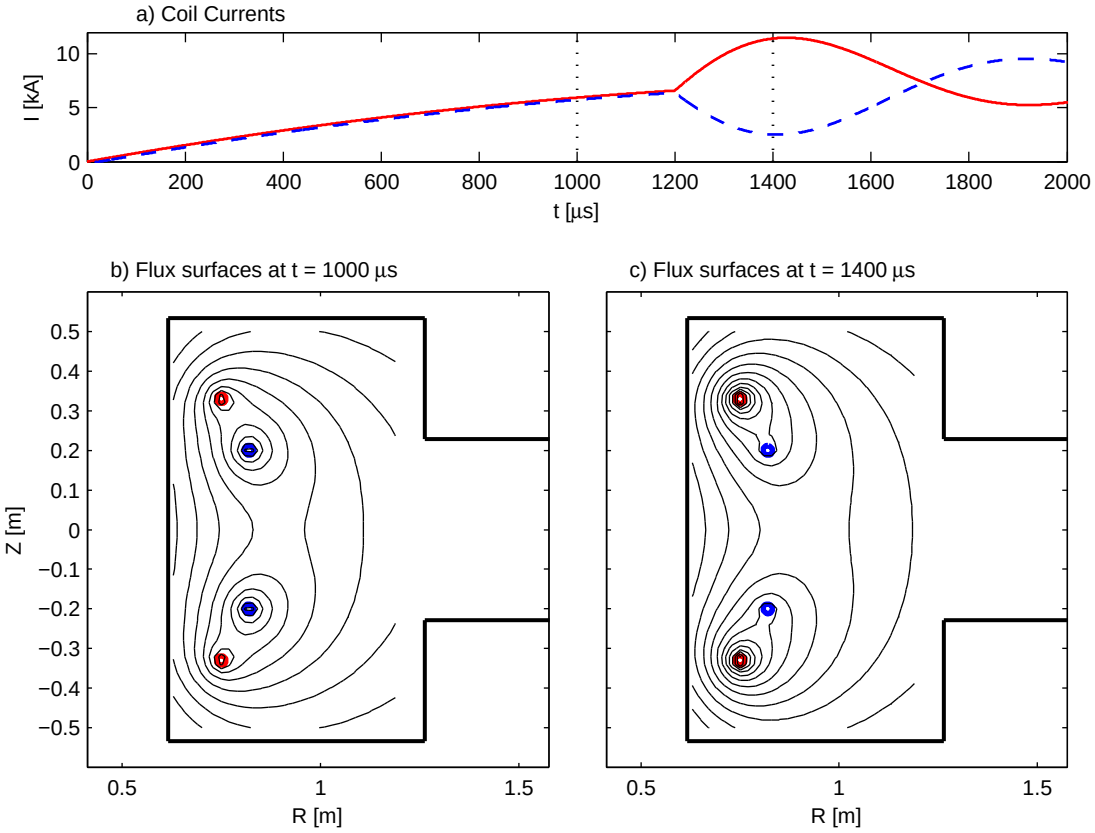

Figure 2-2: Reconnection drive scheme for VTF. a) Typical currents in outer (red) and inner (blue, dashed) internal conductors. (b,c) Poloidal cross section of VTF, showing vacuum chamber boundary in heavy, solid lines, and the location of the outer (red) and inner (blue) internal conductors. (b, c) also show vacuum flux surfaces (i.e. those measured without a plasma) at respective times $t = 1000$ μs, and $t = 1400$ μs, which are characteristic of the ohmic heating phase and reconnection drive stage.

Figure 2-2(b) shows a poloidal cross section of the VTF device, with the vacuum chamber boundary in heavy solid line. The inner (blue) and outer (red) internal conductors are also denoted, along with vacuum magnetic flux surfaces (i.e. magnetic flux surfaces measured when no plasma is in the chamber), at $t = 1000$ μs, characteristic of the ohmic heating phase. During this phase of the experiment the conductor currents dominate the plasma current, and therefore, the vacuum fields are not too far from the fields observed in plasma. The poloidal magnetic field surfaces assume a "figure-eight" shape with an x line on the mid-plane where the poloidal field goes to zero.

After the ohmic heating phase, reconnection is driven in the plasma. A capacitor is discharged through the pin conductors, which are wired in series such that the current is in the forward direction on the outer pair and in the reverse direction on the inner pair. The result is that the *net* current carried by the inner (blue) conductors decreases while the net current carried by the outer (red) conductors increases. This evolution is indicated in Fig. 2-2(a) at $t = 1200$ μs, where the current traces begin to diverge. This swing in current pulls the flux surfaces vertically away from the x line, and they collect around the outer (red) pair of conductors, as is visible in Fig 2-2(c). However, the plasma opposes this strong pull on the flux surfaces, and in response, the plasma current increases strongly and the x line is pulled into a current sheet, as discussed in Chapter 1. It is the reconnection of this current sheet that is of primary interest. Observations of the dynamics of this current-sheet-formation and subsequent disruption by a strong reconnection event will be discussed in detail in Chapter 3.

Finally, a visible light photograph of a hydrogen plasma in VTF is shown in Fig. 2-3. In addition to creating a relevant magnetic geometry for reconnection studies, the currents in the internal conductors (the central pair are prominent in the foreground, and all four can be seen in the background) also apply some rotational transform to the flux surfaces, and magnetic field lines sufficiently close enough to the coils do not intersect the wall. This leads to plasma confinement to regions close to the coils and current sheet, as is visible in the photo.

2.1.1 Baseline VTF Diagnostics

The main goal of experiments reported in this thesis is to connect observations of the evolution and reconnection of the plasma current sheet with measurements of "fast," high-

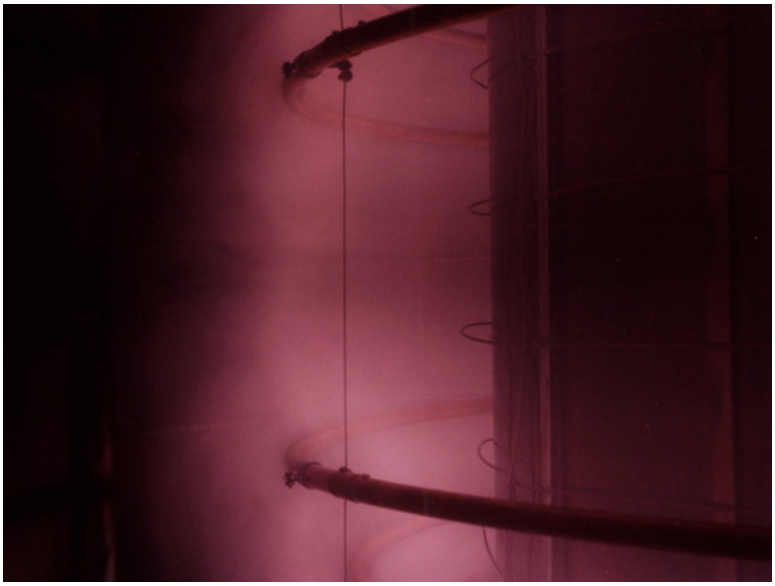

Figure 2-3: Visible light photograph of a hydrogen plasma in VTF. The exposure was open for the entire discharge. Two of the four internal conductors are visible in the foreground; plasma confinement due to their poloidal field is apparent in the plasma density gradient.

frequency plasma fluctuations. This section describes how we measure the former.

Magnetic equilibrium, currents, and toroidal electric fields all derive from measurement of the poloidal flux function,

$$\Psi(R,z) = \int_0^R R' B_z(R',z') dR'. \tag{2.1}$$

(This is the same Ψ as is used in the equilibrium description of tokamaks and other axisymmetric plasmas, i.e. by the Grad-Shafranov equation [6].) For our studies here, Ψ is a highly useful experimental quantity for several reasons. First, Ψ is exactly the poloidal magnetic flux, and thus measures the quantity of field which has been reconnected. $\dot{\Psi}$ evaluated at the x line or on the current sheet is therefore the reconnection rate, and from Faraday's law $E_\phi = -\dot{\Psi}/R$. Contours of constant Ψ also correspond to the poloidal projection of magnetic field lines, and therefore Ψ also contains information about magnetic geometry useful for visualization.

In VTF, flux function measurements are accomplished with 2-D arrays of novel magnetic flux probes [53], which consist of a set of rows of Faraday loops, which each measure $\int \dot{\mathbf{B}} \cdot d\mathbf{A}$, where $d\mathbf{A}$ is an area in the R–ϕ plane. A single row resembles a rope ladder, with the measurement area for Faraday's law ($d\mathbf{A}$) being one of the holes in the ladder. Loop areas

increase with major radius so that the sum along the row performs the correct integral to yield $\dot{\Psi}$. Finally, time integration is performed numerically to yield Ψ.

At present Ψ is measured at two toroidal locations on a 2-D region spanning the inner wall to outside the current sheet, and in between the inner pair of coils. Each 2-D array entails approximately 150 separate measurements and yields Ψ evaluated on a 10×14 grid, with resolution of about 3 cm. In addition, the poloidal flux function is also measured using a single row on the mid-plane of the device at 6 toroidal locations; this is used to observe the toroidal evolution of the reconnection events. A set of "baseline" observations of reconnection of VTF current sheets has been assembled largely from data from the magnetic flux probe diagnostic and will be presented in Chapter 3.

In addition to flux probes, we also employ 2-D arrays of Langmuir probes and a microwave interferometer to measure density line-integrated along a vertical chord. For reference, Table 2.1 presents definitions and typical values of plasma parameters.

Building up the capabilities of this machine and assembling diagnostics has been a major effort over the past few years for the whole VTF team. Some of the experimental contributions from the author include the computer code to control the ICS digitizers, which are the backbone of the data acquisition system for VTF, with nearly 900 installed channels, and a modified control system which allows extended batches of experiments to be run on a cadence without operator interaction.

2.2 Fast Langmuir probes

Langmuir probes are one of the most widely-used diagnostics for laboratory plasmas, useful for plasmas ranging from low-temperature plasmas such as VTF up to the edge plasmas in fusion experiments [54]. Simply a metal electrode drawing current out of the plasma, it is one of the most elementary ways to measure plasma density, temperature, and electric fields. However, while it is straightforward to build and collect data from Langmuir probes, some non-trivial theory is always required to relate the measurements to the intrinsic parameters of the plasma.

This section describes the design of RF, or "fast" Langmuir probes for observation of plasma fluctuations during the reconnection events. It begins with a presentation of background theory for RF probes. The main concern here is to predict how fluctuations in

Density	n	$\sim 1 \times 10^{18}$ m^{-3}
Temperature	$k_B T_e$	$\gtrsim 15$ eV $\gg kT_i$
Gas fill		argon, 1×10^{-4} torr
Toroidal magnetic field (R = 0.92 m)	B_ϕ	72 mT
Poloidal magnetic field	$B_{r,z}$	$\lesssim 5$ mT
"Upstream" magnetic field	B_{up}	~ 3 mT
Plasma beta	$\beta = 2\mu_0 n k_B T / B^2$	$\sim 10^{-3}$
Plasma frequencies	$\omega_{pe} = (ne^2/\epsilon_0 m_e)^{1/2}$	$\simeq 2\pi\times$ 10 GHz
	$\omega_{pi} = (ne^2/\epsilon_0 m_i)^{1/2}$	$\simeq 2\pi\times$ 40 MHz
Gyrofrequencies	$\omega_{ce} = eB/m_e$	$\simeq 2\pi\times$ 2 GHz
	$\omega_{ci} = eB/m_i$	$\simeq 2\pi\times$ 30 kHz
Lower-hybrid frequency ($\omega_{pe}^2 \gg \omega_{ce}^2$)	$\omega_{LH} = (\omega_{ce}\omega_{ci})^{1/2}$	$\simeq 2\pi\times$ 7 MHz
Electron thermal speed	$v_{te} = (2k_B T_e/m_e)^{1/2}$	$\simeq 2.5 \times 10^6$ m/s
Ion sound speed	$c_s = (k_B T_e/m_i)^{1/2}$	$\simeq 6 \times 10^3$ m/s
Upstream Alfvén speed	$v_{A,up} = (B_{up}^2/\mu_0 n m_i)^{1/2}$	$\simeq 1 \times 10^4$ m/s
Total Alfvén speed	$v_A = (B_\phi^2/\mu_0 n m_i)^{1/2}$	$\simeq 2.5 \times 10^5$ m/s
Inertial lengths	$d_e = c/\omega_{pe}$	$\simeq 5$ mm
	$d_i = c/\omega_{pi}$	$\simeq 1.5$ m
Electron gyroradius	$\rho_e = v_{te}/\omega_{ce}$	$\simeq 200$ μm
Sound gyroradius	$\rho_s = c_s/\omega_{ci}$	$\simeq 4$ cm
Debye length	$\lambda_D = (\epsilon_0 k_B T_e/ne^2)^{1/2}$	$\simeq 25$ μm

Table 2.1: Typical plasma parameters

the plasma will couple to a probe. First, we will briefly review how the probes respond to steady-state, DC plasma conditions. This is required since the DC conditions determine the equilibrium state of the plasma near the probe, which controls the RF coupling. The main result is that the coupling can be modeled as a parallel resistor and capacitor, which we will call R_p and C_p, i.e. the "plasma-probe" resistance and capacitance. The capacitance gives the probe a (6 dB/octave) rising response at high frequencies; the corner frequency $1/(2\pi R_p C_p)$ scales with the ion-plasma frequency $f_{pi} = (1/2\pi) \times (ne^2/\epsilon_0 m_i)^{1/2}$, and numerically is predicted to be of the order 3–4 f_{pi} for our probe geometries.

2.2.1 DC Langmuir probe theory

The DC theory of probe operation is described in numerous places, for example the textbook by Hutchinson [54], the classic review by Chen [55] and a more recent review from Demidov *et al* [56].

A probe immersed in the plasma draws an admixture of electron and ion current from the plasma, depending on the bias of the probe relative to the ambient potential in the plasma. Consider first a probe biased equal to the ambient space potential, $V_{bias} = V_{plasma}$. Then, no electric field exists between the probe and the plasma, and the probe freely collects electrons and ions, which simply stream to the probe at their respective thermal speeds. The collection rate for each species is

$$I_{i,e} = \pm \frac{e n_\infty A_p}{4} \sqrt{\frac{8 k_B T_{i,e}}{\pi m_{i,e}}}. \tag{2.2}$$

Here A_p is the area of the probe, T and m are the temperature and mass of the two species, and n_∞ is the ambient plasma density. Further, e is the magnitude of the electron charge, and we adopt the convention of measuring current *into* the probe, so that the electron current is negative. The additional factors 1/4 and $\sqrt{8/\pi}$ arise from integrals over the Maxwellian distribution function. One simple modification to this formula occurs when a species is magnetized on the scale of the probe, i.e. the gyroradius is smaller than the probe dimension. Then the collecting area of the probe is that projected onto the plane perpendicular to the magnetic field.

Next, we generalize to the case where the probe is biased to repel electrons, i.e. $V_{bias} - V_{plasma} < 0$. A boundary layer around the probe forms to connect the electric potential

$\phi(\mathbf{x})$ from $\phi = V_{bias}$ at the probe surface to the ambient $\phi = V_{plasma}$. The electrons adopt a Boltzmann distribution $n \propto \exp(e\phi/k_B T_e)$ in response to ϕ. Applying this Boltzmann condition, the electron current drawn by the probe becomes

$$I_e(V) = \frac{-en_\infty A_p}{4}\sqrt{\frac{8k_B T_e}{\pi m_e}}\exp\left(\frac{e(V_{bias} - V_{plasma})}{k_B T_e}\right). \tag{2.3}$$

This is just the earlier "free" electron flux attenuated by the Boltzmann factor.

Next, the ions, unlike the electrons, are attracted by the probe, and therefore they do not have a simple Boltzmann response to the potential distribution. In general the ion density, ion flux, and spatial distribution of potential around the probe must be calculated self-consistently. This becomes a more involved calculation, discussed in detail by, e.g. Hutchinson [54]. The result is that the bias at the probe is connected to the ambient plasma through a thin boundary layer. This boundary layer is only a few Debye lengths thick [$\lambda_D = (\epsilon_0 k_B T_e/ne^2)^{1/2}$], and is referred to as the probe "sheath." Outside of the sheath, the plasma is quasi-neutral [$\nabla^2\phi \ll e(n_i - n_e)/\epsilon_0$], and the ions are pulled to the probe by weak, long-range electric fields. The ions are found to arrive at the sheath edge at the sound speed, $c_s = \sqrt{k_B T_e/m_i}$, and the space potential at the sheath edge is roughly $V_{plasma} - k_B T_e/2e$. By continuity of current, the total flux of ions across the sheath edge or probe surface are equal. However, most of the potential drop occurs *inside* the sheath edge, and thus the flux of ions to the probe typically saturates at strong negative bias, becoming only a weak function of bias (and ideally a constant). This current is called the "ion-saturation current" and its value has been calculated, e.g. by Hutchinson [54] to be

$$I_{si} \simeq 0.6en_\infty A_s c_s. \tag{2.4}$$

Here A_s is the area of the sheath, derived from the probe radius expanded outward by the width of the sheath. Inside the sheath, the quasi-neutrality condition breaks down, and the ions are accelerated onto the probe surface by strong electric fields. A Child-Langmuir-type relation (as applies, e.g. for vacuum-tube diodes) exists between potential, density, and ion flux, and the sheath structure, including its width, can be found by solving these Child-Langmuir equations. (Meanwhile, the electrons are strongly repelled, and contribute negligible charge density inside the sheath, so typically their presence can be ignored when calculating the sheath structure.) Typically the sheath width is found to be 3–5 Debye

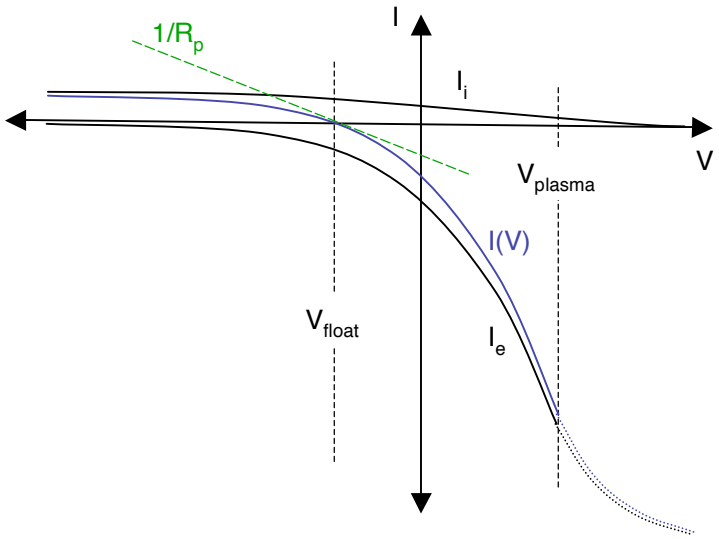

Figure 2-4: Langmuir probe $I(V)$ characteristic. Individual electron (I_e) and ion (I_i) characteristics sum to yield total $I(V)$. The "plasma-probe resistance" R_p is the inverse of the slope of the $I(V)$ characteristic evaluated at the floating potential.

lengths, and the width scales like $V_{bias}^{3/4}$ as the probe bias becomes very strong. This "sheath expansion" effect can give a small residual dependence of the ion current on the probe bias deep in the ion-saturation regime if the probe size is not substantially larger than the Debye length.

Figure 2-4 shows the result of this analysis, the separate electron and ion currents as a function of the probe bias, plus their sum, the Langmuir probe "I(V) characteristic." Notably, there exists a bias at which the exponentially attenuated electron current and saturated ion current balance. At this potential, denoted the "floating potential," or V_{float}, no net current is drawn by the probe. Combining Eqs. 2.3 and 2.4, the floating potential is found to be several T_e below the space potential,

$$V_{float} - V_{plasma} = -\frac{k_B T_e}{e} \times \log\left(0.66 \frac{A_p}{A_s}\sqrt{\frac{m_i}{m_e}}\right). \tag{2.5}$$

Here, the weak dependence of the sheath area A_s on the probe bias can be ignored, or just estimated once and inserted, since it is within the weakly-varying logarithmic factor. The main effect is the mass ratio: for argon (mass number 40) plasmas used on VTF, V_{float} is about 5.2 T_e below the plasma potential. Therefore the probe must be biased to reflect about 99.5% of the electrons in order for electron and ion currents to balance.

Figure 2-4 also defines the "plasma-probe resistance" R_p: the inverse of the slope of the

$I(V)$ curve, evaluated at the floating potential. (The tangent line is shown as the green, dashed line.) By differentiating the $I(V)$ characteristic (again using Eqs. 2.3 and 2.4), one finds that $R_p \approx k_B T_e / e I_{si}$, or more colloquially just T_e/I_{si} when T_e is measured in electron volts. The slope is typically dominated by the exponentially-varying electron current. For small fluctuations in the floating potential, the plasma will act like a voltage source with output impedance R_p. This is will become clear below with the presentation of some typical measurement circuits.

This "DC" analysis actually applies to fluctuations in the plasma as well, as long as the fluctuation time scales are slow enough so that the sheath structure can instantaneously track the evolving plasma parameters ($n_\infty, V_{plasma}, T_e$, etc). Since the sheath is a few λ_D wide, and the typical ion speed in the sheath is c_s, the time scale for ions to cross the sheath is on the order of the ion plasma time: $\lambda_D/c_s \sim 1/\omega_{pi}$. This is the basic time-scale for the sheath structure to come into equilibrium, and therefore this DC analysis applies nearly up to the ion plasma frequency. However, on VTF we have observed a large band of fluctuations extending up the electron cyclotron frequency $\omega_{ce} \gg \omega_{pi}$. Therefore, there is motivation to extend our understanding of Langmuir probe operation above f_{pi} and this will be the focus of the RF Langmuir probe analysis below.

As a final step, we show two typical, *low-frequency* Langmuir probe circuits used to measure plasma properties on VTF. Figure 2-5(a) shows the typical circuit used to measure the floating potential V_{float} in the plasma. All that is required is to attach the Langmuir probe to a large load resistance R_L. (Here $R_L = R_2 + R_1$—on VTF we use a voltage divider since the floating potential can be large compared to voltages acceptable to the digitizers.) If R_L is very large, little current can flow from the plasma into the probe, so the probe must go to the floating potential. The precise condition is that $R_L \gg R_p$, where R_p is the "plasma resistance" defined above. The reason is that the plasma must source a small amount of current into the load resistor R_L to drive it from ground to the floating potential; the plasma can supply this current without deviating far from the floating potential if $R_L \gg R_p$.

A picture of the "load-lines" for the floating potential circuit is shown to the right on Fig. 2-5(a). The load-lines give a graphical solution to the (nonlinear) equations of the plasma and resistor network. (These are $I_L = I_p(V)$, $V = I_L R_L$, where $I_p(V)$ is the Langmuir characteristic for bias V at the probe tip, and I_L is the current through the load resistor R_L). The solution is the intersection of the plasma $I(V)$ curve (blue) and the load-

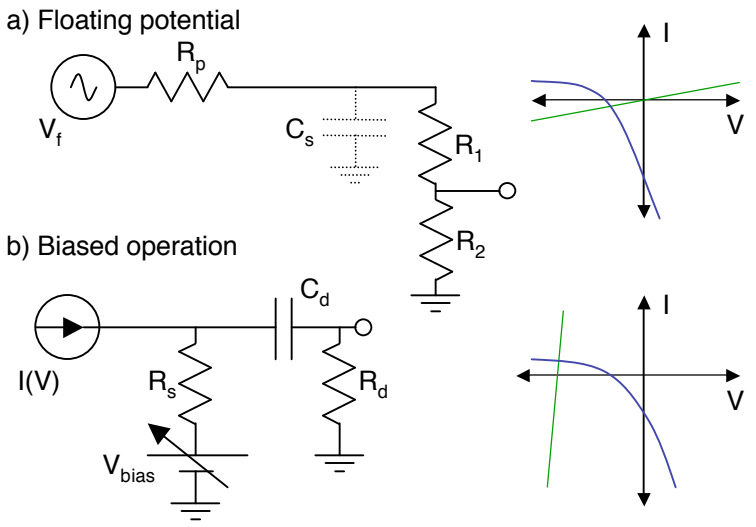

Figure 2-5: Low-frequency Langmuir probe circuits, and associated "load-line" pictures of how the bias and current into the probe are determined. (a) Floating-potential measurement: $R_L = R_1 + R_2 \gg R_p$. (b) Biased operation.

line $I = V/R_L$ (green). When $R_1 + R_2 \gg R_p$, then the intersection point will be close to the desired V_{float}. To summarize, the Langmuir probe behaves like a voltage source driving the voltage V_{float} through the output resistance R_p. A final note is that stray capacitance (C_s), can be a major problem for circuits of this type if they are to work at high frequencies; it causes a low-pass filter effect with a pole at approximately $f_{3dB} = 1/(2\pi R_p C_s)$ (when $R_L \gg R_p$).

A second probe circuit, this one used directly for mapping the $I(V)$ curve, is shown in Fig. 2-5(b). In this case, R_s is chosen *smaller* than R_p so now the plasma behaves like a current source with current $I(V)$, where $V \approx V_{bias}$. The sense resistor R_s converts the plasma current into a small voltage to be measured by digitizers. The load-line picture is again indicated to the right; the intercept $V = V_{bias}$ has been chosen large and negative, in the ion-saturation regime. This configuration is often used to measure the ion saturation current (Eq. 2.4); since I_{si} is proportional to ion density this is one of the simplest plasma density diagnostics.

Finally, Fig. 2-5(b) also shows an additional "decoupling" network (C_d, R_d), used specifically on VTF Langmuir probe circuits to decouple the offset V_{bias} for measurement by ground-referenced digitizers. This simple circuit works because VTF plasmas are relatively short-lived, about 1 ms, so $\tau_d = C_d R_d$ can be made much larger than any other experiment time scale. Therefore, the output voltage is simply $R_s I$. More sophisticated measurement

circuits use differential amplifiers to subtract off this offset.

2.2.2 RF Langmuir probes

The previous section described Langmuir probe operation at low frequencies, which turned out to be frequencies nearly up to the ion plasma frequency. It is necessary to extend this, however, because, as discussed in the forthcoming chapters, fluctuation power above ω_{pi} is observed. The chief difference discovered is an additional capacitive coupling through the sheath. This topic has been discussed in a number of papers [57–59], and in the monograph of Swift and Schwar [60]. At sufficiently high frequencies, the capacitive coupling can dominate the usual (resistive) coupling. Appendix B presents data supporting this theory both from broadband fluctuation measurements and measurements of electron hole waveforms.

At low frequencies, fluctuations in the plasma parameters appear as fluctuations in the $I(V)$ curve. Usually the most important is fluctuations in V_{plasma}, which causes the $I(V)$ characteristic to move back and forth. If the probe's bias point is near the floating potential, then a small shift V_1 in the plasma potential (with probe bias held fixed) will lead to a small current $I_1 = V_1/R_p$. Thus the dominant coupling at these low frequencies is simply resistive, and the plasma looks like a voltage source with output resistance R_p. One caveat is that the $I(V)$ curve can also distort due to changes in the ambient electron density, ion density, or even electron temperature. However, if the fluctuations are quasi-neutral (i.e. for wavelengths $\gg \lambda_D$) then the relative density fluctuations will be much smaller than the potential fluctuations, and the resistive coupling is recovered.

We now consider plasma-probe coupling in the regime $\omega > \omega_{pi}$ in greater detail. Here we find the coupling is still approximately resistive with the same coupling resistance R_p. An additional capacitive coupling C_p appears, however, physically due to finite electric fields (and therefore surface charges) at the probe. Flow of displacement currents to and from the probe to generate these surface charges are the manifestation of this capacitive coupling. Calculating these displacement currents requires knowledge of the sheath structure near the probe. However, a great simplification is available in the high-frequency regime, because the ions will not be able to keep up with fluctuating potentials, and therefore the sheath can be considered frozen in place. Furthermore, one can show that the sheath capacitance effect only becomes important (i.e. $R_p \approx 1/\omega C_p$) for ω a few times the ion plasma frequency. Therefore, when calculating this capacitive effect below the ions will be ignored.

The coupling of fluctuations V_1 in the space potential V_{plasma} onto the probe are now calculated. The boundary conditions (for purposes of calculating the coupling) are that the potential ϕ at the probe is held fixed at V_{bias}, and the potential at ∞ has become $V_{plasma}+V_1$. We split the potential ϕ into two pieces, $\phi_0(x)$ and $\phi_1(x,t)$. $\phi_0(x)$ is the equilibrium, steady piece of the potential, and contains the sheath structure around the probe; it takes on the values $\phi_0 = V_{bias}$ at the probe and $\phi_0 = V_{plasma}$ at ∞. As discussed above, the sheath structure in ϕ_0 is considered frozen on the time-scale of the fluctuations. ϕ_1 therefore goes from 0 at the probe surface to V_1 in the ambient plasma.

Similarly, the electron density will also have steady and fluctuating pieces: $n_0(x)$ and $n_1(x,t)$, which sum to give $n(x,t)$. The steady component n_0 is just the Boltzmann response to ϕ_0: $n_0(x) = n_\infty \exp(e\phi_0(x)/k_BT_e)$, where n_∞ is the ambient plasma density far from the probe.

The calculation of the fluctuating density n_1 is slightly subtle and depends on choosing the correct boundary condition on n_1 far from the probe—here we consider the case where the fluctuations are quasi-neutral, so that $n_1/n_\infty \ll e\phi_1/k_BT_e$. In general, because of the high electron mobility and repulsive potentials, the total density near the probe should still be in a Boltzmann equilibrium with the total potential, $n \propto \exp(e\phi_1/k_BT_e)$. However, a bit of thought is required at this point as to the correct normalization factor: for instance, the density is *not* simply $n = n_\infty \exp(e(\phi_0+\phi_1)/k_BT_e)$. If this were the case, the electrons far from the probe would have experienced a very strong density perturbation: $n(\infty) \approx n_\infty \exp(eV_1/k_BT_e)$, or equivalently $n_1/n_\infty \approx eV_1/k_BT_e$. This is an extremely large (and not quasi-neutral) density fluctuation. Instead, if one requires the fluctuations to be quasi-neutral, n_1 must be much smaller, something more like $n_1/n_\infty \approx (eV_1/k_BT_e)\times\lambda_D^2/L^2$ where L is the wavelength of the fluctuation.

Therefore, it is more appropriate to require $n_1(\infty)$ to be very small. Applying the limit $n_1(\infty) \to 0$ leads to

$$n \approx n_\infty \exp(e(\phi_0+\phi_1-V_1)/k_BT_e). \tag{2.6}$$

This has the correct far boundary condition: $n_0 \approx n_\infty$, and $n_1(\infty) \approx 0$.

The perturbed electron current is now found from using $\phi_1 = 0$ at the probe and

linearizing for small V_1:

$$I_{e1} = +\frac{eAn_\infty}{4}\sqrt{\frac{8T_e}{\pi m_e}}\exp\left(\frac{e(V_{bias}-V_{plasma})}{k_BT_e}\right)\times\frac{eV_1}{k_BT_e}. \tag{2.7}$$

Note that this is a positive current for positive V_1. Intuitively, this is expected: for $V_1 > 0$, the (negative) electron current will decrease, since now the probe appears to be at more negative potential with respect to the plasma, and therefore more electrons are repelled. Furthermore, in the specific case of $V_{bias} = V_{float}$, the result is exactly $I_{e1} = +eI_{si}/k_BT_e \times V_1 = V_1/R_p$, i.e. again we find a resistive coupling of the plasma to the probe through the plasma resistor R_p.

Next the capacitive coupling is calculated. This is determined by the (fluctuating) surface charge on the probe, which exists because of finite electric field $d\phi_1/dx$ at the probe surface: its magnitude is $\epsilon_0 \int d\mathbf{A}\cdot\mathbf{E}_1$. This electric field is in turn found from solving the fluctuating Poisson equation:

$$-\nabla^2\phi_1 = -en_1/\epsilon_0. \tag{2.8}$$

The fluctuating density n_1 can be found from linearizing Eq. 2.6 for small ϕ_1:

$$n_1(x) = n_\infty \exp(e\phi_0(x)/k_BT_e)\times\frac{e(\phi_1(x)-V_1)}{k_BT_e}. \tag{2.9}$$

This yields

$$\nabla^2\phi_1 = \frac{1}{\lambda_D^2}\exp\left(\frac{e\phi_0(x)}{k_BT_e}\right)\times(\phi_1 - V_1). \tag{2.10}$$

This equation is solved with the relevant boundary conditions, $\phi_1 = 0$ at the probe surface and $\phi_1(\infty) = V_1$. Equation 2.10 is a Helmholtz-like equation for ϕ_1, but note the spatial dependence in the pre-factor on the RHS contained in $\phi_0(x)$. The spatial dependence is actually quite strong—recall $e\phi_0/k_BT_e$ ranges from ≈ -5 at the surface of a floating probe to near zero outside the sheath. The character thus rapidly shifts from a vacuum-Poisson regime near the probe ($\nabla^2\phi_1 \simeq 0$) to a strongly-Debye-screened regime ($\nabla^2\phi_1 \simeq (\phi_1 - V_1)/\lambda_D^2$) just outside the sheath. The Laplacian can be solved in any geometry, though in the literature this particular problem has only been examined for the simplest, planar case [59]. However, the qualitative results are easily applied to spherical or cylindrical geometries.

Note that because this equation is linear in ϕ_1, dimensional analysis requires that

$\phi_1(x) \propto V_1$, so that potential and all electric field quantities simply scale linearly with the far boundary condition V_1. Therefore, the probe-plasma capacitance,

$$C_p = Q/V_1 = \frac{\epsilon_0 A}{V_1} \left. \frac{d\phi_1}{dx} \right|_a , \tag{2.11}$$

is a well-defined constant determined only by the geometry of the probe and sheath.

Equation 2.10 can be solved numerically using theoretical expressions for $\phi_0(x)$. However, it is not too hard to estimate the solution. Recall that for probes biased near the floating potential, $e\phi_0/k_BT_e \approx -5$ at the probe surface. This repels 99% of the ambient electrons, and electrons continue to be strongly repelled through most of the sheath, until the edge of the sheath where $e\phi_0/k_BT_e = -1/2$. Therefore within the sheath, Eq. 2.10 is essentially a vacuum Poisson equation. However, at the sheath edge, the Debye screening becomes important, forcing $\phi_1 - V_1$ to be small. Therefore, ϕ_1 will get most of the way to V_1 within the sheath, and so the solution is approximately that of a parallel plate capacitor (in linear geometry) or coaxial capacitor (if cylindrical), with conductor separation approximately equal to the sheath width. In linear geometry this gives [59],

$$C_p \approx \frac{\epsilon_0 A}{\delta}, \tag{2.12}$$

or, for cylindrical probes, as used in VTF,

$$C_p \approx \frac{2\pi\epsilon_0 l}{\log((a+\delta)/a)}. \tag{2.13}$$

In the latter, l is the probe length, a is the radius, and δ is the sheath width. This is the capacitive coupling constant between plasma and probe.

Finally, we estimate the quantity $\tau_p = R_pC_p$, which defines the corner frequency for the probe, above which it will have a rising, capacitive frequency response. Using the above estimates,

$$\tau_p \equiv R_pC_p \simeq \frac{k_BT_e}{eI_{si}} \times \frac{A}{\epsilon_0\delta} \approx \frac{1}{\omega_{pi}} \frac{\lambda_D}{0.6\delta}. \tag{2.14}$$

Therefore, typically the corner frequency is on the order of 3 f_{pi}, since typical sheaths are $\delta \simeq 5\ \lambda_D$. Note that this confirms our earlier approximation of ignoring the ions in the calculation. Finally, we have also made some numerical calculations of the DC and AC sheath structure based on the physics described here, and confirmed that these estimates

are correct, and that in cylindrical geometry the corner frequency is near 3 f_{pi}.

To summarize, at low frequencies we found resistive coupling between the probe and plasma for fluctuations about the floating potential. This connects smoothly to the same resistive coupling $R = R_p$ as the frequency crosses f_{pi}, above which the ions stop responding to fluctuating potentials. A capacitive component to the response enters here as well and becomes the dominant coupling when $f \gg f_{pi}$. The capacitive response was not calculated for $f < f_{pi}$, but its value is less important there because its effect will be small compared to the ordinary resistive coupling.

2.2.3 Fast Langmuir probe design

This section presents designs for "fast" Langmuir probes used to study plasma fluctuations. The main points driving the design are impedance matching of the fast signals and simplicity of design of the probe.

Typically, signals travel through 2–4 m of coaxial line ("coax") between the probe tip and the external oscilloscope. In the final iterations of the experimental setup, the oscilloscope was put very close to the vacuum feedthrough, minimizing the total coax length to about 2 m. Impedance matching typically becomes important when the length becomes about 1/4 of the wavelength of light in coax. In these coax conductors the dielectric is teflon, with a relative dielectric constant of about 2. Therefore, the speed of light is about 2.1×10^8 m/s, and the frequency for impedance matching is about 25 MHz (at 2 m). Since the ion-plasma frequency is typically 30-50 MHz, and the electron gyro-frequency is about 2 GHz, it is necessary that the design be impedance-matched.

Typical floating potential circuits (as illustrated in Fig. 2-5(a)) use a large load resistor in series with the probe tip. However, such a design will not automatically work at high frequencies. Discounting impedance matching for the moment, if the load resistor is far from the probe tip, this circuit is easily slowed down by parasitic capacitance in the lines (also illustrated in Fig. 2-5(a)). Typically, coax gives a capacitive loading of 100 pF/m. One way to overcome this is to put the top-half of the divider circuit (R_1 in the figure) very close to the probe tip. The parasitic slowdown will now be improved to $C_s R_2$ (when $R_2 \ll R_1$). Furthermore, if R_2 is the characteristic 50 Ω impedance of the transmission line, one arrives at an impedance-matched, floating probe design, with no parasitic slowdown. However, a difficulty of this design is construction of the probe tip in a compact area; even

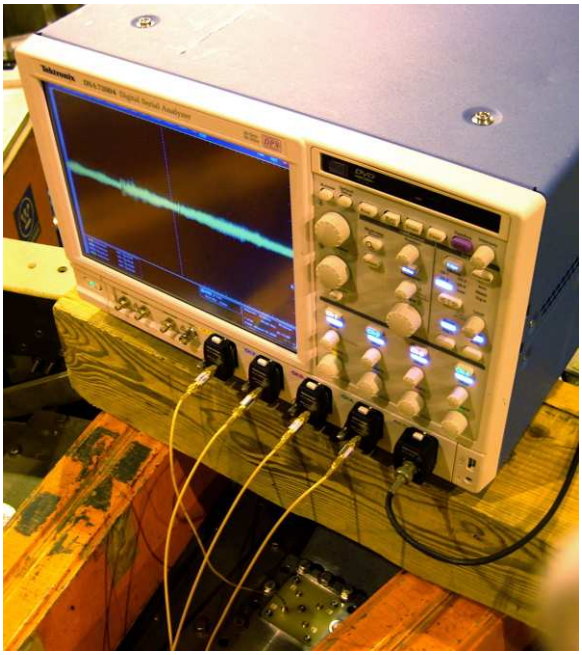

Figure 2-6: Oscilloscope installation atop VTF. Note coax segments to SMA vacuum feedthroughs and RF capacitors inline at scope input.

small surface mount resistors are larger than typical probe tips, and larger than the tip-tip *separation* of the finest-scale probe array used here.

Instead, the design used for fluctuation studies in this thesis is a "floating-current" probe. Essentially, we replace the load resistor R_1 with an RF capacitor. This opens up flexibility as the RF capacitor does not have to be at the probe tip or even in the vacuum chamber. A schematic of the entire system is shown in Fig. 2-7(a). Primarily, this design is useful because the probe tips are kept very simple, so many tips can be constructed in a small area. A further advantage is that the probe can still be used in other modes of operation (because there is no resistor hard-wired into the tip), such as in slow, biased mode [i.e. in Fig 2-5(b)]. Furthermore, one can easily experiment with other load circuits outside the vacuum vessel, such as RF bias-tees.

After the probe tip, the signals are carried through about 2 m of coax. Inside the vacuum chamber about 1.5 m of semi-rigid, 0.047" micro-coax (UT-047C/LL from Micro-Coax) carries signals from the probe-tips to SMA vacuum feedthroughs, and from there 30 cm of standard RG-316 coax completes the path to the oscilloscope. (The length of the lines was carefully matched to better than 0.5 cm to minimize skew in multi-probe timing and cross-correlation measurements.) Typically, we use a 4 nF RF capacitor (model

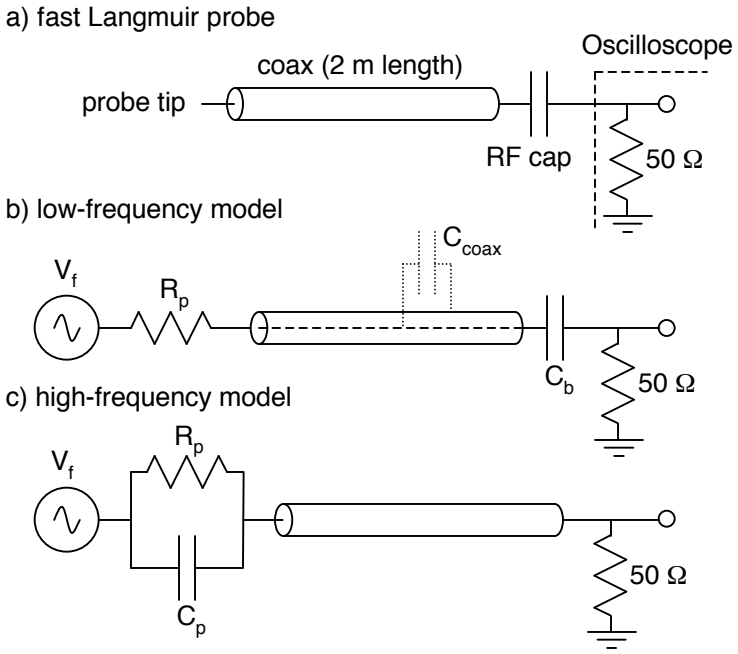

Figure 2-7: Schematic and equivalent low- and high-frequency circuit models for the fast Langmuir probes.

BLK-18+, from Mini-Circuits) as the blocking capacitor, placed at the oscilloscope.

Figures 2-8 and 2-9 show two versions of the fast Langmuir probes that are used for experiments reported here. The first has very finely spaced probe tips, ranging down to 0.8 mm. The probe tips are 2.5 mil (60 μm) Cu wire, with about 1 mm exposed to the plasma. This probe is used extensively in Chapter 5 to measure the size of electron hole structures observed in the plasma turbulence. Also attached to the probe structure is a single-channel electron energy analyzer (top), discussed below in Section 2.3, and a pair of magnetic coils to measure (B_r, B_z) for calibrating the position of the probe relative to the magnetic geometry. The probes are mounted on a 2-D probe drive which can scan them across the poloidal cross-section. The probes can further be rotated in the z–ϕ plane.

Figure 2-9 shows a second, flexible, fast Langmuir probe. Here the short lengths of coax between the tip and ceramic tube are flexible, allowing the probe-tip geometry to be reconfigured during a vacuum break. The probe tips here are simply the 12 mil (300 μm) silver-plated center conductor of the semi-rigid coax described above, with about 2 mm exposed to the plasma. The coax outer conductors are covered with a teflon sleeve and do not contact the plasma. A few different probe geometries have been used with this design, including a "fan" configuration with the probes spread over a 10 cm area in the poloidal

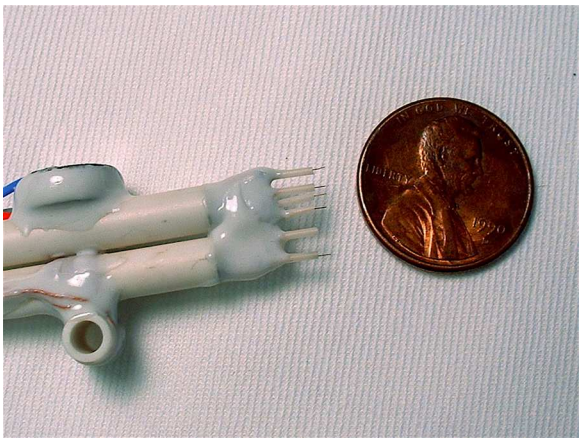

Figure 2-8: Finely-spaced fast Langmuir probe. Langmuir tip spacing ranges from 0.8 mm to 8 mm. Also visible here is a single-channel electron energy analyzer (top side of probe) and a pair of magnetic coils (bottom). The latter are used to calibrate the location of the probe with respect to the magnetic geometry.

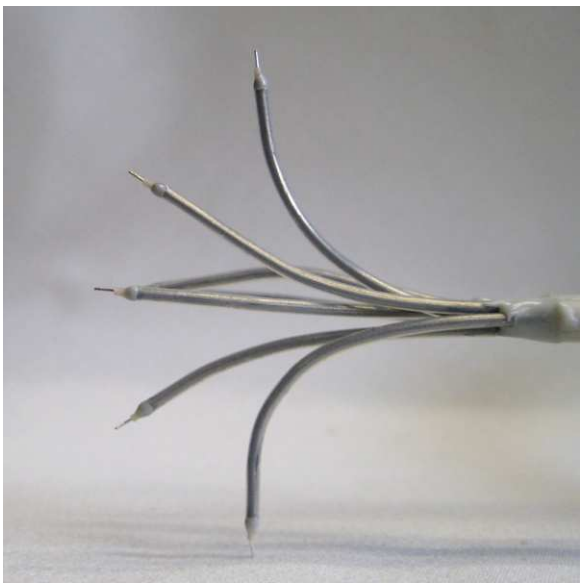

Figure 2-9: Flexible fast Langmuir probe. The probe-tip geometry can be reconfigured during a vacuum break.

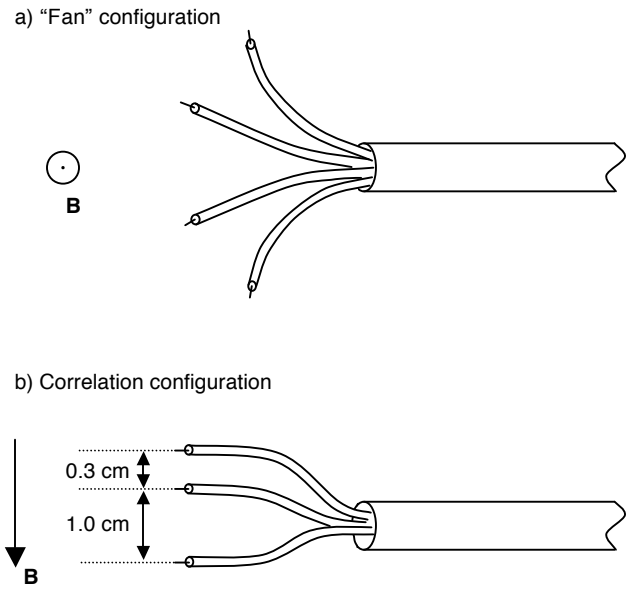

Figure 2-10: Schematic of the geometry of fast Langmuir probes. (a) “Fan” configuration for study of global spatial structures of the turbulence. (b) “Correlation” configuration for wavelength measurements.

plane to look for overall structure in the turbulence, and a “correlation” configuration with collinear probe tips for wavelength measurements. These are shown in Fig. 2-10.

Figure 2-7(b) shows the low-frequency model of the probe. Here, the plasma-probe coupling is a voltage source driving the line with a source resistance R_p. For typical probe geometries used, we estimate that R_p is about 2 kΩ. At these low frequencies ($\leq$ 25 MHz), the coax will not look like a transmission line, but rather as a 200 pF capacitor. This is small compared to the 4 nF blocking capacitor C_b, but is mentioned here because it provides a lower bound on how small C_b can fruitfully be. At low frequencies, $f < 1/(2\pi R_p C_b) \approx$ 20 kHz), C_b supplies a large impedance and therefore the probe tip floats. (Equivalently, the time-constant is about 10 μs.) On the output side, fluctuations below this frequency are high-pass filtered, which is useful because the floating potential is observed to swing up or down violently during reconnection events. Therefore, C_b provides the dual role of allowing the probe tip to float and attenuating low-frequency fluctuations, allowing the digitizer full-scale to focus on plasma fluctuations in the frequency ranges of interest.

Figure 2-7(c) shows the high-frequency model circuit. Here, the blocking capacitor C_b is not shown as it is small compared to the 50 Ω load for $f \gg 1/(2\pi 50 C_b) \approx$ 700 KHz. It therefore plays no role at frequencies relevant for impedance matching, ($f >$ 25 MHz), and the scope end of the transmission line appears correctly terminated at 50 Ω. At these

frequencies, plasma fluctuations see a pure 50 Ω load. Meanwhile, the plasma-probe coupling at these frequencies, as described above, is a paralleled resistor-capacitor. Therefore, in this range, the plasma-probe transfer function $H(\omega) = V_{out}/V_{in}$ is

$$\begin{aligned} H(\omega) &= \frac{50}{50 + \dfrac{R_p}{1 + i\omega R_p C_p}} \\ &= \frac{50}{R_p + 50}\,\frac{1 + i\omega C_p R_p}{1 + i\omega C_p R_{||}}. \end{aligned} \tag{2.15}$$

Here, 50 stands for the 50 Ω characteristic impedance of the line and termination, R_p is the "plasma-probe resistance," and C_p is the "plasma-probe capacitance" describing the additional capacitive coupling between probe and plasma that comes in at high frequencies. $R_{||}$ is the parallel of 50Ω and R_p. Significant simplifications can be made to this expression, since we estimate that $R_p \sim 2\text{k}\Omega \gg 50\Omega$ (for the flexible fast Langmuir probe), so therefore $R_{||} \approx 50\Omega$. Further, we have estimated that C_p is typically 0.2 pF, so $50\Omega \times C_p$ is an extremely short time, corresponding to frequencies near 20 GHz. Therefore, this expression simplifies to,

$$H(\omega) \approx \frac{50}{R_p}\,(1 + i\omega\tau_p). \tag{2.16}$$

Here $\tau_p = R_p C_p$ is the time constant for onset of capacitive plasma-probe coupling, the same as estimated in Eq. 2.14.

Here the chief limitation of our simple probe design becomes apparent: the output is attenuated compared to fluctuations in the plasma by the ratio $50/R_p$, and R_p is not known without other measurements and theory. Therefore, calibrations of the measured signals from the plasma are not excellent. Even though R_p is estimated from measurements of I_{si} and T_e, and we can gain further confidence from the observation of the capacitive τ_p effects, calibrated magnitudes of signals from the plasma will never be believable within more than about a factor of two. However, the models are believed to be reasonably correct, and one piece of evidence is that we observe a clear probe-area dependence in fluctuation amplitudes: the fine-scale fast Langmuir probes [2.5 mil (60 μm) diameter by 1 mm] measure approximately 1/10 the signal as flexible fast Langmuir probes [12 mil (300 μm) diameter by 2 mm length]. Further evidence supporting the capacitance effect is presented in Appendix B.

Poor absolute calibration is typical for Langmuir probes. However, these disadvantages are to be weighed against a simple design capable of measuring signals over a wide bandwidth (out to a few GHz), the ability of multiple probes to measure wavelengths, and to observe fast plasma fluctuations in the time-domain. This last aspect is crucial to the observations of coherent structures in the plasma turbulence in Chapter 5.

2.3 Electron energy analyzers

This section describes design and construction of gridded electron energy analyzers for measuring the electron distribution function during the reconnection events.

The simple Langmuir probes described above measure a sum of electron and ion currents. The current, as a function of the probe bias, has information about the distribution functions because only particles with sufficient energy to reach the probe are collected. Therefore, simple Langmuir probes can measure bulk properties like the electron temperature, and in principle can measure the electron distribution. However, this really only works for regions where the electron current to the probe dominates the ion current, i.e. not too far out on the tail. They cannot be used at all to measure the ion distribution function because the electron current completely dominates the ion current over the regions of interest.

To look at the tail of the electrons, or any part of the ion distribution, one has to separate the electron and ion currents to the probe. Gridded probes attempt to do just this, using extra grids to control which species and energies are able to reach a collector plate. They can therefore be used to measure the tail of the electron distribution, by rejecting ions and discriminating on electron energy, or measure the ion distribution by rejecting the electrons and then discriminating on ion energy. Figure 2-11 shows how a series of grids is used to reject slow electrons and all ions, collecting only the fast electron current.

Just as for simple Langmuir probes, electron current to the collector of a gridded probe is simply the current of electrons with energy large enough to overcome the retarding bias. In the designs used here, the areas of the collectors are much larger than the electron gyroradius, and the probe looks either up or down the magnetic field. Therefore it is the parallel component of the electron energy which determines which particles can reach the collector. With the grid biased to V_{bias} and the collector biased to reject all ions (the biasing

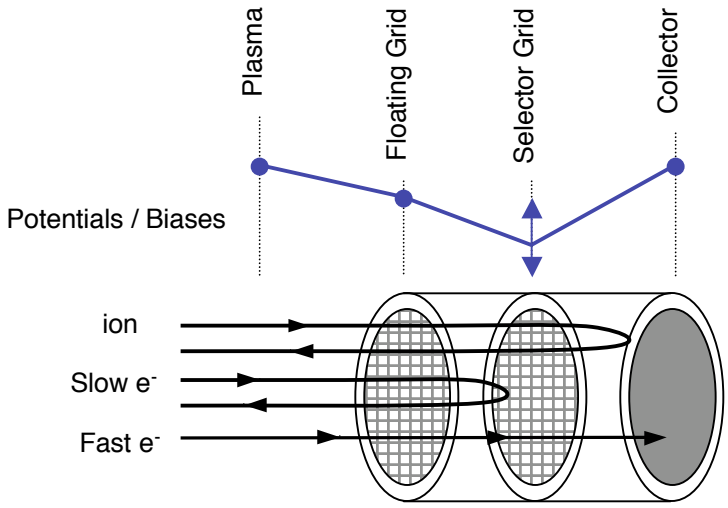

Figure 2-11: Cartoon of electron energy analyzer operation. The collector is biased strongly positive to avoid ion currents, and the negative selector or discriminator grid determines the threshold electron energy for reaching the collector.

scheme that was found to be successful on VTF), the collected electron current is

$$\begin{aligned} I_{coll}(V_{bias}) &= eTA\int_{v_c}^{\infty} v_{||} f(v_{||}) dv_{||}, \\ &= \frac{eTA}{m_e}\int_{\mathcal{E}_c}^{\infty} f(\mathcal{E}) d\mathcal{E}. \end{aligned} \tag{2.17}$$

Here $\mathcal{E}_c = m_e v_c^2/2$ is the critical energy to reach the probe, simply $e(V_{plasma} - V_{bias})$ (we will call this the "true bias point") and v_c is the associated critical parallel velocity. T is the transparency factor for the grids, and A the probe area. Under ideal conditions, one can measure I_{coll} as a function of V_{bias}, and take derivatives (or finite differences) to determine $f(\mathcal{E})$. Note that this is actually the *reduced* parallel distribution, i.e. integrated over the perpendicular velocities.

Gridded probes have a long history of use for measuring electron distribution functions in low-temperature, laboratory plasmas. Details of their construction and operation has been investigated by a number of authors [61, 62], including some of the additional challenges of measuring ion distributions rather than electron distributions.

Stenzel and Gekelman, *et al*, used an energy-analyzing probe in their reconnection experiments to measure the evolution of the electron distribution during reconnection [63]. Their probe employed a micro-channel plate instead of a grid. This had a much narrower angle of acceptance and therefore made point measurements in velocity space, accepting only

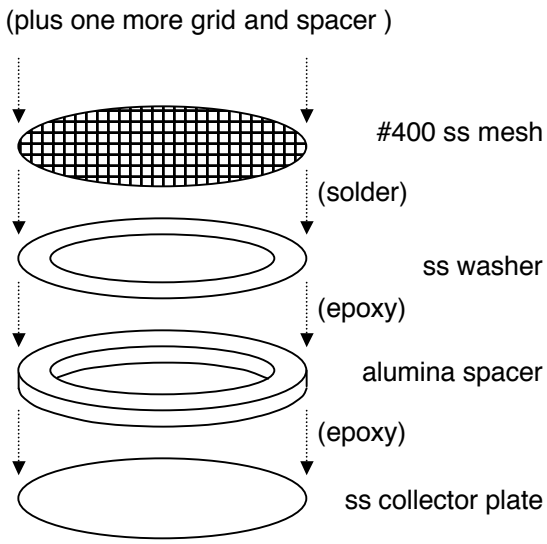

Figure 2-12: Construction of a single channel electron energy analyzer.

electrons with zero energy transverse to the plane of the probe (rather than integrating over these degrees of freedom, as simple gridded probes do). The probe could additionally be pointed over all 4π steradians. In an experimental *tour de force*, through extensive scans over reproducible discharges, they were able to measure the full 3-dimensional distribution function of electrons during the reconnection events on their experiment [46], finding extended "fingers" of fast electrons drawn out parallel to the reconnection electric field.

Some of the non-ideal aspects of these probes have also received attention in the literature. These include the problem of "grid-sag" [64], wherein the Debye shielding of the plasma screens the voltage on the grid, such that the space potential in the gaps between the wires is not quite what is applied to the grids. Therefore, more particles can leak through than otherwise expected, leading to overestimation of temperature. To avoid this, it is important that the grid spacing be less than the sheath length scale [61], which is a few Debye lengths in our case where the grid is negatively biased to discriminate electrons. The effect of space charge downstream from the initial grid has also been studied [65, 66]. Here it is found that a potential maximum can form between the grids if they are spaced larger than a few Debye lengths apart. This is a greater problem for probes designed to measure the ion-distribution function, since this maximum acts like a virtual grid which can reflect ions; it may actually help [66] an electron energy analyzer such as ours.

Two types of energy analyzer probes have been constructed for use on VTF. The first follows the schematic in Figure 2-12, consisting of a floating grid, biased grid, and collector.

The grid layers are constructed from 400-gauge stainless steel mesh (alloy 304), woven from 1 mil diameter wire, with a 1.5 mil inter-wire gap and nominal transparency of 36%. (This 1 mil length is approximately the Debye length for VTF plasmas.) The mesh is soldered onto stainless steel washers punched from shim stock. Layers are separated from one another by < 1 mm alumina washers cut from an alumina tube (3/8" OD, 1/4" ID). The collector plate is also punched from stainless steel shim stock. Layers are assembled and sealed from the outside using vacuum-compatible epoxy. The final collector diameter is 6.3 mm. Typically, these energy analyzers are piggy-backed onto another probe, and for instance is visible in Fig 2-8.

This single grid/collector probe was able to see evidence of energization of electrons during the reconnection events; results are presented in the next chapter. However, the reconnection events on VTF have been found to be not highly reproducible, so a seven-channel energy analyzer probe was designed and constructed to collect data at multiple biases simultaneously. Seven such grid/collector pairs are laid out for manufacture on printed circuit board (PCB), using the circuit board schematic shown in Figure 2-13. Construction on circuit boards allows much finer features compared with construction by hand. For instance, the grid and collector diameters have been scaled down to 3 mm from the 6.3 mm used on the single-channel probe, and the final probe head occupies an area of about 1.5 cm $\times$ 1.5 cm. Three separate circuit layers, one for collectors, one for biased grids, and one for a floating grid, are patterned on 0.75 mm FR-4 (fiberglass/epoxy) substrate. These are cut apart and eventually epoxied one atop the other.

For the grids layers, a standard printed circuit board "via"—a drilled and plated "through-hole" plus annular copper "pad"—takes the the place of the alumina spacer and stainless steel washer of the single-channel probe. To create the grids, the copper plating is removed from the wall of the through-hole and the 400-gauge stainless steel mesh is soldered to the remaining copper ring. After soldering, mesh outside the pad is carefully excised to prevent adjacent grids from being electrically shorted. On the floating layer, however, there is only one grid which covers all holes, and therefore only one electrical connection. The collectors are simply tinned copper pads of equal diameter to the holes on the grid layers; no modification to this layer is required. The 3 layers are stacked and epoxied together, lining up the grids on the floating and biased grid layer with the collectors, completing the three-layer, seven-channel energy analyzer. Patterned circuit board traces provide electrical

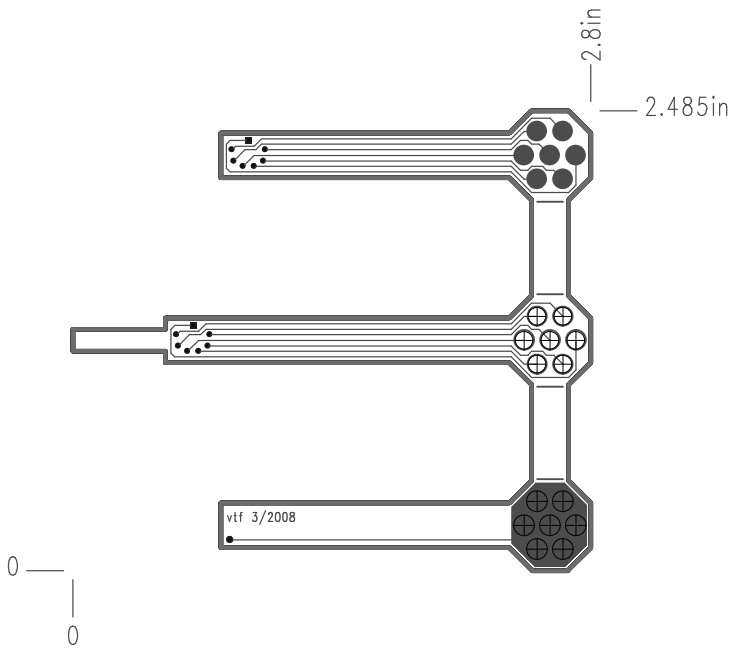

Figure 2-13: Printed-circuit board schematic for the three layers of a 7-channel energy-analyzing probe.

connection from the collectors and grids to a set of solder points about three inches away from the probe head. Wires are soldered here to provide flexible connection to a vacuum feedthrough, eventually connecting to biasing and measurement circuits outside the vacuum chamber. After soldering, the wires are fed down a ceramic tube into which the tongue of the grid layer is epoxied. These solder points are also potted in vacuum epoxy. Photographs of the layers before and after construction are shown in Fig 2-14.

2.4 Summary

This chapter has reviewed the experimental tools used for studies conducted in this thesis. The VTF device creates low-temperature plasmas with magnetic field geometry suitable for study of magnetic reconnection in the strong-guide field regime. Plasma is built up over about 1 ms of ohmic heating before the plasma is driven into a current sheet. Novel magnetic flux probes conceived by the VTF group measure the evolution of the poloidal flux function Ψ, which is crucial to observing the global magnetic geometry and reconnection of this current sheet.

The author has developed and constructed RF, or "fast" Langmuir probes suitable for

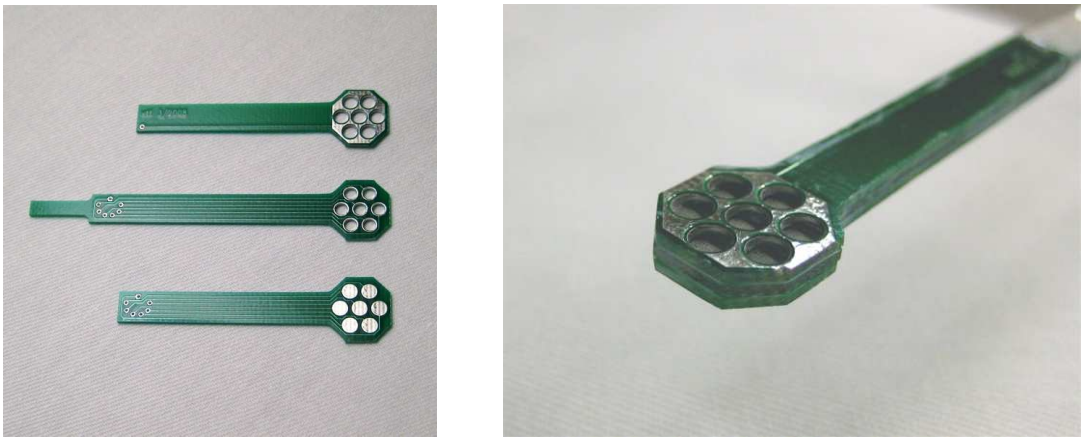

Figure 2-14: The 3 layers of a seven-channel energy-analyzer probe before and after assembly. (The floating grid has not been soldered on yet.)

studying fast fluctuations during the reconnection events. This chapter has also discussed theoretical operation of the probes, including the resistive and capacitive coupling of plasma fluctuations onto the probes.

Finally, electron energy-analyzing probes have been constructed for measuring populations of fast electrons energized by the reconnection events. This includes a novel, multiple-channel energy analyzer constructed using printed circuit board techniques, which integrates seven grid/collector pairs into a small area.

Chapter 3

Reconnection Results

This chapter presents baseline observations of magnetic reconnection in the VTF experiment to motivate and establish the necessary background for experiments on plasma fluctuations to be presented in the next chapters. First we will discuss observations, using the magnetics diagnostics, of the formation of a plasma current sheet and the release of its stored magnetic energy by reconnection events. Recent experiments [52] have identified a "spontaneous reconnection" regime, where the current sheet is found to be stable for 100's of μs before suddenly undergoing a reconnection event which releases the magnetic energy on a time scale of about 10 μs. Finding the "trigger" mechanism for this fast reconnection state is now a primary goal of experiments on VTF.

The observed time-variation of the reconnection rate is actually very useful for experimentally discerning which mechanisms play an important role in controlling the reconnection process. If current-driven turbulence is the cause of fast reconnection in VTF, then we expect to establish tight temporal correlation between the relevant fluctuations and the reconnection rate. On the other hand, time delay between reconnection and fluctuations, or persistence of fluctuations long after the reconnection events would imply that the reconnection process gives rise to the fluctuations (perhaps by generating short gradient lengths or creating populations of energetic particles prone to kinetic instability) but that ultimately these fluctuations do not play a crucial role in the reconnection process.

Besides observations of the geometry of the current sheet and dynamics of the energy release, it is found that critical (runaway) electric fields are approached or exceeded during the reconnection events. In addition, fluctuations (discussed in the next chapters) observed

in conjunction with the reconnection events, have features which imply they are likely driven by energetic particles. This inspired a search for particle energization by the reconnection events. These studies are conducted using gridded electron energy analyzers described in the previous chapter. These observations are useful in their own right, since the topic of high-energy electron production has been a long-debated aspect of reconnection research. Furthermore, within this thesis, they are important because energetic (non-Maxwellian) electrons are an additional source of free energy to drive instabilities in the plasma.

3.1 Basic reconnection observations

This section discusses observations of reconnection events on VTF, primarily using the magnetic flux probe diagnostics discussed in the previous chapter. This enables observation of the formation of a current sheet and its disruption due to reconnection events. The current sheet is found to relax from an elongated, stretched magnetic field geometry to a "potential" magnetic geometry ($\nabla \times \mathbf{B} \simeq 0$), again indicating loss of stored magnetic energy. It is shown that the reconnection electric field arises in association with the inductive decay ($-dI/dt$) of the current sheet. A study is made of the evolution of an inferred plasma resistivity, $\eta \equiv E_\phi / j_\phi$ evaluated at the reconnection x line. It is found that this quantity increases by about a factor of 5 during the reconnection events. Finally, we will discuss the evolution of a few important, dimensionless quantities during the reconnection events, the ratio of the electric field to the Dreicer, or "runaway" electric field, and various drift parameters, which are the ratio of the relative electron-ion drift comprising the plasma current (j/ne) to the thermal speeds of the individual species. This is important information toward understanding what instabilities can be driven in the plasma.

Figure 3-1 shows an example of a typical reconnection event in VTF. Time $t = 0$ to 1200 μs is the ohmic heating phase of the experiment, which builds up the plasma current and density. In this discharge, the reconnection drive is applied at 1200 μs, which pulls the plasma into a current sheet. The reconnection event, which disrupts the plasma current sheet and releases the magnetic energy stored there, peaks at about $t = 1380$ μs. Here the plasma current dropped by about 40%. Associated with this magnetic energy release is the inductive, toroidal electric field E_ϕ, which is the reconnection electric field.

Figure 3-1(c,d) show color profiles of Δj_ϕ and E_ϕ during the reconnection event. Dashed

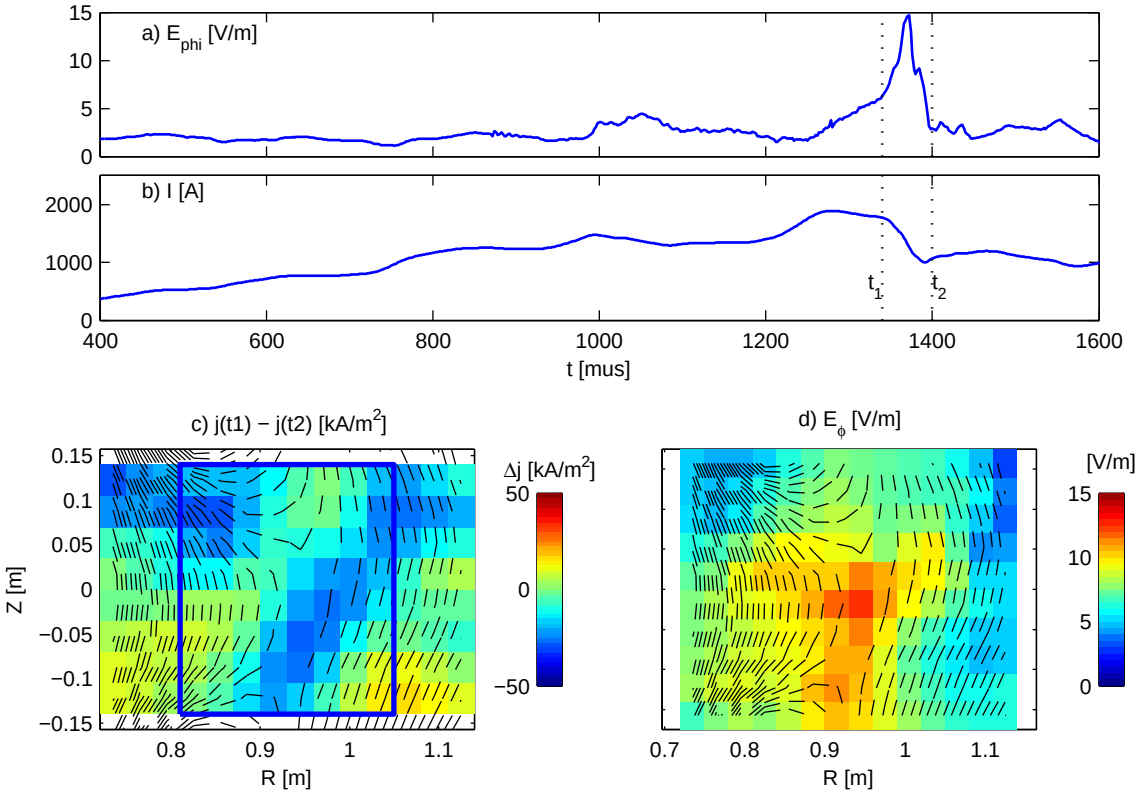

Figure 3-1: Typical measurements from the flux array during reconnection events. (a) Toroidal electric field evaluated at the x line. (b) Toroidal plasma current (integrated over the blue box denoted in (c). Characteristic times before ($t_1 = 1340$ μs) and after ($t_2 = 1400$ μs) reconnection are denoted as well. (c) Change in current density from t_1 to t_2 showing loss of current from the current sheet. Dashed lines are Ψ contours at t_1. Moderate spatial smoothing is also applied using the the 3×3 gaussian smoothing matrix s_{ij}, $s_{22} = 0.83$, $s_{12} = s_{21} = s_{32} = s_{23} = 0.04$ with $s_{11} = s_{13} = s_{31} = s_{33} = 0.002$. j_ϕ measurements at the top and bottom edge or the box are also suppressed here. (d) Reconnection electric field $(-1/R) \times \partial\Psi/\partial t$ evaluated at time $t = 1370$ μs, at the peak of the reconnection event.

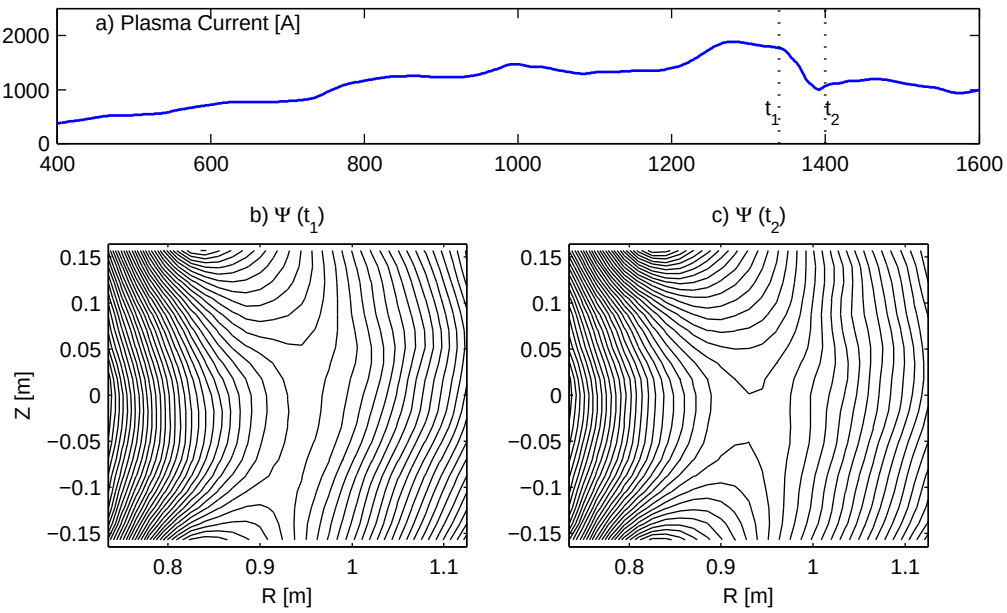

Figure 3-2: Evolution of Ψ across a reconnection event. (a) Toroidal plasma current. (b,c) $\Psi = \int_0^R B_z R dR$ evaluated before and after reconnection events. Contour interval is 50×10^{-6} Tm^2.

lines in these figures show contours of Ψ evaluated at a time immediately before the reconnection event (at time $t_1 = 1340$ μs), showing the stretched state of the magnetic field. (Recall Ψ contours correspond to poloidal magnetic field surfaces with $\mathbf{B} \cdot \nabla \Psi = 0$.)

Figure 3-1(c) shows the measured change in current Δj_ϕ across the reconnection event. Most of the current is lost from the current sheet itself. Here j_ϕ has been calculated from the measured Ψ using a finite difference approximation to Ampere's law. This figure also shows, as a blue box, the region over which we typically evaluate the total plasma current [as for Fig. 3-1(a)], via Ampere's law $\mu_0 I = \int \mathbf{B} \cdot d\mathbf{l}$. Finally, E_ϕ measurements during this reconnection event are shown in Fig. 3-1(d). Typically we find that the toroidal electric field peaks within the current sheet, as is shown here. The location of the x line is calculated directly from the flux function measurements. Therefore E_ϕ can be evaluated evaluated at the location of the evolving x line; this is what is used for later plots (such as Fig. 3-1(a)) unless otherwise specified. Typically we do not find large time variations between electric field evaluated at the x line versus averaged over the cross section. The averaged electric field tends to be 20-50% smaller, however, depending on how large a region is averaged, because of the peaking at the x line.

Figure 3-2 shows in more detail the relaxation of the magnetic field due to reconnection.

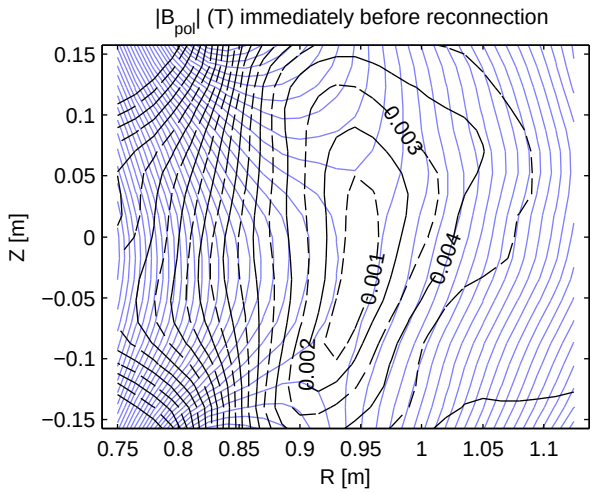

Figure 3-3: $|B_{pol}|$ in the current sheet. Black solid and dashed contours are $|B_{pol}| = (B_R^2 + B_z^2)^{1/2}$ evaluated at time t_1 (of Fig. 3-2), immediately before the reconnection event. Contour interval is 1 mT. Light blue contours are Ψ for reference.

Figure 3-2(a) shows the total plasma current over the discharge, and indicates two times, t_1 = 1340 μs and t_2 = 1400 μs which bracket the reconnection event. Figure 3-2(b) shows contours of Ψ at t_1, immediately before the reconnection event, where characteristic stretching and energy storage in the magnetic field is apparent. In contrast, after the reconnection event, as shown in Fig. 3-2(c), the field relaxes to a lower energy, "potential" structure. Such a potential field structure has $\nabla \times \mathbf{B} \simeq 0$, so that the field reversal region is an open "x" geometry rather than a current sheet and has less magnetic energy than a stretched sheet.

Figure 3-3 shows contours of poloidal magnetic field $|B_{pol}| \equiv (B_R^2 + B_z^2)^{1/2}$. At the current sheet the poloidal field reverses and therefore $|B_{pol}|$ is at a minimum there. We find a typical magnetic field strength "upstream" of the current sheet of 2–3 mT. The maximum aspect ratio of the current sheet, at its most stretched, is about 5.

The reconnection electric field is associated with inductive decay of the current sheet. Figure 3-4 shows a scatter plot of pairs $(V_{loop}, dI/dt)$ for times near the reconnection events over approximately 40 discharges. Here $V_{loop} \equiv 2\pi R_x E_{rec}$, where R_x is the radius of the x-line and E_{rec} is the electric field evaluated there. dI/dt has been evaluated from the contour shown in Fig. 3-1(c). (Slightly higher or lower (by 20%) values will be measured if larger or smaller areas are used, though this contour captures at least 80% of dI/dt.)

It is found that $\Delta V_{loop} \propto -dI/dt$. (Note that there is also finite offset in V_{loop} even

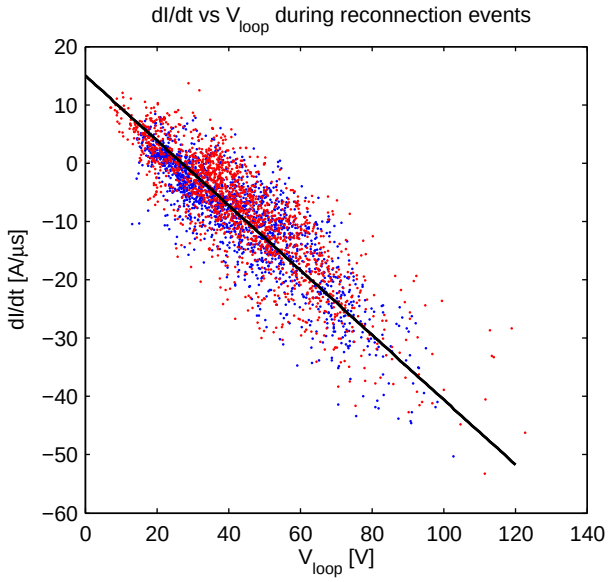

Figure 3-4: Inductive nature of the reconnection events. Instantaneous values of $V_{loop} = 2\pi R E_\phi$ evaluated at the x line and dI/dt evaluated over the 25 cm $\times$ 30 cm area (as in Fig. 3-1(c)) which is centered on the current sheet. Blue and red points are measured by the two separate probe arrays on opposite sides of the vacuum chamber.

when $dI/dt = 0$.) The black line in the figure indicates a proportionality constant L, so that $\Delta V_{loop} = -L dI/dt$. The experimentally measured $L \simeq 1.8 \times 10^{-6}$ H. This is slightly less than the nominal L calculated from the standard formula imagining that the plasma is a simple toroidal loop, $L_0 = \mu_0 R_0(\log(8R_0/a) - 7/4) \approx 2.4 \times 10^{-6}$ H, based on the major radius $R_0 = 0.92$ m, and a plasma radius $a = 0.15$ m. This may indicate additional screening effects due to "perfectly conducting" internal toroidal conductors, the closest of which are about 25 cm away from the current sheet. It is also possible that outer, unmeasured flux surfaces take over the current from the current sheet, providing a similar screening effect.

Overall, finding inductive response is not too surprising. Assuming axisymmetry, the toroidal component of the vector potential A_ϕ and the toroidal current density j_ϕ are related by a Green's function [67, Eq. 5.37], so that

$$A_\phi(R,z) = \int dR'dz'\, G(R,z;R',z')\, j_\phi(R',z'). \tag{3.1}$$

This integral is to be taken over all space. Meanwhile, the plasma current is measured over the current sheet (since the probe array only measures Ψ between the central pair of

internal conductors), which is therefore expressed by

$$I = \int_{CS} dR'dz'\ j_\phi(R', z'). \tag{3.2}$$

Therefore, finding an inductive relationship between $E_\phi = -\partial A_\phi/\partial t$ measured at a given point (R, z), (i.e. at the x line) and the total current lost requires the proportionality

$$\int_{CS} dR'dz'\ \Delta j_\phi \propto \int dR'dz'\ G(R, z; R', z')\ \Delta j_\phi(R', z'), \tag{3.3}$$

where Δj_ϕ is the current density change during the reconnection event. For Fig. 3-4, E_ϕ has been evaluated where it is maximum, but this does not change the argument substantially since E_ϕ is finite over an extended region near the current sheet.

For the discussion here, the most important idea is that the convolution of j_ϕ through G is a smoothing operation (a localized change in current leads to electric fields over the whole cross section), but one that still peaks for $R = R'$ and $Z = Z'$. There may be other currents driven in the plasma (or in the internal conductors) as a result of the reconnection event, and indeed this is suggested by the disagreement between the inferred inductance and the standard formula, but the localization of ΔA_ϕ through the Green's function combined with the localized loss of current from the current sheet yields an overall inductive response.

The reproducibility of the inferred L is an indication that the geometry of the current sheet is reasonably similar between discharges. However, the particulars of the geometry are not too essential: recall, for instance, that the self-inductance of a current ring depends only logarithmically on its minor radius a.

Finally, we discuss the possibility (and requirements) for anomalous resistivity as a mechanism for reconnection events. Figure 3-5 shows a plot of toroidal electric field (a), current density (b), and their ratio E_ϕ/j_ϕ (c). Such a proportionality exists assuming an Ohm's law

$$\mathbf{E} + \mathbf{v} \times \mathbf{B} = \eta \mathbf{j}. \tag{3.4}$$

In this plot, electric field and current density are both evaluated at the reconnection x line, so therefore one assumes that $\mathbf{v} \times \mathbf{B} \simeq 0$, because $\mathbf{B}$ is entirely toroidal there, leaving only $E_\phi = \eta j_\phi$. (Note that, however, in general $\mathbf{v} \times \mathbf{B}$ is expected to be very important, balancing the reconnection electric field over most of the plasma cross section, and breaking

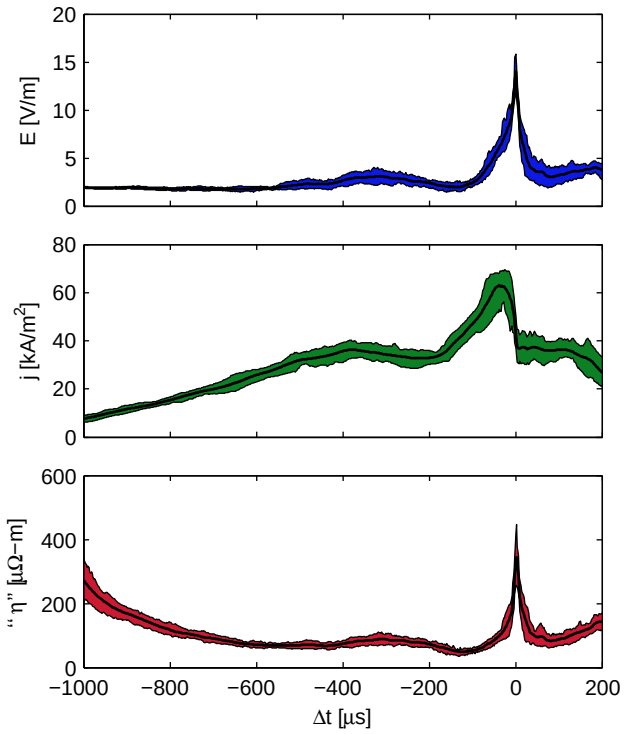

Figure 3-5: Electric field, current density, and ratio over the entire discharge. (a) Toroidal (reconnection) electric field evaluated at the x line. (b) Current density evaluated at the x line. (c) $\eta \equiv E/j$, inferred "resistivity" from ratio of electric field to current density.

down only near the current sheet. Experiments on VTF have not yet established in detail the area over which $\mathbf{v} \times \mathbf{B}$ ceases to balance E_ϕ. If this is smaller than the finite region over which j_ϕ is measured by the probe array, then η inferred from the simple E_ϕ/j_ϕ here will be in error. This is a high priority of ongoing experiments.)

A large number of shots have been aligned to the reconnection event, defined as time $\Delta t = 0$ based on the peak toroidal electric field. Colored bands indicate the "1-σ" group, so that 67% of all discharges land within the colored band, with the black curve indicating the mean. The standard sequence of events, plasma build-up by ohmic heating, application of the reconnection drive ($\Delta t \approx -200\mu$s), and the reconnection event ($\Delta t = 0\mu$s) are all evident. Typically the toroidal electric fields are 2 V/m for most of the discharge but reach 15 V/m during the reconnection events. Current densities in the current sheet range up to 60 kA/m^2 immediately before the reconnection event, and typically half of the current density is lost as part of the magnetic relaxation.

Finally, Fig. 3-5 plots the inferred η, which is seen to evolve through the discharge. Initially ($\Delta t \approx -1000$ μs), it is found to be large but decreasing. This is consistent with the

following plasma startup scenario: initially the plasma is only weakly ionized and therefore has extra "neutral" resistivity η_0 provided by electron-neutral collisions. These contribute a resistivity of the form [68]

$$\eta_0 \sim \frac{m_e \nu_{e0}}{ne^2} \sim \frac{n_0}{n} \frac{m_e v_{te} \sigma_{e0}}{e^2}. \tag{3.5}$$

Here n_0/n is the ratio of neutral gas density to plasma density, and σ_{e0} is the electron-neutral cross-section. As the discharge progresses, the plasma is becoming better-ionized, and this is consistent with the decrease in n_0/n and therefore the neutral resistivity.

Eventually, the resistivity is found to saturate (near $\Delta t \approx -600$ μs). This can potentially be due to two effects: First, the plasma density and neutral density may be saturating at this stage, so that n_0/n becomes a constant. The typical densities at this stage are 1–2×10^{18} m^{-3}, which is a moderate fraction of the initial neutral fill density (3.5×10^{18} m^{-3}). However, it is unlikely that neutral density would become a constant, as the neutral ionization rate $\sim n\langle \sigma_{ion} v \rangle$ *increases* with increasing plasma density; this works to totally burn out the neutral gas. Simple estimates find a characteristic time of only ~ 100 μs to ionize the remaining 2×10^{18} m^{-3} neutrals, once $n \simeq 1 \times 10^{18}$ m^{-3}, using $T_e = 15$ eV and the ionization cross-section for argon ($\simeq 2 \times 10^{20}$ m^{-2}, for $\mathcal{E} \gtrsim 30$ eV, going to zero at the threshold of 15.75 eV) [69]. Therefore, it is possible that neutrals are almost completely burned out of the plasma.

Therefore, a second, likely more important effect, is that as the plasma becomes better-ionized the resistivity becomes dominated by Spitzer resistivity η_{Sp} [70], which results from electron-ion collisions; it has no density dependence due to equal numbers of charge carriers and scattering centers. Therefore, this predicts that the total resistivity $\eta = \eta_{Sp} + \eta_0$ saturates once there is enough plasma density so that $\eta_0 < \eta_{Sp}$.

Quantitatively, Spitzer resistivity is given by the formula,

$$\eta_{Sp} = 0.53 \times 10^{-4} \; Z_{\mathit{eff}} \log \Lambda \, (T_e/[eV])^{3/2} \;\; \Omega\text{-m}. \tag{3.6}$$

In this formula, $\log \Lambda \simeq 12$ is the Coulomb logarithm, and Z_{eff} is the mean charge state of the ion species, $Z_{\mathit{eff}} = (\sum_Z Z^2 n_{iZ})/(\sum_Z Z n_{iZ})$, where n_{iZ} is the number of ions in charge state Z.

Z_{eff} has not been studied in detail for VTF plasmas. However, it may be larger than 1,

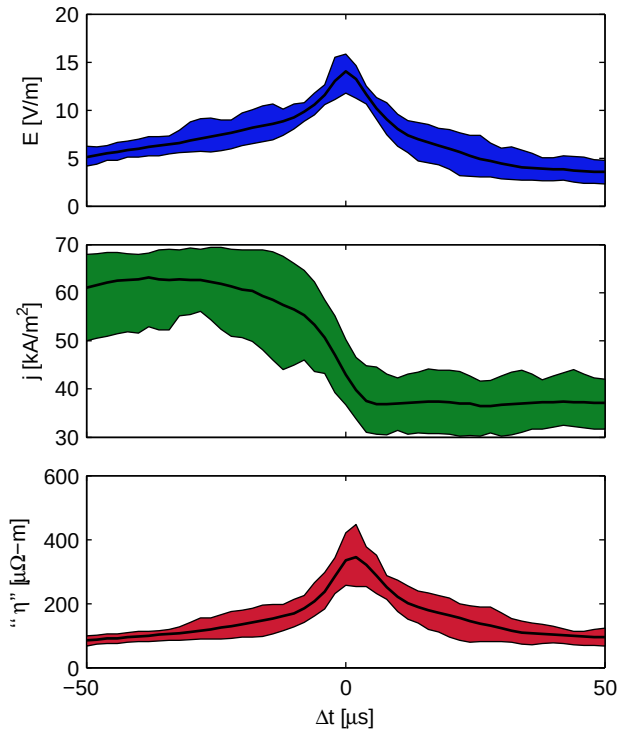

Figure 3-6: Electric field, current density, and ratio over the short time scale of the reconnection events. (a) Toroidal (reconnection) electric field, evaluated at the x line. (b) Current density evaluated at the x line. (c) $\eta \equiv E/j$, inferred "resistivity" from ratio of electric field to current density.

because the high-energy portion of the 15 eV electron population will have enough energy to ionize argon atoms to their second and third (and higher) ionization states. (The first four ionization energies of argon are 15.75, 27.6, 40.7, and 59.8 eV [71].) Some simple estimates of the ionization rates into higher ionization states of argon (using the "universal" ionization cross sections in Ref. [72]) indicate that there is enough time during the 1 ms of ohmic heating to reach the doubly and perhaps triply ionized state of argon.

The inferred saturated resistivity is moderately higher than the calculated Spitzer parallel resistivity, which is estimated to fall in the range from 15 to 25 $\mu\Omega$-m for electron temperatures from 10 to 15 eV. In contrast, the inferred η for $\Delta t = -400$ to -200 μs is near 60–80 $\mu\Omega$-m. It is possible that some residual neutral effects, $Z_{eff} > 1$, and possibly even current-driven turbulence affect the resistivity here.

This thesis has not made more detailed study of the baseline resistivity in VTF, and instead focuses on the plasma dynamics during the reconnection events. During the reconnection events ($\Delta t = 0$) the electric field increase is accompanied by the inductive *decrease*

in plasma current as discussed above. This is not compatible with any constant resistivity, and indeed the inferred resistivity has a spike which largely parallels the electric field, and typically rises by about a factor of 5. Figure 3-6 zooms in on the 100 μs surrounding the reconnection event. The inferred η is seen to track the electric field closely, with a slight (2–4 μs) delay due to decreasing j.

3.2 Runaway electric fields

The inductive electric fields during the reconnection events approach or exceed the "Dreicer," or runaway electric field [70, 73]. This is the characteristic electric field required to overcome the electron-ion collisional drag. Given sufficient time, and barring other loss mechanisms of the fast particles, such fields can accelerate electrons to very high energies. This follows because the classical electron-ion collision cross section $\sigma(\mathcal{E}_{CM})$ falls with the square of the center-of-mass energy $\mathcal{E}_{CM}$ for the colliding particles. Therefore the energy loss per unit distance, for a particle with energy $\mathcal{E}$, scales with $n\sigma(\mathcal{E})\mathcal{E}$, and begins to decrease as soon as $\mathcal{E}$ is large enough to set $\mathcal{E}_{CM}$; i.e. when $\mathcal{E} \gtrsim k_B T_e$. Because the drag force decreases with energy, electrons can "runaway" to large energy. In classical theory, the characteristic field which leads to runaway of the electrons is the Dreicer field E_D; such a field accelerates a thermal electron by one thermal velocity in one collision time. In Ref. [73] it is given as

$$eE_D = nm_e \frac{e^4}{4\pi\epsilon_0^2 m_e^2} \frac{m_e}{2k_B T_e} \log\Lambda. \tag{3.7}$$

E_D typically is found to be about 12 V/m based on temperatures of 15 eV and densities of 1×10^{18} m^{-3}; this is summarized with a number of other parameters in Table 3.1.

We have calculated the drag force on fast electrons due to bulk electrons, ions, and residual neutral gas for VTF parameters. For electrons and ions, the drag force is calculated from classical collision theory in Ref. [70]. The collisional drag is $m_e \nu_s v$, where ν_s is the "slowing-down" collision rate for fast electrons with a given species, and v is the speed of the fast electron. These are converted to an equivalent critical electric field $E_c = m_e \nu_s v/e$, which is the electric field required to exceed the drag force. For drag on ions, this is given by

$$E_c^i = \frac{Z_{eff} n e^3 \log\Lambda}{4\pi\epsilon_0^2} \times \frac{1}{2\mathcal{E}}, \tag{3.8}$$

where $\mathcal{E}$ is the energy of the fast electron. The drag on bulk electrons has a more complicated functional form

$$E_c^e = \frac{ne^3 \log \Lambda}{4\pi\epsilon_0^2 k_B T_e} \times 2G\left((\mathcal{E}/k_B T_e)^{1/2}\right), \tag{3.9}$$

where $G(x)$ is the Chandrasekhar function, which peaks near $\mathcal{E} = k_B T_e$, but at high energies falls off $\propto 1/\mathcal{E}$ just like ion drag.

Finally, neutral collision effects on fast electrons are estimated here from the "momentum-loss" cross-section σ_m, which is tabulated as a function of energy $\mathcal{E}$. This is related to the drag force using $\nu_m = n_0 \sigma_m v$, giving an equivalent critical electric field $E_c^n = m_e \nu_m v/e = 2n_0\sigma_m(\mathcal{E})\mathcal{E}/e$. The momentum-loss cross-section has been compiled in a recent experimental review article [74]. However it should be noted that large experimental uncertainties remain; this is due in part to the difficulty in measuring the (dominant) small-angle limit of the scattering cross sections in the typical crossed-beam experimental apparatus.

The equivalent critical electric fields due to electrons, ions, and neutrals are plotted as a function of energy in Figure 3-7, using a plasma density $n = 1 \times 10^{18}$ m^{-3} and neutral density $n_0 = 2 \times 10^{18}$ m^{-3}. (Recall that the neutral density may be lower due to burn-out. It is included here as a conservative upper bound. Also, we have assumed $Z_{\mathit{eff}} = 1$.) High-energy neutral cross-sections have been extrapolated from available experimental data. The cross-section appears to scale as $1/\mathcal{E}$ for energies larger than 10 eV, which gives a critical electric field approximately constant with energy. This still allows runaway as long as this critical electric field is exceeded. However, the runaway effect will not be as dramatic as in fully-ionized plasma, since there the drag force falls with energy.

Ionizing collisions between fast electrons and argon are estimated to be a smaller effect. While reported cross-sections are similar to momentum loss (both are approximately 2×10^{-20} m^2 at 100 eV) [69], a momentum-loss collision is more drastic, as one such "collision," which is actually a large collection of small-angle scatterings, removes a large fraction ($1 - \mathrm{e}^{-1} \simeq 63\%$) of a particle's momentum. In contrast, typical ionization events only remove energies in the range of the ionization threshold (15.75 eV) [75].

These critical electric fields, along with normalized drift parameters (ratio of average electron-ion drift to various thermal speeds) are summarized in Table 3.1. The latter are relevant to the types of turbulence which can be produced in the plasma, and will be relevant to discussions in the following chapters.

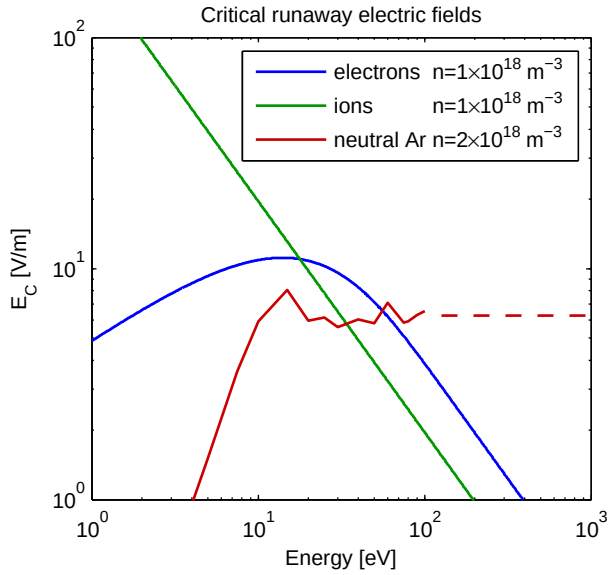

Figure 3-7: Critical "runaway" electric fields calculated as a function of energy, using momentum loss against electrons, ions, and neutral Ar. Neutral Ar momentum-loss cross sections are taken from a recent review [74].

Plasma density	n_e	$\simeq 1 \times 10^{18}$ m^{-3}
Temperature	$k_B T_e$	$\gtrsim 15$ eV $\gg kT_i$
Thermal speeds		
Electron thermal	$v_{te} \equiv (2k_B T_e/m_e)^{1/2}$	2.5×10^6 m/s
Ion sound speed	$c_s \equiv (k_B T_e/m_i)^{1/2}$	6×10^3 m/s
Current density	j_ϕ	60 kA/m^2
Drift speeds	$v_{de} \equiv j/ne$	3.5×10^5 m/s
Drift parameter		
Electrons	v_{de}/v_{te}	0.15
Ions	v_{de}/c_s	60
Electric fields E_ϕ		
Before reconnection		2 V/m
Peak during reconnection		15 V/m
Critical electric fields E_c		
20 eV		25 V/m
100 eV		12 V/m

Table 3.1: Drift parameters and characteristic electric fields during the reconnection events.

In summary, it is found that the typical electric fields during reconnection events approach or exceed the critical field for runaway production. Residual neutral argon gas, if not burned out, is found to have a roughly equal effect to the charged species, and therefore should be taken into account for future study of runaway electron production by reconnection events in VTF.

3.3 Energetic electron production

This section presents observations of the tail of the electron distribution function using electron energy analyzers. First we present initial observations made using a single-collector electron energy analyzer, which shows that a population of fast electrons is created by the reconnection events. We then present further observations using the multi-channel analyzer described in the previous chapter. This confirms heating of the tail electron population during the reconnection events. However, resolving the fine details of the velocity space structure (an initial goal for this probe) is not possible because we find *spatial* structure in the fast electrons on the 1 cm scale of the probe.

As described in the previous chapter, a single-collector electron energy analyzer measures the current of fast electrons with sufficient energy to overcome the discriminator grid bias. If the area of the collector is much larger than the electron gyroradius, it will simply be the parallel component of the electron energy which determines which particles can reach the collector.

$$\begin{aligned} I_{coll}(V_{bias}) &= e\,TA \int_{v_c}^{\infty} v_{||} f(v_{||}) dv_{||}, \\ &= \frac{e\,TA}{m_e} \int_{\mathcal{E}_c}^{\infty} f(\mathcal{E}) d\mathcal{E}, \end{aligned} \tag{3.10}$$

where $\mathcal{E}_c = m_e v_c^2/2 = e(V_{plasma} - V_{bias})$ is the critical energy to reach the probe (which we will call the true bias point) and v_c is the associated critical parallel velocity. Under ideal conditions, one can measure I_{coll} as a function of V_{bias}, and take derivatives (or finite differences) to determine $f(\mathcal{E})$.

Figure 3-8 shows our analysis from a series of discharges using a single-channel energy analyzer. An experimental challenge here is that the true bias point changes (via changes in V_{plasma}) over the course of the discharge. To attempt to control for this, plasma discharges

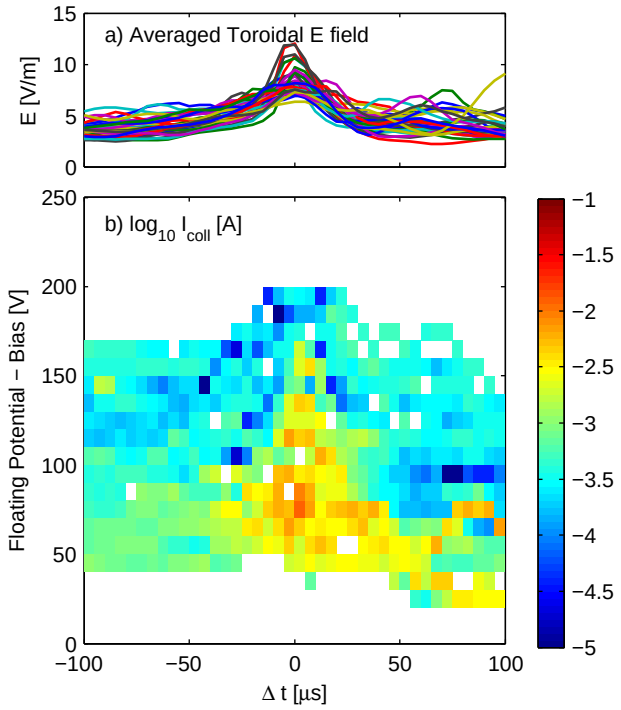

Figure 3-8: Measurements of the raw current of fast electrons versus time during reconnection events. Data was assembled over multiple discharges from a single-channel gridded energy analyzer, as described in the text.

were repeated with various V_{bias}. The reconnection event in each discharge was identified based on the peak electric field, and time Δt is measured in each discharge relative to the reconnection event. Further, V_{float} was measured (using the front, floating grid) as a function of time through the discharge. The difference $V_{bias} - V_{float}$ is assumed to track the true bias $V_{bias} - V_{plasma}$ (though recall that these are expected to differ by approximately $5k_BT_e/e$). Each shot then obtains a measurement of I_{coll} along a trajectory in (Δt, $V_{bias} - V_{float}(t)$) space; these are interpolated onto a grid. Figure 3-8 shows, the results of this analysis, which is the current into the collector as a function of ($V_{float} - V_{bias}$) and time. Notably, electrons with energies of $\geq$ 150 eV beyond the floating potential are observed, which naively implies electrons with energies near 250 eV. Thus far it has proven difficult to look much beyond this point due to decreasing signal to noise out on the tail and arc breakdown (between pairs of grid biased hundreds of volts apart and separated by less than 1 mm.) Further experiments were conducted with the probe looking the opposite direction along the magnetic field (and therefore opposite to the direction that electrons are accelerated by an electric field) and no fast electron current was observed.

Finally, note that Fig. 3-8 presents not $f(\mathcal{E})$, but its integral I_{coll}. As might be expected, differentiating this assembled data set to attempt to derive $f(\mathcal{E})$ was not successful, due to lack of shot-to-shot reproducibility. To attempt to improve upon these measurements, a 7-channel electron energy analyzer was designed and constructed, as discussed in detail in the previous chapter.

These measurements do improve over the single-point measurements, as now the location of the plasma potential is of less concern; the heating or energization is apparent simply from relative changes in currents between channels at different discriminating bias. Initially, it was hoped that a multi-channel analyzer would be able to directly observe unstable features in the electron distribution. However, in the end this level of detail was not attainable, as will be shown below, because the population of fast electrons has spatial variations on the scale of the probe. Naively applying $f(\mathcal{E}) \approx \Delta I_e/\Delta V$ using numerical differences between adjacently-biased channels yields unphysical, negative values for f due to this extra noise.

Instead, we have had more success measuring the average "temperature" of the tail electrons implied by the probe measurements. If the fast electrons are imagined to arise from a (one-sided) maxwellian distribution with effective temperature T_{tail} then $I_{coll}(V) \propto \exp(-V_{bias}/T_{tail})$. Then, a linear fit to $\log I_{coll}$ vs. V_{bias} yields T_{tail} from the slope. This is the procedure adopted here. Notably, this slope measurement is invariant to uncertainty in true bias point, $V_{bias} - V_{plasma}$. Therefore, by this method one robustly measures the effective temperature on the tail of the electron distribution, but exactly where on the tail is uncertain. However, the total bias range used, 100 V, is approximately the same as the true bias point, so the probe is averaging over a large fraction of the tail.

Figure 3-9 shows an example of fast electron production and application of this analysis method. Figure 3-9(a) shows the time trace of the toroidal, reconnection electric field, evaluated at the location of the probe. The reconnection drive was applied at $t = 1200$ μs, after which the current sheet formed, followed by a strong reconnection event at $t = 1360$ μs. Figure 3-9(b) shows the time traces of current to the 7 collectors. The associated biases on the discriminating grid, relative to ground, range from -140 V to -40 V, and are indicated in the legend. The grids with strongest bias will collect only the most energetic electrons. One grid (gray trace, V_{float} in the legend) is connected directly to the "floating" front grid. For this set, the channels with -140, -120, and -100 V biasing did not have a floating grid in front. It has been found that the front floating grid does not have a large effect

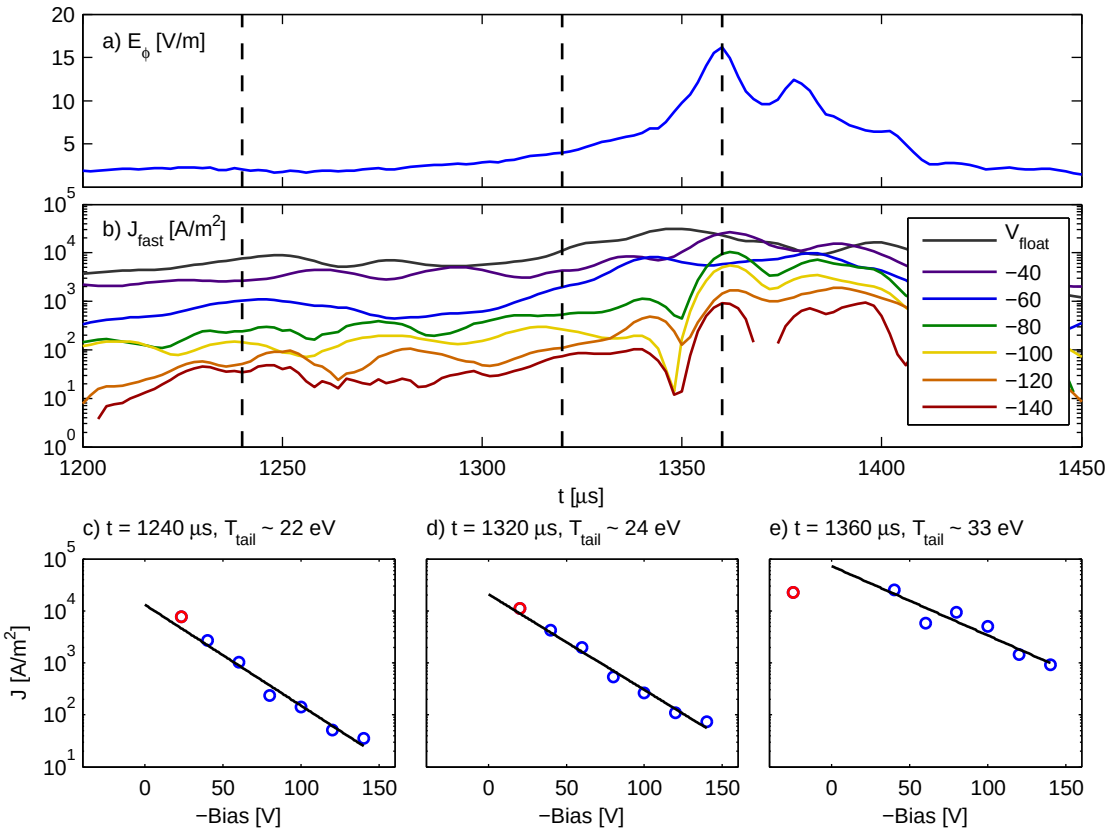

Figure 3-9: Measurement of fast electrons versus time with a seven-channel energy analyzer. (a) Toroidal reconnection electric field evaluated at the probe location. (b) Time traces of fast electron current to the seven collectors. Color indicates grid bias, from −140 V (red, bottom) to −40 V (violet, second-to-top), and floating (gray, top). (The typical floating potential for most of the discharge is near −20 V.) (c-e) Current versus bias at times 1240 (c), 1320 (d), and 1360 (e) μs.

on measured signals, apart from the extra transparency effects. Its presence or absence is accounted for within the cross-calibration coefficients between channels, which range over about $\pm$ 20%, and which are derived from a large scan of discharges biasing all grids equally. Finally, the traces have been normalized by probe area and nominal grid transparency to yield current density.

Notably, the currents to all collectors increase strongly during the reconnection events, with the greatest relative increase among the strongest-biased probes. For instance, the current for the collector behind the -100 V grid increases from $\simeq$ 200 A/m^2 before the reconnection event up to $\simeq$ 5 kA/m^2 at the reconnection event, a relative increase of about 25. Furthermore, the traces appear to "squeeze" together during the reconnection events, indicative of heating.

Figure 3-9(c-e) display the collector currents versus bias at times t = 1240, 1320, and 1360 μs, indicated by vertical dashed lines in Fig. 3-9(a,b). The last time is during the reconnection event. Plotted along with these are linear fits to the data which give characteristic temperatures of the tail electrons. Prior to the reconnection event, the inferred temperature is near 20 eV. However, during the reconnection event, in addition to finding stronger fast electron currents, we also find a flatter slope, with inferred temperature of about 33 eV, about a 60% increase. This is not insignificant; if the temperature of the (whole) distribution increases from 20 to 33 eV, then the current of 200 eV particles will increase a factor of $\exp(200/20 - 200/33) \simeq e^4 \sim 50$.

In Fig. 3-9(c-e), the floating potential is indicated by the red circle, along with current to its associated collector. The floating potential is generally found to move strongly (up to 80 V) during the reconnection events. Interestingly, the floating potential is often found in this discharge to swing positive; this is counter to the direction driven by electron heating alone (recall $V_{float} - V_{plasma} \simeq -5k_BT_e/e$, discussed in the previous chapter). This indicates that there are strong positive swings of V_{plasma} during the reconnection events (at the probe location). This implies that the true bias point $V_{bias} - V_{plasma}$ for the probe could be even *larger* during the reconnection events, therefore energization may be even larger than what is suggested simply from the relative change in electron current at fixed bias.

In terms of fitting temperatures to the data, the grid at floating potential swings far away from the other biases and strongly influences the measured slope if it is used in the fit, in this case leading to a greater inferred temperature. (This is apparent in Fig 3-9(e), where

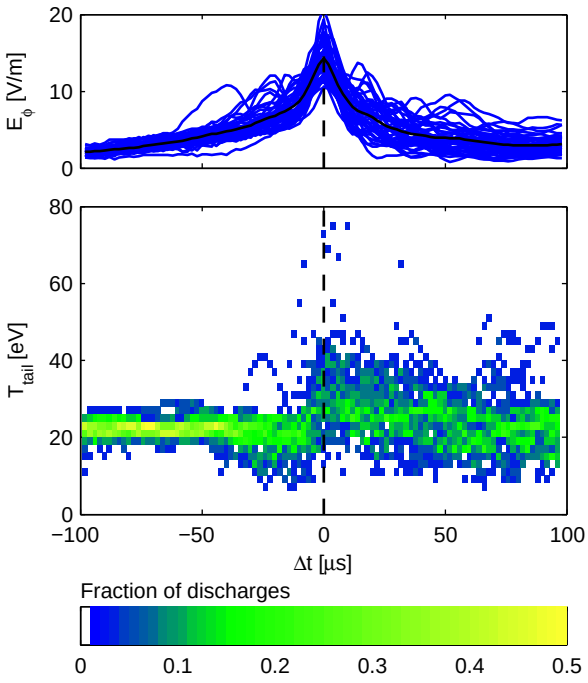

Figure 3-10: Color histogram of fitted electron tail temperatures during reconnection events. Color indicates the fraction of measured temperatures in a given (T_{tail}, t) bin over the collection of discharges.

including the red, floating-biased collector in the fit will lead to a flatter line, indicating a higher temperature.) In the absence of a complete understanding of the dynamics of V_{float}, here we will report the more conservative results based on fitting only to the other collectors.

Figure 3-10 shows temperature measurements over a large collection of discharges. Figure 3-10(a) shows measured reconnection electric fields (evaluated using a flux array 20° toroidally away from the energy analyzer, which is within a few cm of the reconnection x line in the poloidal plane.) Time is measured relative to the reconnection event, which is identified as the time of peak toroidal electric field. For each discharge, the tail temperature is measured by fitting as discussed above. Results are shown in color histogram form in Fig. 3-10(b), in which color indicates the fraction of discharges which landed in a given time-temperature bin. The results robustly show heating of the tail of electrons from near 20 eV before reconnection events to a typical 30–35 eV immediately after.

Finally, we present some data on fine-scale structure or "filamentation" of the fast electron population. This is inferred from scans with all seven grids biased with the same

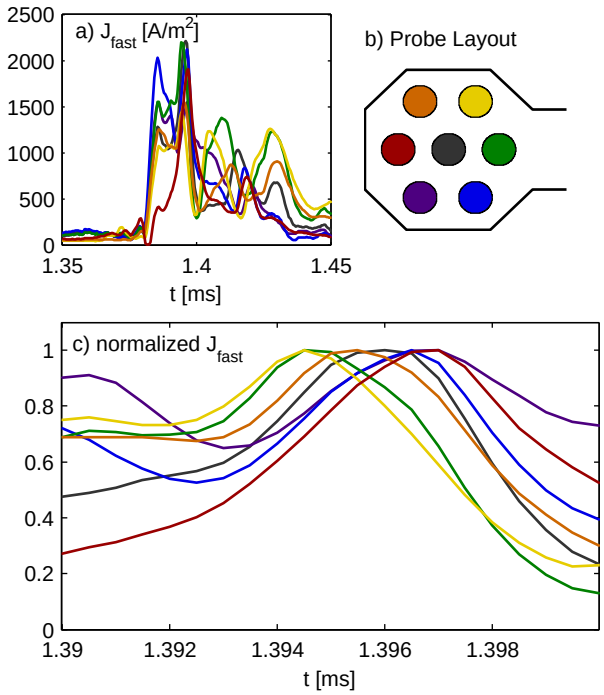

Figure 3-11: Evidence for filamented "beamlets" in the fast electron population. a) Collector currents versus time near a reconnection event. Color indicates collector location as shown in (b). c)Traces near 1.39 ms, with collector currents normalized to their respective maxima, showing propagation of a filament across the probe face.

retarding voltage. Even with equal biases, it is found that the collectors measure highly differing time traces. Figure 3-11 shows a particularly clear example of this phenomenon. Figure 3-11(a) shows the time traces of all 7 collectors, showing a burst of fast electrons onto the collectors as a result of a reconnection event. Data to these collectors has been normalized by probe areas and nominal grid transparency to yield fast electron current densities. For this discharge, the grids are biased at -120 V with respect to ground. Figure 3-11(b) shows the color coding of collector channels used in the plotting.

As can be seen in Fig. 3-11(a), a few "waves" of fast electrons wash over the probe, but they are not measured on all channels equally. Moreover, there are clear correlations between *adjacent* collectors. For example, near 1.39 ms, the green, blue, and violet channels pick up the largest currents, indicating localization on the bottom quadrant of the probe. Similarly, near 1.44 ms, the green, yellow, and orange channels are strongest, indicating that the electrons predominantly crossed the top half of the probe. Finally, Fig 3-11(c) zooms in on the 10 μs region from 1.39 to 1.40 ms, and normalizes each collector by its peak

current for clarity in comparing the time-behavior. Here, the fast electron current crossed all the probe faces, and roughly in order from right to left, reaching maximum on the yellow and green collectors first, followed by orange, gray, and blue, and finishing with red and violet. From the time traces one can also see that by the time that the current is maximum over red and violet, it is down by about 50% on yellow and green, and vice versa. This indicates that the characteristic size of these current filaments was approximately the probe size (1 cm). (A similar conclusion can be reached from the amplitude-variation between adjacent channels on the probe, which are separated by about 0.4 cm.) At the same time, the current filament can be seen to propagate roughly 1 cm in 3 μs, or at about 3×10^3 m/s; this is of the same order as the characteristic speed of the reconnection outflow.

Filamentation of the fast electron population is interesting in its own right and should be investigated further in future research. It also implies extra instability mechanisms (strong spatial gradients), which will be discussed further in the next chapter. To improve energy analyzer design, however, and get past the simple exponential fitting which we have used above, future energy analyzers must be designed so that all collectors see the same fast electrons. The basic inhomogeneity scale appears to be about 0.5 cm, so future energy analyzers must be constructed at this scale or smaller, or roughly a factor of 3 smaller than the present probe; one might hope to fit all collectors in the area of a *single* collector on the present design. It is very difficult to envision simply scaling the present design down because of the difficulty of soldering the mesh to a smaller structure. However, it may be possible to put all the collectors behind a single pair of grids, using the first grid to screen bulk electrons, the second to screen ions, and then variably bias the multiple collectors to discriminate electron energies.

In conclusion, these results are best understood as useful and semi-quantitative but not perfect diagnostics of the production of super-thermal electrons. The results are robust due to the use of multiple grids, which measure an increase in the temperature of the electron tail, independent of knowledge of the plasma potential (and hence bias point). Future, smaller energy analyzers are envisioned which occupy a region smaller than the observed inhomogeneity scale of the fast electrons.

Chapter 4

Study of Electrostatic Fluctuations

This chapter presents observations of broadband, electrostatic plasma fluctuations that arise during reconnection events. The previous chapter discussed basic results on reconnection from the VTF experiment. A chief finding was that the reconnection process is "spontaneous," consisting of periods of slow reconnection and current sheet formation punctuated by bursts of fast reconnection, dissipating the energy in the current sheet over a short period of time. Thus, the experimental reconnection rate changes drastically over time, as does an inferred resistivity E_ϕ/j_ϕ. This observed strong time-variation is an interesting problem in its own right, and may point the way to the larger "trigger" problem of the onset of fast reconnection in other systems. For our purposes here, observing the time-correlation of various processes with the reconnection events becomes an extra tool to use in discerning which mechanisms play an important role in reconnection in VTF.

With this in mind, a detailed study of plasma fluctuations during reconnection events in VTF has been undertaken. Experiments have found that substantial fluctuations appear during the reconnection events. Modes are identified based on frequency and wavelengths, which are measured using multi-probe cross-correlation techniques. Identifying the modes and the possible excitation mechanisms is an important aspect of determining whether the modes can have an important role in the reconnection events or are simply a consequence of reconnection. We also make some preliminary estimates of electron-ion coupling via quasi-linear theory.

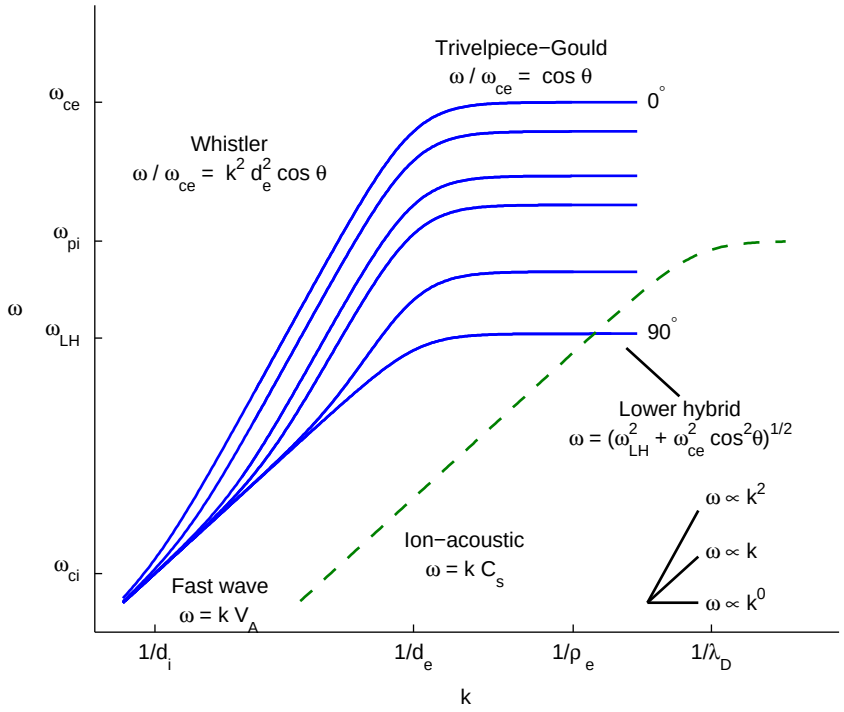

Figure 4-1: Landscape of linear modes calculated for VTF parameters. Dispersion relations ω vs. k, in log-log-scale, are plotted for a few angles $\theta = \angle(\mathbf{k}, \mathbf{B})$. Blue curve: right-handed branch of cold plasma dispersion, which includes fast waves, whistler waves, Trivelpiece-Gould waves, and lower-hybrid waves. Green dashed curve: ion-acoustic waves. The triangular legend (lower-right) indicates 3 characteristic slopes on the log-log scale, corresponding to dispersion curves $\omega \propto k^0, k^1$, and k^2.

4.1 Background

Figure 4-1 plots the linear dispersion relation of standard, fluid waves [76] for VTF parameters and serves to fix the terminology used here. VTF is in the wave regime $\omega_{pe}^2 \gg \omega_{ce}^2$, and therefore there is a large gap with no cold-fluid modes between ω_{ce} and ω_{pe}. Modes near ω_{pe} have not been studied here and therefore modes with $\omega \leq \omega_{ce}$ are considered. Similarly, at the low-frequency end only modes with $\omega > \omega_{ci}$ are considered, as those are the only modes which can be driven on the time scale of the reconnection events in VTF ($\sim 1/\omega_{ci}$).

For reference, the definitions and typical experimental values of a number of fundamental frequencies (e.g. plasmas frequency ω_{pe}, etc) and length scales (e.g. the ion inertial length d_i, electron gyroradius ρ_e, etc.) were given in Table 2.1 (page 38).

Two basic dispersion branches exist. First, the cold R-waves [76], which derive from the right-handed branch of the cold plasma dispersion tensor, are plotted in blue, for a

few angles $\theta = \angle(\mathbf{k}, \mathbf{B})$. Starting at long wavelength ($kd_i \sim 1$, where d_i is the ion inertial length) and low-frequency ($\omega \sim \omega_{ci}$), these are the MHD "fast" (compressional Alfvén) waves, with dispersion relation $\omega = kV_A$, where V_A is the Alfvén speed. Following the dispersion curve, as k is increased past $1/d_i$, the ions become unmagnetized, and the waves become the electromagnetic "whistler" waves, with quadratic dispersion $\omega = \omega_{ci}k^2d_i^2\cos\theta = \omega_{ce}k^2d_e^2\cos\theta$. Here $d_e = c/\omega_{pe}$ is the electron inertial length. Both the fast waves and whistler waves are electromagnetic, with $\mathbf{E} \perp \mathbf{k}$, and $\mathbf{E}$ is found to rotate around $\mathbf{B}$ in the right-handed sense. As k is further increased past $1/d_e$, the modes become the electrostatic "Trivelpiece-Gould" waves with the dispersion relation $\omega \simeq \omega_{ce}\cos\theta$. If one follows the Trivelpiece-Gould branch to extreme perpendicular angles, ion dynamics must be included again, and one finds the "lower-hybrid" waves, with $\omega \simeq (\omega_{LH}^2 + \omega_{ce}^2\cos^2\theta)^{1/2}$. Here, $\omega_{LH} = (\omega_{ce}\omega_{ci})^{1/2}$ is the lower-hybrid frequency. Finally, the Trivelpiece-Gould modes begin to become damped (on electrons, as $\omega/k_{||} \sim v_{te}$) when $k\rho_e \sim 1$, where ρ_e is the electron gyroradius.

A second branch of possible waves is the ion-acoustic waves, which derive from a hot, isothermal electron response and cold ion response. They have the dispersion relation $\omega \simeq kc_s$ and exist for $\omega \leq \omega_{pi}$, which is reached when $k\lambda_D \sim 1$. Here c_s is the ion sound speed and λ_D the Debye length. The ion acoustic waves can be driven unstable by relative electron-ion drift, but only if T_e is sufficiently larger than T_i so that the waves are not strongly damped on the ions.

4.2 Observation of fluctuations during reconnection

Two primary types of fluctuations have been observed on VTF during reconnection events: lower-hybrid waves and high-frequency Trivelpiece-Gould waves. The former are the strongest component the fluctuations, and have peak fluctuation power near $f_{LH} \simeq 10$ MHz. The Trivelpiece-Gould waves on the other hand comprise the high-frequency band of the spectrum and typically have peak power near 1 GHz ($\sim f_{ce}/2$).

Figure 4-2 shows a sequence of plots from our studies of the relationship of reconnection events and development of fast plasma fluctuations. This particular discharge was selected because it contains a clear picture of phenomena that will be discussed in detail below.

Figure 4-2(a) shows plasma current density, and (b) shows electric field, evaluated at

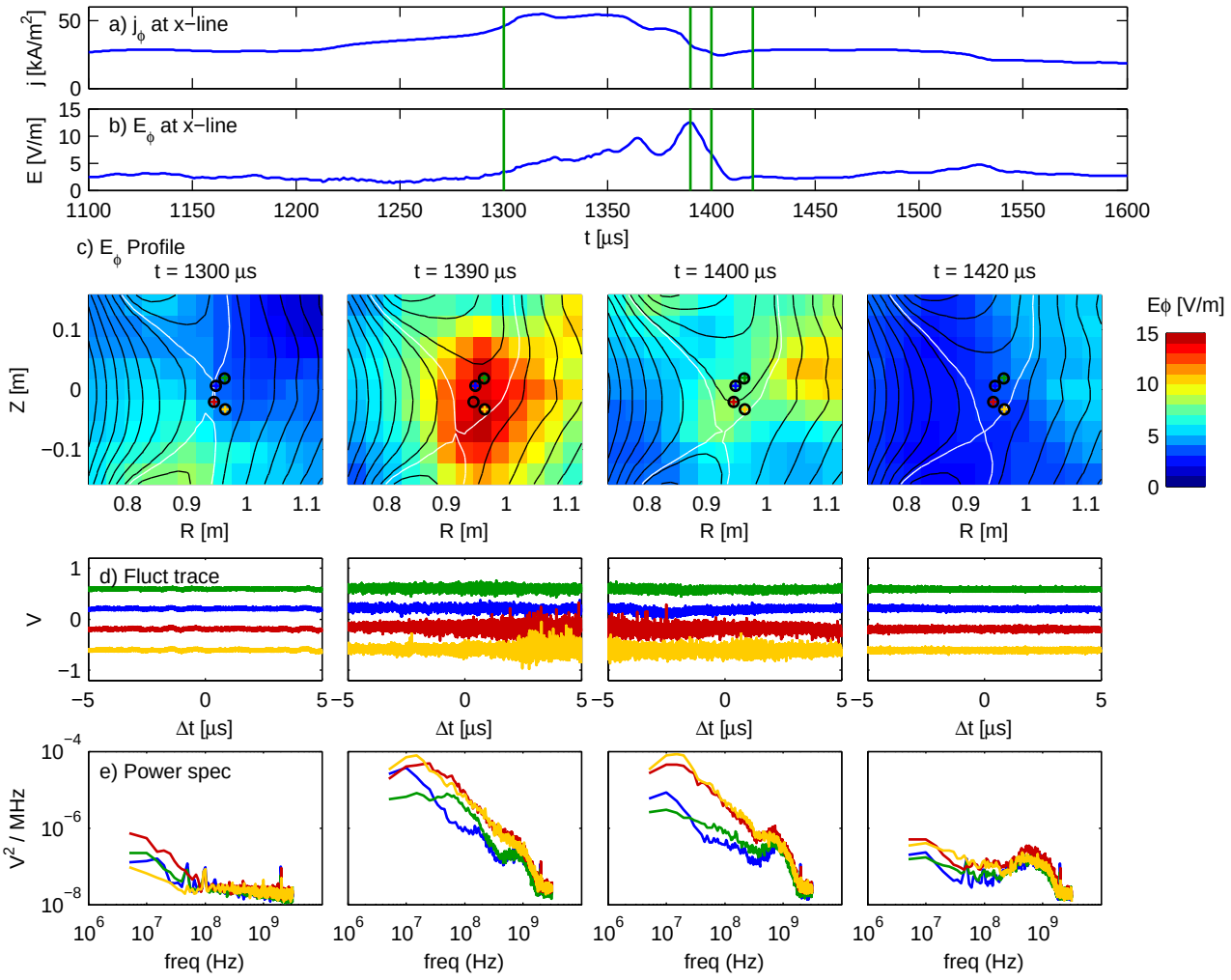

Figure 4-2: Global picture of reconnection events and high-frequency plasma turbulence. (a) Plasma current density evaluated at the x line. (b) Reconnection electric field (reconnection rate) evaluated at the x line. (c) Magnetic flux surfaces (black), magnetic separatrix (white), and color background indicating toroidal electric field. (d) Fluctuation traces (e) Power spectra from traces. Signals are color-coded (green, blue, red, yellow) corresponding to the location of the probe in the experiment cross-section, shown by colored symbols in (c).

the reconnection x line. The plasma discharge was initiated at $t = 0$, and density built up through 1.2 ms of ohmic heating. At $t = 1200$ μs, the reconnection drive was applied, pulling the plasma into a current sheet, whereupon the current density at the x line increased from 25 kA/m^2 to about 50 kA/m^2. The disruption of this current density is associated with a reconnection event, which in this discharge occurs at $t = 1390$ μs. The reconnection (toroidal) electric field associated with the current crash reached 12 V/m.

The four panes of Fig. 4-2(c) show the contours of magnetic flux (lines) and profile of toroidal electric field (colors) at four times indicated by green vertical lines in Fig. 4-2(a) and (b). Black lines track constant flux surfaces, whereas the white contour denotes the magnetic separatrix. The chosen times illustrate characteristic times during the discharge: current sheet formation, reconnection, and post-reconnection.

Finally, associated fluctuation observations are shown in Fig. 4-2(d) and (e). Figure 4-2(d) shows the time signals observed on four electrostatic probes for the 10 μs window centered on the time indicated in the associated flux frame. Signals are color-coded green, blue, red, and yellow, corresponding to the probes in the experiment cross-section shown as the colored symbols in Figure 4-2(c). (They are in the "fan" configuration from Fig. 2-10.) Fig. 4-2(e) then shows the power spectra, found from standard spectral estimation techniques, for these 10 μs time windows.

The essential observations are as follows: away from the reconnection events, for instance at $t = 1300$ μs, fluctuations are small, close to the bit-noise level. (Some rumbling visible near $f = 1$ MHz is due to noise from the reconnection drive firing circuits; it is actually visible on the magnetics diagnostics as well.) During the reconnection event at $t = 1390$ and 1400 μs, strong fluctuations arise. The fluctuations are flat out to, or have a peak near 10 MHz, which is approximately the lower hybrid frequency. Above this frequency, the fluctuations maintain a broadband character, with power extending all the way to the electron cyclotron frequency. In addition, the fluctuations show strong spatial variation, with the red and yellow probes picking up much stronger fluctuations than the green and blue; this may be because they are closer to the x line. Continuing on, at frequencies near 800 MHz, generally a new peak appears (visible on blue and green at $t = 1390$ μs and on all four at $t = 1400$ μs). In this high-frequency range all probes typically measure similar power. This new peak at 800 MHz is notable because it persists long after the reconnection event—it is still visible on the power spectrum at $t = 1420$ μs. Note that at this time

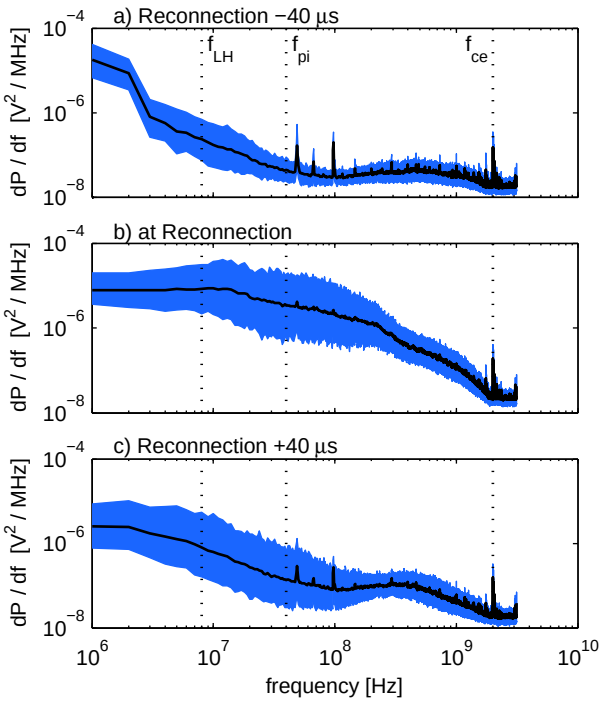

Figure 4-3: Power spectra dP/df observed before, during, and after reconnection events. Black curves indicate geometric mean power over the ensemble of discharges. The colored band encompasses the central 67% of spectra, over all four probes and all discharges. Units are spectral density (Volt^2/MHz) of raw voltages measured by the probe.

the low-frequency modes have mostly disappeared, and the reconnection event has ended. Such high-frequency modes are also observed away from the main reconnection event, for instance, during other types of relaxations of the plasma current during the initial ohmic heating phase of the experiment.

Figure 4-3 shows the evolution of a statistical collection of spectra from 25 discharges and all four probes (in the same fan configuration), at three times relative to the reconnection event. The black curve indicates the geometric mean of the spectra, and the colored band denotes the 1-σ group, so that 2/3 of the measured spectra lie within this band; this gives a measure of the shot-to-shot and probe-to-probe variations in observed fluctuation power, which are substantial, more than 1 order of magnitude in the 10–100 MHz frequency range. The location of the lower-hybrid frequency ($f_{LH} \equiv (f_{ce} f_{ci})^{1/2}$), ion plasma frequency $f_{pi} = 1/2\pi \times (ne^2/\epsilon_0 m_i)^{1/2}$, and electron cyclotron frequency f_{ce} are indicated in the figure as well. The electron plasma frequency $f_{pe} = 1/2\pi \times (ne^2/\epsilon_0 m_e)^{1/2} \geq 10$ GHz is at or off the end of the abscissa.

These curves illustrate that the fluctuation phenomena discussed above are generic: before reconnection events, fluctuations are near the noise level, and strong fluctuations in the lower-hybrid regime, extending out to f_{ce} are driven during the reconnection events. After the reconnection events, a band of high-frequency modes at 1/4 to 1/2 f_{ce} persists.

To assemble this data set, reconnection events are identified by the magnetics diagnostic as the time of maximum reconnection (toroidal) electric field; discharges are only included if the peak reconnection electric field is at least 10 V/m. (This excludes about 1/3 of the discharges.) The reconnection electric field is measured at a magnetic flux array relatively close to the fluctuation probes (approximately 20° away toroidally). Spectra are calculated using standard spectral estimation techniques [77, 78] for the 10 μs window bracketing the reconnection event. This is partitioned into 10 segments, which are separately FFT'd, and the results are averaged to reduce statistical variance in the periodogram estimate. The individual segments are windowed using a Bartlett window before FFT. The data was decimated by 2 from the initial 12.5 GS/s sample frequency to decrease processing requirements for this ensemble; however signals from 3.125 GS to 6.25 GS are observed to be at the noise floor.

To summarize, two distinct species of fluctuations are observed during the reconnection events, a collection of lower frequency modes peaking near the lower hybrid frequency, and a high frequency band peaking from 500–1000 MHz, ($\sim f_{ce}/2$). These modes can be distinguished by their time behavior and space behavior. In particular, the low-frequency modes are more tightly coupled to the reconnection events in space and time, while the high-frequency modes are more uniform in space and persist for 10's of μs after the completion of the reconnection events. We will show that these two groups can also be distinguished by wavelength and dispersion relation. In the coming sections we will show that the low frequency modes are lower-hybrid modes driven by cross-field current, possibly driven by strong gradients, that form during the reconnection events, and the high-frequency modes are electrostatic Trivelpiece-Gould modes driven by high energy (runaway) electrons energized by the reconnection process.

We will now present a more detailed analysis of these two wave regimes.

4.3 Lower-hybrid regime

4.3.1 Measurements

We have conducted more detailed investigations of the waves using cross-correlation techniques between probes separated by 0.3 cm, 1 cm, and 1.3 cm, as shown in Fig. 2-10. The probes are sampled simultaneously by the oscilloscope and correlation analysis is applied off-line. The probe shaft can rotate so that these collinear RF probes can study the cross-correlation properties of modes as a function of angle with respect to the magnetic field. (In the machine geometry, the probe rotates in the Z-ϕ plane.) Recall that the magnetic field is almost entirely toroidal, especially near the reconnection x point where the poloidal component is zero.

Of primary use here is the cross-spectrum C_{XY} [77], which is the Fourier transform of the cross-correlation of signals $x(t), y(t)$, defined as $c_{xy}(\tau) \equiv \frac{1}{T}\int_0^T x(t)y(\tau - t)dt$, where T is an averaging time, long enough for sufficient statistics and frequency resolution, but short enough so that fluctuation power is approximately stationary. Experimentally this is evaluated from the Fourier transforms $X(f)$ and $Y(f)$ of the signals as

$$C_{XY}(f) \equiv \langle X^\dagger(f)Y(f)\rangle. \tag{4.1}$$

Here $\dagger$ denotes complex conjugation. C_{XY} is complex, and therefore contains both amplitude and phase information. The amplitude is typically normalized by the power spectra of the individual signals to provide a dimensionless quantity known as coherency, which intuitively is the correlation coefficient between the two signals as a function of frequency.

An equally important measure is the cross-phase, defined as $\arg(C_{XY})$. If the signals are well-correlated, this can supply the average phase relationship between the two signals at each frequency; this is interpreted as $\mathbf{k} \cdot \mathbf{\Delta}$, where $\mathbf{k}$ is the wave-vector and $\mathbf{\Delta}$ is the vector separation between probe tips. As the signals become uncorrelated, the cross phase becomes random and uniformly distributed on the interval $(-\pi, \pi)$. (Here we will uniformly use $-\pi$ as the branch cut for arg.)

These measurement techniques succeed when two probes observe the same wave-packet and signals are strong compared to noise. Coherency drops and the phase becomes random when this condition is not fulfilled. Most importantly, if multiple waves exist at the same

frequency but have different vector $\mathbf{k}$, then they will register different phase shifts between the probe tips. This "wave-bath" effect can quickly destroy coherence. Spectral resolution can also play a role: the requirement to look over a finite time window sets a minimum frequency resolution $\delta\omega$, and if wave dispersion is large enough so that $\Delta \cdot d\mathbf{k}/d\omega \times \delta\omega \sim 1$, then the coherency will be low because many waves with different probe-probe phase will land within one frequency bin.

Furthermore, since we will typically look at phase data for multiple discharges, it is further required that $\mathbf{k}$ is reproducible between discharges. Finally, all of these spectral estimators have intrinsic variance, and therefore, like the power spectrum estimates, one partitions the measurement window, and estimates $\overline{C_{XY}}$ from an average of cross-correlations of each segment. Notably, the final cross-phase is not an average of the phases, but rather the phase of the (complex) averaged $\overline{C_{XY}}$.

Figure 4-4 shows a color histogram of the observed cross-phase for frequencies in the "lower-hybrid" regime of 0–200 MHz, for probes at 0.3 cm, 1 cm, and 1.3 cm separation, with the probe aligned with the magnetic field. An ensemble of 15 discharges is used. In each, phase is extracted from the cross-correlation evaluated over the 10 μs window centered on the reconnection event, averaging 50 segments, for 5 MHz spectral resolution. Data is binned into 40 bins distributed between $-\pi$ and π; color indicates the fraction of phase measurements landing in a particular bin.

First, note that the phase measurements are most consistent at small separation, and become more scattered at larger separation, indicating that the coherence is falling off with a parallel scale of order 1 cm. The most important conclusion is that the phase in this regime does not rapidly wind through 2π, but rather stays close enough to zero to indicate that $k_{||} \lesssim 300$ m^{-1} over this range. Equivalently, one can bound the parallel phase speed $d\omega/dk_{||} \sim \omega/k_{||} \gtrsim 2 \times 10^6$ m/s, which is of order or larger than the electron thermal speed. Despite the crudeness of this estimate, it is sufficient to conclude that these waves cannot be parallel acoustic waves driven by electron current. These would have $\omega/k_{||} \sim c_s \ll v_{te}$, and would have registered a substantially faster winding of the phase (leading most likely to a random phase measurement) than is observed. Next, a noisy, but finite preference for negative $\omega/k_{||}$ is apparent; this is consistent with modes traveling in the direction of electron drift (i.e. the parallel electron drift comprising the toroidal plasma current).

Figure 4-5 shows a similar color histogram, except here we have varied the angle θ of

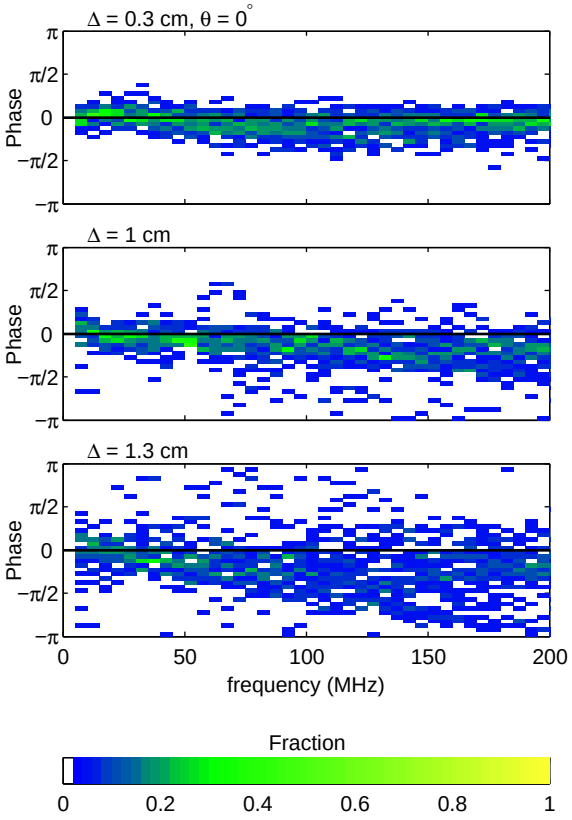

Figure 4-4: Phase measurements versus probe separation for the lower-hybrid frequency regime $0 < f < 200$ MHz. The plot is shown in color histogram form, showing fraction of discharges which measured a given phase at given frequency.

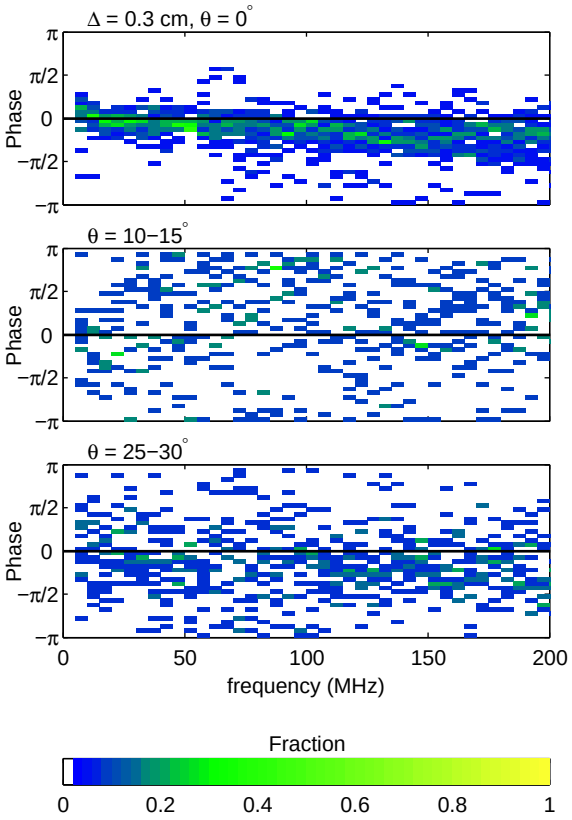

Figure 4-5: Phase measurements versus angle of the probe with respect to the magnetic field for probe separation = 0.3 cm, over the lower-hybrid frequency regime $0 < f < 200\ MHz$. The plot is shown in color histogram form, showing fraction of discharges which measured a given phase at given frequency.

the probe with respect to the magnetic field for the 0.3 cm probe separation. The phase quickly becomes random with angle, becoming nearly completely incoherent and random by $\theta = 30^\circ$ for $f < 100$ MHz, or $\theta = 15^\circ$ for $f < 50$ MHz. At the same time, the fluctuations are strong here, much larger than the bit noise, so the incoherence arises directly from the presence of a bath of waves with different $\mathbf{k} \cdot \mathbf{\Delta}$ at each frequency. We have already found that $k_{||}\Delta_{||}$ is small, indicating that it is $\delta(\mathbf{k}_\perp \cdot \mathbf{\Delta}_\perp) > \pi$ that gives the spread. This sets a minimum bound in typical $k_\perp$, since $\delta(\mathbf{k}_\perp \cdot \mathbf{\Delta}_\perp) < k_\perp \Delta_\perp$, implying $k_\perp \gtrsim 4000$ m^{-1} at $f = 100$ MHz. In plasma units, $k_\perp \rho_e \simeq 0.8$ using $k_\perp \simeq 4000$ m^{-1}. Other potential mechanisms for this decorrelation are that the two probes are not observing the same wave packet, or that instability growth is large enough so that a new wave has grown from noise in between the two probes. However, both these ideas lead to the same conclusion about the largeness of $k_\perp$: in the first case, a large $k_\perp$ is necessary to construct a sufficiently narrow wave packet. In the second case, we would conclude the yet-stronger condition $k_i \Delta_\perp \gtrsim 1$ where k_i is the imaginary part of the wave vector ($= \gamma / v_{gr}$).

In conclusion, we find that $k_\perp \gg k_{||}$ for waves in this regime, and quickly find poor coherence between probes as they are separated by a small distance ($\sim$1 mm) perpendicular to the field, even as they are coherent over longer distances ($\sim$1 cm) parallel to the field.

Finally, Fig. 4-6 shows the time correlation of these lower-hybrid modes and the reconnection events, evaluated for a large ensemble of discharges, with the probes in the fan configuration as used above. An important observation here is that while there is good overall correlation of the reconnection events with fluctuation observations, there appears to be a systematic delay of the fluctuations with respect to the peak reconnection electric field.

4.3.2 Discussion

As discussed, our observations are not consistent with ion-acoustic waves, since $k_{||}$ is observed to be too small. It is not automatically clear why ion-acoustic instability has not been observed. Based on observed current densities near 50 kA/m^2 and density of 1×10^{18} m^{-3}, we find electron-ion drifts, $v_{de} = j/ne \simeq 50 c_s$. This is large enough to trigger the ion-acoustic instability (for argon/electron mass ratio) as long as $T_e/T_i > 5$ [79]. The critical electron drift to trigger the ion-acoustic instability is a strong function of the electron-ion temperature ratio, however: at $T_e/T_i = 10$ the critical drift is only $\simeq 15 c_s$. At present the

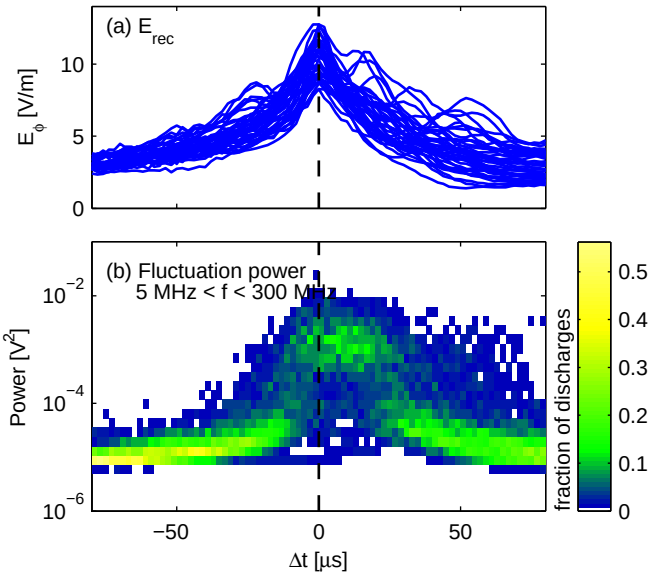

Figure 4-6: Color histogram indicating time-correlation of reconnection electric fields and high-frequency fluctuation observations in the Lower-hybrid regime, 5 MHz $< f <$ 200 MHz. Color indicates fraction of discharges which measured a given power in this frequency band versus time relative to the peak of the reconnection event.

ion temperature is not known experimentally, though ion temperature measurements on the "open" configuration of VTF (using laser-induced fluorescence) found ion temperatures up to 2 eV during reconnection [51].

Instead, the results better match expectations for lower-hybrid waves, electrostatic waves which satisfy the dispersion relation,

$$\begin{aligned} \omega^2 &= \frac{\omega_{pi}^2 + \omega_{pe}^2 \cos^2\theta}{1 + \omega_{pe}^2/\omega_{ce}^2}, \\ &\simeq \omega_{LH}^2 + \omega_{ce}^2 \cos^2\theta, \end{aligned} \tag{4.2}$$

where $\omega_{LH}^2 = \omega_{pi}^2/(1 + \omega_{pe}^2/\omega_{ce}^2) \approx \omega_{ce}\omega_{ci}$, as VTF is in the regime $\omega_{pe}^2 \gg \omega_{ce}^2$. (The dispersion relation and propagation characteristics of lower-hybrid waves have been thoroughly investigated in laboratory plasmas, e.g. in Ref. [80].) Near the lower hybrid frequency, these modes are quite anisotropic with $k_{||} \ll k_\perp$, in agreement with observations here. Finally, lower-hybrid waves derive from cold electron response, in accordance with the observed bound $\omega/k_{||} > v_{te}$. Overall, the measurement of $k_{||}$ is quite noisy, but this may be expected due to projection effects from slight misalignment of the probe with the magnetic field: near

ω_{LH}, $k_{||}/k_{\perp} \simeq 1/270$ for argon.

Observations here do not decisively measure $k_{\perp}$, but its effect is manifested in the decorrelation of the probe signals as the probe is barely rotated away from being parallel to the magnetic field. As discussed, it is not even necessarily possible to directly observe $k_{\perp}$ unless there is a single well-defined vector $\mathbf{k}_{\perp}$ with which the probes are aligned.

Lower-hybrid waves have played a prominent role in theories of anomalous plasma resistivity, including early theories applied to collisionless shocks in laboratory plasmas, and later applied to reconnection. They are also of interest for their mediation of interactions between electrons and ions: they can simultaneously interact with electron parallel energy via $\omega_{LH}/k_{||} \sim v_{te}$ and ion perpendicular energy via $\omega_{LH}/k_{\perp} \sim v_{ti}$ [81, 82]. A number of mechanisms have been proposed in the literature to account for excitation of lower-hybrid waves, roughly grouped into "parallel" or "perpendicular" excitation mechanisms, which we now discuss in turn. Our results favor the perpendicular drive mechanisms from gradients in the plasma, and we will discuss these in detail first. Afterwards some brief comments will be made about the parallel excitation mechanisms.

4.3.3 Lower-hybrid waves: Perpendicular excitation

Overall, the lower-hybrid region is fertile ground for plasma instabilities. In reconnecting current sheets, the length scales can be on the order of the ion or "sound" gyroradii (ρ_i or ρ_s). (These are much steeper gradients than typically contemplated in instability studies, where the instability scale lengths are typically the minor radius a.) With such strong gradients, the "drift-frequency" $\omega_* \equiv k_y T/eBL_n$ (which is just the wave vector $\mathbf{k}$ dotted into the diamagnetic drift velocity) can approach the lower-hybrid frequency when $k_y\rho_e \to 1$ and $L_n \to \rho_s$. Interaction of the drift and lower hybrid modes leads to a strong instability. These types of instabilities have previously been studied in basic laboratory plasmas, e.g. in Ref. [83].

These instabilities and their role in reconnection have been extensively studied since their early identification as a method of producing anomalous resistivity [32]. Experiments on the MRX device by Carter *et al* [41] observed the "lower-hybrid drift instability" (LHDI) [31], which is the version driven unstable by a strong density gradient. (The MRX current sheet is about 1 ρ_i wide, exactly the regime to drive this sort of instability.) This work concluded, however, that the observed LHDI did not correlate well with enhanced reconnection. They

also found that the LHDI was confined to the low-β half of their current sheet (which is in-out asymmetric due to toroidal effects). This agreed with the theoretical predictions that the electrostatic LHDI modes are stabilized by finite plasma beta [84]. The LHDI has now also been observed in the magnetosphere current sheets [85]; that work found the same finite-β effect and similarly found that LHDI could not explain the enhanced reconnection.

However, both of those observations were in an anti-parallel reconnection geometry with $\beta \sim 1$. Experiments reported here, on the other hand, are in a low-beta regime due to the strong guide magnetic field, and so this stabilization mechanism is absent. Further, VTF also has a current sheet that is on the order of ρ_s wide, and therefore in principle the same gradient mechanism can act in VTF as in MRX. However, a more thorough consideration finds some other instability mechanisms that may be more important than the density-gradient-driven LHDI.

First, it is possible that "non-equilibrium" perpendicular currents arise during reconnection due to the strong electric fields associated with the reconnection events. Such currents can arise if, for example, a strong $E \times B$ drift arises on a time scale faster than the ion gyroperiod, so that electrons start drifting before the ions. Such conditions seem marginally possible and will be discussed in more detail below. These "non-equilibrium" perpendicular drifts give rise to the "modified two-stream instability" (MTSI) [31, 81]. It was given its name because the dispersion relation in the fluid limit closely resembles the parallel two-stream (Buneman) instability, with the difference that cross-field drift rather than parallel drift drives the instability. Because the electrons have a magnetized parallel response, the minimum relative (perpendicular) drift speed for strong two-stream-like mode excitation is only the sound speed c_s, unlike the parallel Buneman which requires the much stronger v_{te}.

However, a favored candidate at present is a *temperature*-gradient driven lower-hybrid mode [86]. (This has no accepted moniker, but we will call it LHTI—lower-hybrid temperature (gradient) instability—for short here.) Recall in Chapter 3 that the fast electron population was found to be filamented on a fairly short length scale (about 1 cm), which may imply strong temperature gradients. (There is also a weaker, "kinetic" version of this instability, which is driven by a spatial gradient of fast electrons. Which of these prevails depends on how deeply the observed energization extends into the bulk of the distribution.)

We now present the theory of these instability mechanisms in more detail and calculate stability boundaries and growth rates. All these modes derive from solutions to a com-

mon set of plasma dispersion relations: the warm, electrostatic plasma dispersion relation including gradient effects. This is written schematically as

$$0 = 1 + \epsilon^{(e)} + \epsilon^{(i)}, \tag{4.3}$$

where $\epsilon^{(e)}$ and $\epsilon^{(i)}$ are the electron and ion contributions to the dielectric. The ions are treated as unmagnetized because the growth rates are larger than the ion gyrofrequency and $k\rho_i \gg 1$, so straight-line orbits are used. The electrons are treated by full-orbit integrals, allowing $k\rho_e \sim 1$, with gradients included by the "local" or slab approximation, where it is assumed that wave vectors are much larger than gradient scale lengths. This treatment follows the thorough exposition in the monograph by Mikhailovskii [86]. Detailed calculations are also available in e.g. Ref. [41].

In terms of geometry, the gradients are assumed to lie in the $\hat{x}$-direction, and the drifts (including diamagnetic drifts) are in the $\hat{y}$ direction. The magnetic field is in the $\hat{z}$-direction. Modes resonant with drifting species therefore have finite k_y. Because growth rates maximize when $k_y \simeq k_\perp$, the two will be used largely interchangeably in this discussion. In practice, a finite k_x will be required so that the wave packet can be localized within the gradient regions. However, theory typically finds that $k_y \sim 1/\rho_e$ at maximum growth, much larger than the k_x required by this wave packet criterion, as typical gradient scales are near ρ_s in these theories, so this is not a real concern. For the theory here, k will be taken as positive, and therefore ω is signed, with negative ω indicating a mode propagating in the negative direction. The density and temperature gradients are assumed to be positive (i.e. $dT/dx > 0$, and therefore scale lengths are also positive quantities), and the magnetic field points in the positive $\hat{z}$-direction. Therefore, the ion diamagnetic drift is the in the positive $\hat{y}$–direction and the the electron diamagnetic drift is in the *negative* $\hat{y}$-direction. (The diamagnetic drifts of each species are those that comprise the plasma current to fulfill $\mathbf{j} \times \mathbf{B} = \nabla p$.)

In general, the ion dielectric can be calculated with drifting or stationary ions, and the electron dielectric can be calculated including density, temperature, or no gradients. These are summarized below, but first we discuss how they are mixed and matched to yield the dispersion relation for each instability. This is summarized in Table 4.1.

LHDI [31, 41] is driven by equilibrium density gradient, and it is most easily calculated

Instability	Ions	Electrons	Notes
LHDI	Drifting: Eq. 4.5	Density gradient: Eq. 4.9	$V_{\perp i} = -\frac{T_i}{T_e} V_{\perp e} = \frac{+T_i}{eBL_n}$
MTSI	Drifting: Eq. 4.5	No gradient: Eq. 4.8	
LHTI	Stationary: Eq. 4.4	Temp gradient: Eq. 4.10	

Table 4.1: Summary of dispersion relations for perpendicular lower-hybrid instabilities

in the "lab" reference frame with no $E \times B$ drifts. Therefore, the electron density-gradient dielectric is used, and the ions use a drifting dielectric, identifying the ion drift with its diamagnetic drift, $V_{\perp i} = +T_i/eBL_n$.

Next, MTSI [31] is driven by "non-equilibrium" drifts, i.e. not associated with density or temperature gradients. (In any case, gradients are not included self-consistently in the calculation.) This instability is most easily calculated in the electron frame, and therefore the electron dielectric with no gradients is used, and all drift is assumed to reside in the ions. However, the final result can be put into a different reference frame with a simple Doppler shift.

Finally, for the LHTI, the gradient of parallel electron temperature is kept in the electron dielectric, and the ions are assumed to be at rest. To model the weaker, kinetic version of the instability (i.e. if the gradients only exist within the high-energy tail of the electrons), it is convenient to consider separate hot and cold electron populations, using the density gradient dielectric of the hot electrons. However, the final instability condition is even simpler than this and will be discussed below.

First, we summarize ion dielectric results. As mentioned above, the ions are considered to be unmagnetized, and are treated by straight-line orbits. (This is found to be the correct treatment as long as the growth rates are larger than ω_{ci} [87].) If the ions are stationary, then

$$\epsilon^{(i)} = \frac{1}{k^2 \lambda_{Di}^2} \left[1 + \frac{\omega}{k v_{ti}} Z \left(\frac{\omega}{k v_{ti}} \right) \right]. \qquad \text{(Stationary)} \tag{4.4}$$

Here Z is the well-known plasma dispersion function [88], and λ_{Di} the Debye length evaluated with the *ion* temperature. For purposes of LHDI or MTSI, the ions are drifting across

the field with a speed $V_{\perp i}$, yielding

$$\epsilon^{(i)} = \frac{1}{k^2\lambda_{Di}^2}\left[1 + \frac{\omega - k_y V_{\perp i}}{kv_{ti}} Z\left(\frac{\omega - k_y V_{\perp i}}{kv_{ti}}\right)\right]. \qquad \text{(Drifting)} \tag{4.5}$$

In the LHDI, the ion drift is attributed to the ion diamagnetic drift: $V_{\perp i} = +T_i/eBL_n$.

Next, the electron contribution is calculated with the standard orbit integrals, including gradients calculated within the local wave approximation [86]. This yields

$$\epsilon^{(e)} = \frac{1}{k^2\lambda_{De}^2}\left[1 + \hat{\ell}\frac{\omega}{k_{||}v_{te}} Z\left(\frac{\omega}{k_{||}v_{te}}\right)\Gamma_0(z)\right]. \tag{4.6}$$

Compared with the full expression (which includes the sum over the Doppler-shifted cyclotron resonances), here we have simplified to $\omega \ll \omega_{ce}$ and kept only the $n = 0$ term, because we are looking for modes near the lower-hybrid frequency. Here $\Gamma_0(z) = I_0(z)\mathrm{e}^{-z}$, where $z = k_\perp^2 T_e/m_e\omega_{ce}^2$, and I_0 is the modified Bessel function of the first kind. This is the well-known Bessel function term which contains the finite gyroradius effects for the electrons.

Gradient effects are contained within the operator $\hat{\ell}$,

$$\hat{\ell} \equiv 1 + \frac{k_y T}{m\omega\omega_{ce}}\left(\frac{1}{n}\frac{\partial n}{\partial x} + \frac{\partial T}{\partial x}\frac{\partial}{\partial T}\right). \tag{4.7}$$

(Here the expression differs in a sign from Ref. [86]; there the cyclotron frequencies are kept as signed, algebraic quantities. In the discussion here, ω_{ce} is the *unsigned* electron cyclotron frequency.) With no gradients, i.e. for MTSI,

$$\epsilon^{(e)} = \frac{1}{k^2\lambda_{De}^2}\left[1 + \xi_e Z\left(\xi_e\right)\Gamma_0(z)\right]. \qquad \text{(No gradients)} \tag{4.8}$$

Here ξ_e abbreviates $\omega/k_{||}v_{te}$.

On the other hand, for LHDI the density gradient is kept and the relevant electron dielectric is,

$$\epsilon^{(e)} = \frac{1}{k^2\lambda_{De}^2}\left[1 + \left(1 - \frac{\omega_{*n}}{\omega}\right)\xi_e Z\left(\xi_e\right)\Gamma_0(z)\right]. \qquad \text{(Density gradient)} \tag{4.9}$$

Here $\omega_{*n} \equiv -k_y T_e/eBL_n$ is the drift frequency due to density gradients, and L_n is the density gradient scale length. This discussion will employ explicitly-signed drift frequencies:

the electron drift frequencies ω_{*n} (and ω_{*T}, below) are negative quantities because the electron diamagnetic drift is negative in this geometry and k_y is regarded as positive. In general, the sign of a drift frequency ω_* for either electrons or ions emerges from $\mathbf{k}$ dotted into the relevant diamagnetic drift velocity.

Finally, keeping the gradient of *parallel* temperature, the electron dielectric is [86]

$$\epsilon^{(e)} = \frac{1}{k^2\lambda_{De}^2}\left[1 + \left\{\xi_e Z - \frac{\omega_{*T}}{\omega}\left(\xi_e^2 + (\xi_e^2 - \tfrac{1}{2})\xi_e Z\right)\right\}\Gamma_0\right]. \qquad \text{(Temp. grad.)} \qquad (4.10)$$

Here $\omega_{*T} \equiv -k_y T/eBL_T$ is the corresponding drift frequency for the temperature gradient, whose scale length is L_T. Also, $Z(\xi_e)$ is abbreviated as simply Z for clarity. This expression is more complicated than Eq. 4.9 due to the derivative operator $\partial/\partial T$ acting on $\xi_e Z(\xi_e)$. The Z-function recursion relationship $Z' = -2(1 + \xi Z)$ was also used to simplify the resulting expression.

The expression above calculated the gradient near a point where $T_{||} \simeq T_\perp$. If general anisotropy is allowed, then the expression generalizes to

$$\epsilon^{(e)} = \frac{1}{k^2\lambda_{D,\perp}^2}(1 - \Gamma_{0,\perp}) + \frac{\Gamma_{0,\perp}}{k^2\lambda_{D,||}}\left[1 + \left(1 - \frac{\omega_{*T_{||}}}{\omega}\, T_{||}\frac{\partial}{\partial T_{||}}\right)\xi_{e,||}Z(\xi_{e,||})\right]. \qquad (4.11)$$

The subscripts to the various quantities involving temperature (λ_D, ξ_e, L_T, etc.) now explicitly refer to the relevant temperature used.

Armed with these dispersion relations, we can proceed to calculate growth rates. Figure 4-7 shows a calculation of instability due to temperature gradient (i.e. filamentation). The dispersion relation is solved for a range of $k_{||}$ and $k_\perp$, and Fig. 4-7(a) plots contours of the growth rate γ, where it is positive, over $(k_{||}, k_\perp)$ space (assuming $k_\perp = k_y$). For this plot we have used $L_T = 100\rho_e \simeq 2$ cm, finding peak instability at $k_\perp\rho_e \simeq 0.8$, and $k_{||}\rho_e \simeq 3\times10^{-3}$. Thus, $k_{||}/k_\perp \simeq 4\times10^{-3} \simeq (m_e/m_i)^{1/2}$, which is exactly in the lower hybrid regime. At each $(k_{||}, k_\perp)$, ω is found as well and Fig. 4-7(b) plots the maximum growth rate associated with each frequency; peak growth rates are found for real ω near the lower-hybrid frequency. For completeness, Fig. 4-7(c) plots the $k_{||}$ and $k_\perp$ associated with the (ω, γ) pairs from Fig. 4-7(b). These trace out the heavy, black curve superimposed on the contours in Fig. 4-7(a).

Because of overall interest in the temperature instability, it is useful to examine the analytic structure of the dispersion relation in greater detail. First, if one takes the cold

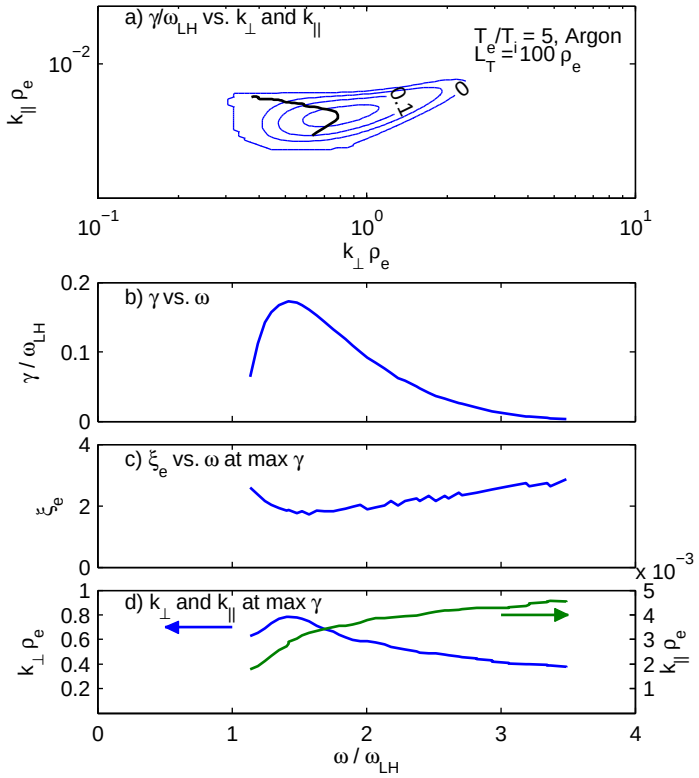

Figure 4-7: Instability plots for the lower-hybrid temperature-gradient instability. (a) Contours of γ in $(k_\perp, k_{||})$ space, calculated for parameters $L_T = 100\rho_e \simeq 2$ cm, $T_e/T_i = 5$, argon mass ratio, and $\omega_{pe}/\omega_{ce} = 10$. The thick dark curve is the path of maximum γ at each ω. (b) maximum γ at each ω. Note that modes exist only for $\omega \geq \omega_{LH}$. (c) $\xi_e = \omega/k_{||}v_{te}$ associated with the maximum γ at each ω. (d) $k_\perp$ and $k_{||}$ associated with the maximum γ at each ω. (Note that here positive frequencies are plotted even though this instability propagates in the electron diamagnetic direction.)

plasma limit of the dispersion relation for LHTI (Eqs. 4.10 or 4.11 plus Eq. 4.4) one finds the cubic dispersion relation

$$0 \simeq 1 - \frac{\omega_{ce}^2 \cos^2\theta}{\omega^2}\left(1 - \frac{\omega_{*T}}{\omega}\right) - \frac{\omega_{LH}^2}{\omega^2}. \tag{4.12}$$

(Here we have also taken the limits $\omega_{pe}^2/\omega_{ce}^2 \to \infty$ and $\sin^2\theta \to 1$, but left $\cos^2\theta$ intact.) Note first that if $\omega_{*T} = 0$ then the cold lower-hybrid dispersion relation $\omega^2 = \omega_{LH}^2 + \omega_{ce}^2\cos^2\theta$ is recovered. From this cubic dispersion relation, the rough instability criterion $\omega_{*T}/\omega > 1$ is immediately apparent, as that will invert the sign of the second term, leading to the possibility of imaginary ω. This suggests that to find instability, $|\omega|$ should be minimized and $|\omega_{*T}|$ maximized. The former occurs when $|\omega| \to \omega_{LH}$, i.e. $k_\perp \gg k_{||}$ in accordance with the lower-hybrid dispersion relation (Eq. 4.2). Next, $|\omega_{*T}|$ is similarly maximized when k_y is as large as possible, again consistent with perpendicular propagation. These are the primary reasons that perpendicular drifts and gradients drive lower-hybrid waves. Note, finally, that to find instability ω will follow the same sign as ω_{*T} (so as to flip the sign of the second term). In this particular geometry, ω_{*T} is negative and therefore the unstable ω will have a negative real component; in general, this instability propagates in the *electron* diamagnetic direction.

Solving for the roots of this cubic equation reveals that the marginal stability condition is $|\omega_{*T}| \geq \omega_{LH}$, with the most unstable angle at $\cos\theta = (2m_e/m_i)^{1/2}$, i.e. for very perpendicular angles so that $|\omega_r| \simeq \omega_{LH}$. Unfortunately, cold plasma theory does not reveal the allowed k_y, but from kinetic theory it is known that $k_y\rho_e \lesssim 1$ otherwise the finite gyroradius effects will come in. Therefore, the instability condition is $L_T \lesssim 0.7\rho_s \times (k_y\rho_e)$.

An alternative marginal stability condition can be found from studying the imaginary part of the dispersion relation. Near marginal stability, $\omega = \omega_r + i\gamma$, where γ is the small imaginary growth rate of the instability. Following standard procedure it can be found from from $\gamma \approx -\epsilon_I/(d\epsilon_R/d\omega|_{\omega_r})$, where ϵ_I is the imaginary part of the dielectric; once ω_r has been found from the roots of ϵ_R, the real part of the dielectric. For the purposes of estimating growth rates in the limiting case (ω_{*T} not large), the modes excited are found to be approximately cold, lower-hybrid modes with $\omega^2 \simeq \omega_{LH}^2 + \omega_{ce}^2\cos^2\theta$, and furthermore,

$$[d\epsilon_r/d\omega|_{\omega_r}]^{-1} \approx \frac{1}{2}\frac{\omega_{ce}^2}{\omega_{pe}^2}\omega_r. \tag{4.13}$$

Therefore, based on the imaginary part of Eq. 4.10,

$$\gamma \approx \frac{\sqrt{\pi}}{k^2\rho_e^2}\left[-\omega_r + \omega_{*T}\left(\xi_e^2 - \tfrac{1}{2}\right)\right]\ \xi_e \exp\left(-\xi_e^2\right)\Gamma_0. \tag{4.14}$$

The two terms in brackets represent competition of Landau damping on the electrons with the instability drive from the gradient. The Landau damping is negative-definite in ω_r due to the additional factor of ω_r in ξ_e; its contribution to γ is negative for both positive and negative ω. However, the drift term can contribute to positive growth if $(\omega_r\,\omega_{*T}) > 0$; once again, the mode propagates in the electron diamagnetic direction. The competition of these two terms implies an instability bound $|\omega_{*T}/\omega| \gtrsim 1/\xi_e^2$. As found in Fig. 4-7, ξ_e can be near 2 in the regions of instability, so the marginal instability condition is slightly relaxed compared to the cold-fluid bound $|\omega_{*T}| > \omega_{LH}$. Instead, the kinetic bound is closer to $|\omega_{*T}| > \omega_{LH}/2$, equivalently $L_T \approx \rho_s$, roughly 4 cm on VTF. (Note that this theory does not treat the ion dynamics correctly in true limit $\gamma \to 0$, where in general ion-cyclotron resonances must be retained; the theory employed here assumes $\gamma \gg \omega_{ci}$, and therefore the marginal instability condition is only approximate. This is discussed in detail in Ref. [87].)

Overall, optimizing Eq. 4.14 to find the peak growth rate is non-trivial due to the dependence of ω on both $k_\perp$ and $k_{||}$ and ω_{*T} on $k_\perp$. However, the purely-numerical solutions in Fig. 4-7 can be "checked" based on this formula, using the numerically determined ω, ξ_e, etc., from the figure. To compare at peak growth rate, Eq. 4.14 is evaluated with the parameters $\omega/\omega_{LH} = 1.4$, $\xi_e = 1.8$, $k_\perp\rho_e = 0.8$, and $\omega_{*T}/\omega_{LH} = 1.1$ (at $L_T/\rho_e = 100$). This yields the semi-analytic growth rate $\gamma/\omega_{LH} \approx 0.22$, which is of the correct magnitude, but about 30% larger than the pure-numerical peak growth rate $\gamma/\omega_{LH} \simeq 0.18$. Nonetheless, Eq. 4.14 qualitatively shows the main physics mechanisms relevant for determining the growth rate: competition between gradient drive and Landau damping, which pushes the resonant ξ_e to near 2, which is off the peak of the Landau damping, but not so large that only the exponentially small tail drives the instability; and, competition between maximizing ω_{*T} at large k_y and loss of growth due to the finite gyroradius effects of $\Gamma_0/(k\rho_e)^2$ as $k_\perp\rho_e$ approaches 1.

Figure 4-8 presents some simple parametric scans over the temperature scale length L_T (a), and electron-ion temperature ratio T_e/T_i (b). The temperature scale length is crucial, and the peak growth rate increases sharply with decreasing L_T. In fact, gradient

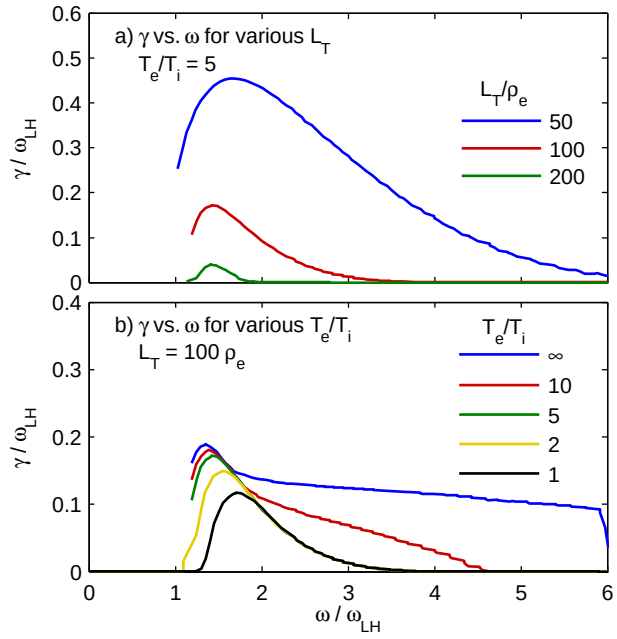

Figure 4-8: (a) Growth rate of the lower-hybrid temperature instability for various gradient lengths L_{Te}. (b) Growth rate for various temperature ratios. As $T_e/T_i \to \infty$ a long "tail" of perpendicular ion-acoustic instability appears.

scales $L_T \simeq \rho_s \simeq 200\rho_e$ will be required for strong growth on the 10 μs time-scale of the reconnection events (i.e. $\gamma \sim 0.1\omega_{LH} \sim 5 \times 10^6$ s^{-1}). The temperature plays a more minor role in the growth rate. One effect is that, at $T_i = 0$, a broad band of higher-frequency modes can be excited in addition to the peak instability near ω_{LH}. These are actually perpendicular ion-acoustic waves [86]; they are found to be stabilized, however, when the ions acquire a finite temperature.

As discussed above, it may also be necessary to consider instability drive not by bulk temperature gradient, but a weaker, kinetic drive by the spatial gradient of fast electrons. To analyze this case, one can imagine hot and cold electron populations and consider the gradient instabilities of these. However, it is more direct to simply study the general imaginary contribution to the dielectric from gradients [86]. The gradient contributes a small imaginary part to the dielectric,

$$\epsilon_I^D = +\frac{\pi e^2}{\epsilon_0 m_e k^2} \int \left(\frac{\mathbf{k} \times \nabla f}{k_z \omega_{ce}} \right)_{\omega/k_z} d^2 v_\perp. \tag{4.15}$$

(Again, this expression differs in sign from Ref. [86] because the electron gyrofrequency is unsigned here.) This kinetic drive must compete against Landau damping on the electrons

at the same phase velocity,

$$\epsilon_I^L = -\frac{\pi e^2}{\epsilon_0 m_e k^2} \int \left. \frac{\partial f}{\partial v_z} \right|_{\omega/k_z} d^2 v_\perp. \tag{4.16}$$

Meanwhile, the real part of ω will derive simply from the bulk dielectric, e.g. Eq. 4.8, and will typically be a cold lower-hybrid mode that can resonate with the fast tail electrons. Next, if the fast electron population is imagined to have a gradient length scale L and effective temperature T near the relevant phase velocity, then the marginal stability condition is $L/\rho_s < 0.7(k_y\rho_e) \times (\omega_{LH}/\omega)$ where ρ_e and ρ_s have been evaluated with this effective tail temperature. Just as for the temperature-gradient-driven modes, these modes are most unstable at $\omega = \omega_{LH}$, again implying that gradient scales of order ρ_s can trigger these modes. Such gradient scales have been directly observed in the fast electron populations by the energy analyzer probe. The question is how deeply these gradients extend into the bulk of the distribution, as the instability drive also scales with f at the resonant phase speed, and therefore becomes increasingly weak with distance from the bulk of the distribution.

We have also carried out a similar analysis of the MTSI and LHDI dispersion relations. Figure 4-9 plots growth rate versus frequency for the MTSI, for various perpendicular drift speeds (a), and temperature ratios (b). The MTSI is very similar in structure to the temperature instability: peak growth is found for modes with a finite $k_{||}$, again with $k_{||}/k_\perp \sim (m_e/m_i)^{1/2}$ at maximum growth. For argon mass ratios and a temperature ratio of 5, the marginal instability is $V_{\perp i}/C_s \simeq 1.3$. The MTSI has a similar temperature dependence to the temperature-gradient instability, as well; the instability increases with temperature ratio and, as $T_e/T_i \to \infty$, a tail of high-k, perpendicular acoustic waves appears on the spectrum.

The LHDI, on the other hand, has a different spectrum in k-space than the MTSI and the temperature instability. Figure 4-10(a) plots γ versus $k_{||}$ and $k_\perp$ for a calculation with $L_n = \rho_s$. The LHDI is a "flute" mode; its peak growth rate comes at $k_{||} = 0$. Furthermore, its growth tends to *decrease* with temperature ratio at fixed gradient length scale. This is because it is largely driven by the ion drift, and here we have considered the "pure" gradient driven LHDI, which fixes $V_{\perp i} = T_i/eBL_n = -(T_i/T_e) \times V_{\perp e}$, so that the ion drift is seen to *decrease* with increasing temperature ratio (at fixed scale length). A final note is that there is appreciable growth over a wide band of $k_\perp$, including strong growth for $k_\perp\rho_e \sim 10$,

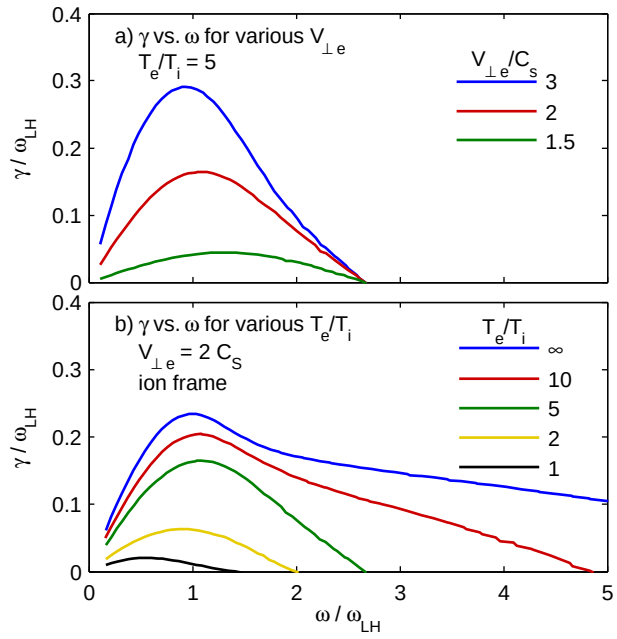

Figure 4-9: Growth rate of modified two-stream instability (MTSI) for various perpendicular drifts (a) and temperature ratios (b). As $T_e/T_i \to \infty$ a long tail of perpendicular ion-acoustic instability appears.

as is visible in Fig. 4-10(a). Therefore, there are large possible Doppler shift effects, so the frequency spectrum plotted in Fig. 4-10(b) can be strongly shifted around depending if one looks at the growth spectrum in the ion or electron frames.

In summary, it is found that at least three perpendicular drift or gradient mechanisms exist which will drive lower-hybrid waves. They comprise three independent "bases" for instability: density, temperature, and drift, and in practice any mixture of these can operate. We now discuss the particular drive mechanisms and expectations for each instability in more detail, and find that the temperature instability is likely the strongest effect in VTF.

LHDI: This instability is driven as a result of large density gradients. In the strong guide-field regime, the LHDI can be driven if the density scale length in the current sheet approaches ρ_s, and this is roughly the scale of current sheets observed on VTF [52] immediately before the onset of the reconnection event. However, as found in Fig. 4-6, fluctuations tend to *lag* the peak of the reconnection event, whereas the existence of a thin current sheet and the associated gradients *precedes* the reconnection event. This suggests that LHDI due simply to having a thin current sheet is *not* the cause of the lower-hybrid waves in VTF. On the other hand, it could be that even sharper density gradients are formed during the

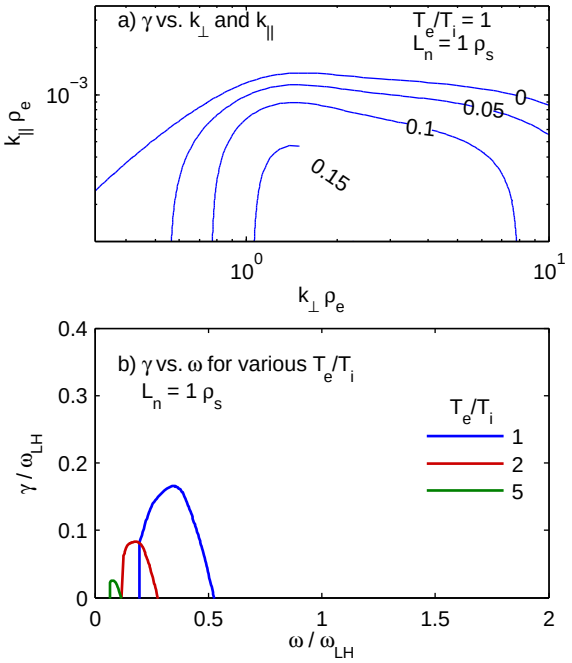

Figure 4-10: Growth rates for lower-hybrid drift instability (LHDI) in the VTF parameter regime. (a) Contour plot of growth rate of LHDI showing maximum growth at $k_{||} = 0$. (b) Growth rate of LHDI for various temperature ratios.

disruption of the current sheet. In fact, computational studies of guide-field reconnection predict a strong quadrupolar density perturbation near the x line in coincidence with reconnection events [28]. (This is within the set of "laminar" fast reconnection mechanisms discussed briefly in Chapter 1.) Experiments on VTF are presently attempting to observe this effect, as it would be a major result.

MTSI: "Non-equilibrium" perpendicular current that could drive MTSI might arise during the onset of the reconnection events, since they are observed to turn on about as fast as the ion-cyclotron time, $\omega_{ci}^{-1} \simeq 6\ \mu$s. Furthermore, ions are also potentially unmagnetized near the current sheet due to finite gyroradius, as $\rho_s \sim 3$ cm is the same size scale as the current sheets [52]. At the same time, the reconnection flows are large; the outflow speed has been observed to be up to the (upstream) Alfvén speed, $\simeq 1 \times 10^4$ m/s $> c_s$. However, the electric fields associated with the outflow have not yet been measured below the ρ_s scale where decoupling should occur. This is a high priority for future experiments. Challenges include observing the electric fields (which is the gradient of the measured potential) on fine spatial scales and controlling for systematic errors between the easily measured floating potential V_{float} and the true space potential V_{plasma}.

Second, recent investigation has also found that the reconnection events on VTF are not completely axisymmetric, but rather start at one toroidal location and appear to propagate toroidally, "unzipping" the magnetic field. Such local reconnection corresponds to a local disruption of toroidal current, but if this does not happen symmetrically around the device then substantial perpendicular currents can be driven to maintain $\nabla \cdot \mathbf{j} = 0$. Prior to reconnection onset the electron parallel drift is estimated to be $v_{de} \sim 50\ c_s$; only a small fraction of this has to be diverted across the field to drive MTSI. Both of these mechanisms would be expected to correlate well or slightly lag the reconnection events, as they are driven in consequence of the reconnection process.

LHTI: Both LHDI and MTSI, being driven by pure perpendicular flows, are independent of the sign of $k_{||}$ and can in principle drive waves with both positive and negative $k_{||}$. However, our phase measurements find $k_{||}$ pointing preferentially in the electron parallel drift direction (Fig. 4-4). This suggests a connection to the energization of electrons produced by the reconnection event; this is a subtle, but useful, clue that it may be the gradient instability of fast electron filaments which drives the lower hybrid waves. Furthermore, "filamentation" of the fast electron population on a scale near 1 cm—implying short gradient scale lengths of temperature—has already been observed using the energy-analyzer probe. However, the energy analyzer is only studying the tail of the electron population, so it would be very useful to conduct further study of temperature fluctuations of bulk electrons. These two mechanisms could also be better-discerned if improved $k_{||}$ measurements were available, as the temperature instability will have $\omega/k_{||}$ closer into the bulk whereas the tail instability will have $\omega/k_{||}$ resonant with the tail. Unfortunately, such a measurement is very difficult due to strong projection effects (of $k_\perp$ onto $k_{||}$) in the lower-hybrid regime. Finally, the observation that fluctuations slightly lag the reconnection events fits very well with electron-temperature-gradient instabilities, since the reconnection events are known to energize the electrons, both from the energy analyzer measurements presented in the previous chapter, and in the discussion of Trivelpiece-Gould modes below, which are found to be driven by a small population of fast electrons energized by the reconnection event.

To summarize, of the three proposed instability mechanisms, the temperature gradient instability fits reasonably well and requires the fewest additional assumptions. Future work on VTF will continue to improve measurements of the evolution of the in-plane electric fields, plasma flows, and density gradients during the reconnection events, and therefore

provide further information on the various instability mechanisms.

4.3.4 Lower-hybrid waves: Parallel excitation

This section describes some of the parallel excitation mechanisms of lower-hybrid waves. However, we find that the parallel plasma drifts in VTF are not large enough to trigger these instabilities, further suggesting the importance of the perpendicular instability mechanisms discussed above.

The parallel excitation mechanisms include "slide-away" lower-hybrid waves [89], drive by super-thermal electron beams [90], or Buneman instability. Qualitatively our results do bear quite similar resemblance to observations of the "slide-away" regime on tokamak experiments, where ohmic electric fields approaching the runaway electric field were used to heat the plasma. Copious lower-hybrid waves and also higher-frequency Trivelpiece-Gould modes ($\omega = \omega_{pe} k_{||}/k$—in these experiments $\omega_{ce}^2 \gg \omega_{pe}^2$) were observed. In interpreting these results, Coppi and collaborators [89] found that the lower-hybrid waves could be driven unstable based on a positive slope in the electron distribution function which formed based on separation of the "trapped" and "circulating" populations of electrons. Here, the trapping is caused by the standard mirror force in the tokamak geometry. Based on the variation of magnetic field along the flux surface $2\epsilon = \Delta|B|/|B|_{avg}$, a low density ($n_t/n_0 \sim \sqrt{2\epsilon}$), cold ($T_{t,||}/T_0 \sim 2\epsilon$) population of trapped electrons is unable to be accelerated by applied electric fields. With enough drift in the circulating population, a region of positive slope opens up in the reduced distribution $\int f d^2 v_\perp$, near $v_{de} = j/ne$, and modes resonant with this velocity can be lower-hybrid modes.

However, a few troubles cloud this hypothesis. First, unlike in high-temperature tokamak plasmas, VTF is not in a banana regime with a well-defined trapped population of electrons. The well-known criterion here is that the collision frequency must be much smaller than $\epsilon^{3/2} v_{te}/qR_0$, where q is the rotational transform, R_0 the major radius, and ϵ the aspect ratio of the flux surfaces, described above. We find that $q \gtrsim 3$ over most of the volume of VTF for the magnetic fields used here, but diverges close to the x point. The ϵ-dependence enters in to account for the typical low parallel velocity of trapped electrons and the short distance the particle has to diffuse in velocity space to de-trap. Using $\epsilon = 0.15$, based on typical flux surfaces near the x point, this condition is not satisfied for nominal 15 eV temperatures, and is not well satisfied until temperatures near 100 eV are attained,

which has not been observed for the bulk. In addition, for $\epsilon \simeq 0.15$, the drift speeds v_{de} required for instability are approximately 0.3 v_{te} [91]. This has not been observed on VTF; typically $v_{de}/v_{te} \simeq 0.1$, averaged over the current sheet. If a higher temperature is assumed to so that the banana regime can prevail, then this ratio is even smaller. In conclusion, VTF does not appear to be in the correct regime for excitation of these slide-away lower-hybrid modes.

Waves near ω_{LH} can also be driven by strong electron-ion two-stream instability (Buneman instability) as a second branch due to finite magnetic field [79]. The peak unstable frequency in the ion frame has $\omega \simeq \omega_{LH}(m_i/m_e)^{1/6}$. However, this is not a likely explanation, as these modes have smaller growth rates than the standard Buneman instability [where $\omega \simeq \omega_{pi}(m_i/m_e)^{1/6}$], and further have $k_{||} \simeq k_{\perp}$, contrary to the strong observed anisotropy. Finally, Buneman instability has even stronger electron current requirements than the slide-away lower hybrid waves: $v_{de} > v_{te}$, whereas the VTF current sheets possess $v_{de} \simeq 0.1 v_{te}$ as discussed above. (However, some recent 3-D particle simulations [37] *have* found Buneman instability in strong-guide field current sheets, but these were in an ultra-low-*beta*, force-free current sheet regime; the density was much lower, leading to super-thermal electron-ion drifts were obtained.)

A final parallel drive mechanism is excitation by super-thermal electron beams, as discussed by Papadopoulos and Palmadesso [90]. In general, a wide band of modes can be excited by electron beams, and the growth rates of modes near ω_{LH} are less than for high-frequency modes (ω_{ce}), since growth rates are found to scale with frequency. However, Papadopoulos and Palmadesso found that *narrow* beamlets might preferentially excite lower-hybrid waves since the perpendicular group velocity ($\propto k_{||}$) becomes small near ω_{LH}, so the *convective* growth rate $k_{i,\perp}$ actually maximizes at ω_{LH}. This topic will be explored more completely in Section 4.4, in connection with observed high-frequency beam-driven modes.

4.3.5 Anomalous resistivity

Here we make a simple estimate of the anomalous momentum coupling due to growth of these waves, using quasi-linear theory. The theory, presented in Appendix A, calculates the net momentum transfer from electrons to fluid ions due to the growth of the waves. This is cast into the form of an effective parallel electric field due to the waves, which is to be

compared against the DC reconnection electric field. As usual, the quasi-linear momentum coupling is proportional to the instability growth rate and to the saturated amplitude. For the growth rate, one inserts an estimate from linear theory, and here we will use the experimentally-measured mode amplitude. For the growth rate, we will use estimates from the temperature gradient instability.

Quasi-linear theory predicts a parallel electric field

$$E_{ql} \sim \frac{2e}{m_i} \frac{\omega_r \gamma}{|\omega^4|} k_{||} k^2 \left\langle \tilde{\phi}^2 \right\rangle . \tag{4.17}$$

The direction of $k_{||}$ observed (Fig. 4-4) is in the direction of the electron drift, which is the correct direction to remove momentum from the drifting electron population. To substitute numbers, it is useful to normalize frequencies to the lower-hybrid frequency. Further, we use the approximation $\omega/k_{||} \simeq \omega_{ce}/k_{\perp}$ since we do not have an excellent measurement of $k_{||}$. These steps yield,

$$E_{ql} \sim \frac{1}{\sqrt{2}} \left(\frac{\gamma}{\omega_{LH}} \right) \left(\frac{\omega_r}{\omega_{LH}} \right)^{-2} (k_{\perp}\rho_e)^3 \left(\frac{kT_e}{e\rho_s} \right) \left[\left(\frac{e}{kT_e} \right)^2 \left\langle \tilde{\phi}^2 \right\rangle \right] . \tag{4.18}$$

For amplitudes, we use an estimated calibration factor for raw Langmuir signals to potential fluctuations ∼40, and use typical raw fluctuation power $\sim 10^{-3}$ V^2 (see Figure 4-6), giving $e\phi_{rms}/kT_e \sim 0.1$. The quasi-linear electric field is then estimated at $\omega_r = \omega_{LH}$, $\gamma \sim 0.3\omega_{LH}$, and $k_{\perp}\rho_e = 1$, finding $E_{ql} \sim 1$ V/m. This simple estimate is too small, by about a factor of 15, to explain the typical reconnection electric fields of about 15 V/m.

Overall it is hard to draw firm conclusions from this estimate, based on the limitations of the theory and difficulty trusting the calibration of the Langmuir probes. Nonetheless, the result does suggest that these modes are not essential sources of anomalous resistivity for the reconnection process in VTF. Further hurdles for interpreting these waves as an essential source of anomalous resistivity in the plasma include the large (> 1 order of magnitude) variation in fluctuation power observed from shot to shot, even as peak reconnecting electric fields only vary by 30%, and the systematic time delay of these fluctuations compared to the reconnection rates (see Figure 4-6). These qualitative observations are an important complement to the highly crude quantitative estimates above.

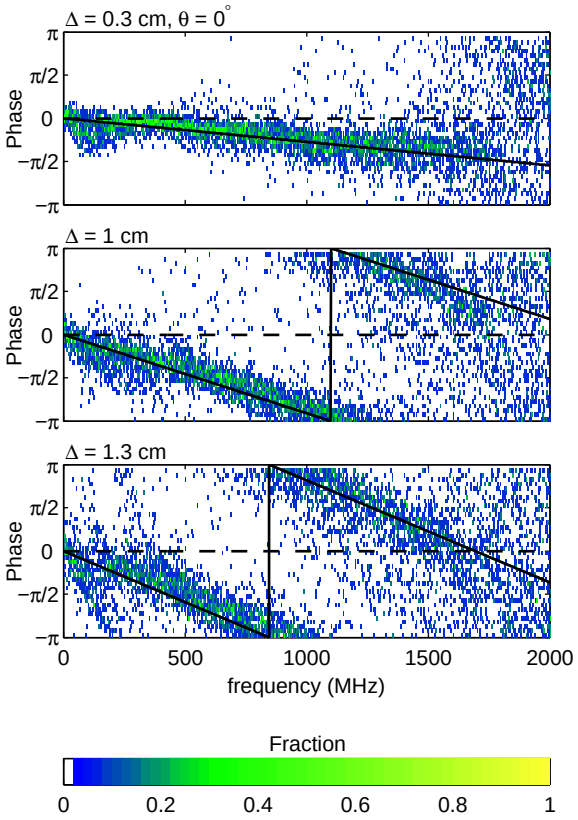

Figure 4-11: Phase measurements for various probe separations over the Trivelpiece-Gould frequency regime $0 < f < 2$ GHz. Probes are aligned parallel to the magnetic field. The plot is shown in color histogram form, showing fraction of discharges which measured a given phase at given frequency.

4.4 Trivelpiece-Gould regime

4.4.1 Measurements

We have a conducted similar analysis of the higher-frequency branch, over the frequency range 200 MHz $< f <$ 2 GHz. Overall, these waves have proven much easier to analyze owing to improved coherence. Furthermore, the modes are not nearly as anisotropic (between $k_{||}$ and $k_{\perp}$) as the lower-hybrid waves, which also helps matters. Figure 4-11 presents phase measurements for probes aligned parallel to the field over the entire regime up to $f_{ce} = 2$ GHz. As before, phase is measured from the statistical cross-correlation evaluated for the 10 μs window bracketing the reconnection events.

In this frequency regime a clear parallel dispersion relation $k_{||}(\omega)$ is apparent. Interestingly, over this range the dispersion is *linear* with $k_{||}(\omega) \propto \omega$, i.e. $\omega/k_{||}$ approximately a

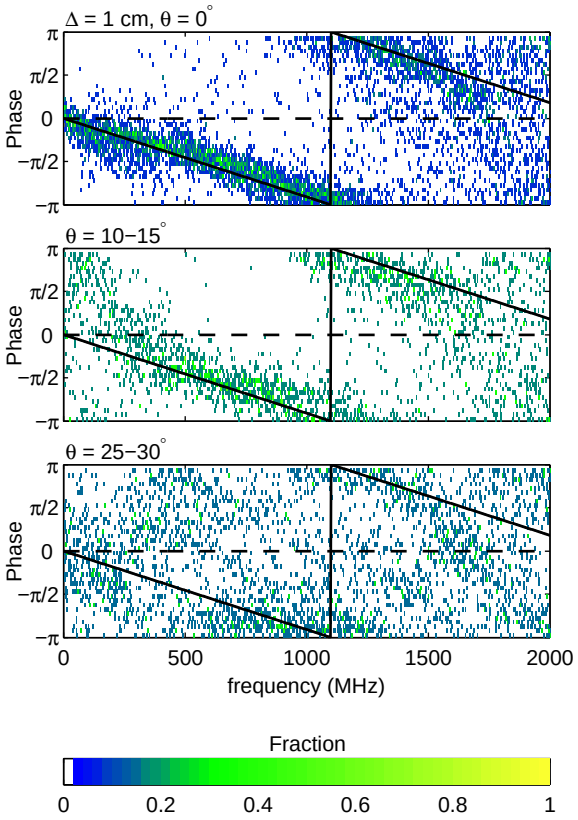

Figure 4-12: Phase measurements versus frequency for various probe angles with respect to the magnetic field over the Trivelpiece-Gould regime $0 < f < 2$ GHz. The probe separation is 1 cm. The plot is shown in color histogram form, showing fraction of discharges which measured a given phase at given frequency.

constant phase velocity (v_{ph}) Comparing probes at the three separations, one finds consistent v_{ph}, so that the phase Φ satisfies

$$\Phi = k_{||}(\omega)\Delta = \frac{2\pi f}{v_{ph}}\Delta \tag{4.19}$$

In Figure 4-11 are plotted fit curves using the known Δ for each pair, using the common fit parameter $v_{ph} = 2.2 \times 10^7$ m/s. (Note that the direction of $k_{||}$ and v_{ph} is is consistent with the direction of electron drift.) $k_{||}$ takes on a wide range of values, with the typical value of 300 m^{-1} at 1 GHz, and an extrapolated 600 m^{-1} at 2 GHz. This phase velocity is very fast compared to the electron thermal speed, $v_{ph}/v_{te} \sim 10$.

Figure 4-12 shows that the coherence falls for these waves with increasing angle from the magnetic field. (Note that coherence also falls with frequency, even for parallel correlation,

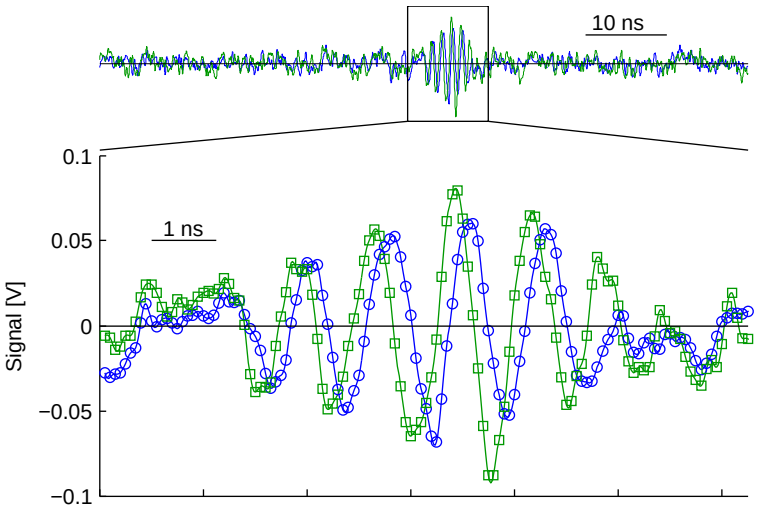

Figure 4-13: Observation of a wave packet of Trivelpiece-Gould waves.

but this happens since fluctuation power approaches the noise level as f approaches f_{ce}.) In contrast to the lower-hybrid waves, here we plot data from the probe pair with 1 cm separation because the decorrelation onset is slower. Furthermore, 30° separation is required to substantially decorrelate the waves. The parallel dispersion in Fig 4-11 indicates that $k_{||}$ is well-defined at each frequency. However, a dispersion relation $\omega = \omega(k_{||}, k_{\perp})$, still leaves room for a bath of waves with vector $\mathbf{k}_{\perp}$ containing variation in azimuthal angle. As discussed above such a bath effect decorrelates the waves when $k_{\perp}\Delta_{\perp} \simeq \pi$, or therefore $k_{\perp} \simeq 600$ m^{-1}. We therefore estimate that in this range of frequencies $k_{||} \sim k_{\perp}$.

Next, Figure 4-13 shows a that the high-frequency modes often appear as discrete wave packets, rather than simple broadband noise. This is most clear when the high-frequency modes are strong but the low-frequency modes are not. Here, we have filtered the data with a digital band-pass filter (300 MHz to 2 GHz) to isolate the high-frequency mode. The "carrier" frequency in the wave packet is observed to be about 800 MHz, exactly the peak of the typical spectra of the fast modes.

Finally, Fig. 4-14 shows the time correlation of these modes and the reconnection events, evaluated for a large ensemble of discharges, with the probes in the fan configuration as used above. As has been discussed above, these high frequency modes persist long after the reconnection events; here one sees that substantial fluctuations still exist at 25 μs after the reconnection event. This strongly implies that these modes arise as a consequence of the reconnection events. Below we will discuss that a natural interpretation for the excitation

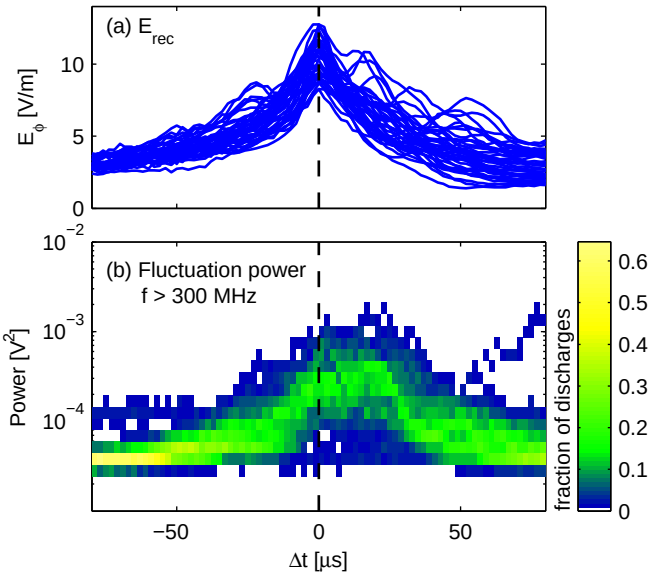

Figure 4-14: Color histogram indicating time-correlation of reconnection electric fields and high-frequency fluctuation observations in the Trivelpiece-Gould regime, 300 MHz $<$ f $<$ 2 GHz. Color indicates fraction of discharges which measured a given power in this frequency band versus time relative to the peak of the reconnection event.

of these modes is instability of a tail of high-energy electrons generated by the reconnection event.

4.4.2 Discussion

To summarize observations, the high frequency branch of observed oscillations has a fairly uniform phase velocity and fluctuation power is observed up to almost exactly f_{ce}. Peak fluctuation power is typically in the range of 1/4 to 1/2 f_{ce}. In this section we show that these are Trivelpiece-Gould modes most-likely driven unstable by bump-on-tail (Čerenkov) instability of high-energy, runaway electrons.

First, as is well known, the electrostatic cold dispersion relation for high frequency plasma waves [79],

$$1 - \frac{\omega_{pe}^2}{\omega^2 - \omega_{ce}^2}\sin^2\theta - \frac{\omega_{pe}^2}{\omega^2}\cos^2\theta = 0, \tag{4.20}$$

predicts two bands of waves. In the limit of well-separated $\omega_{pe} \gg \omega_{ce}$, one band of waves exists between ω_{pe} and $\omega_{UH} = (\omega_{pe}^2 + \omega_{ce}^2)^{1/2}$, and the second exists for $\omega < \omega_{ce}$, with a gap (of cold waves) in between. Our waves fall nicely in the second category, since we observe cutoff of fluctuation power at f_{ce}. This category is the Trivelpiece-Gould branch of the

dispersion relation, with $\omega \simeq \omega_{ce} \cos\theta$. This connects to the lower-hybrid branch discussed earlier when the waves are highly perpendicular and the the ions begin to play a role. For this high frequency branch, however, $k_\perp \sim k_{||}$, consistent with observations here; recall we find $k_\perp \simeq 600$ and $k_{||} \simeq 300$ m^{-1} at 1 GHz.

Standard linear instability theory predicts these high-frequency modes will be driven unstable by beam or other kinetically unstable populations of fast electrons. Adding a fast cold beam beam of particles to the fluid theory leads to the simplest form of instability. This is the classic electron-electron two-stream instability specialized to the limit $\omega \leq \omega_{ce}$ with $\omega_{pe}^2 \gg \omega_{ce}^2$ [79]. (Note that modes near ω_{pe} can also be driven unstable by such a beam.) The dispersion relation is

$$\frac{1}{\omega^2 - \omega_{ce}^2} \sin^2\theta + \frac{1}{\omega^2} \cos^2\theta + \frac{\alpha}{(\omega - k_{||} V_b)^2} \cos^2\theta = 0. \tag{4.21}$$

Here $\alpha = n_b/n_0 \ll 1$ is the relative beam density and V_b the beam velocity. A weak drive implies that unstable modes will be close to the linear bulk modes deriving from the bulk dielectric: $\omega = \omega_{ce}\cos\theta + \delta$, and $\omega = k_{||} V_b$. Note that this already matches experimental observations here in that it predicts a constant $\omega/k_{||} = V_b$. The solution of this dispersion predicts the growth rate [79]

$$\gamma/\omega_{ce} \simeq (\alpha/2)^{1/3} (\sin^2\theta \cos^3\theta)^{1/3} \times \frac{\sqrt{3}}{2}, \tag{4.22}$$

based on the roots of the cubic equation derived by assuming $\delta \ll \omega$. Finally, one finds that the growth rate is dependent on θ: Maximum growth occurs at maximum of $\sin^2\theta \cos^3\theta$, $\theta \simeq 40°$, or $\omega \simeq 0.75\omega_{ce}$.

Within broader kinetic theory there are multiple potential instability mechanisms: warm beams, temperature anisotropy, or even spatial gradients of the fast electrons. Of these the beam- and anisotropy drive are consistent with the observed high-frequency peak, but only the beam-drive is consistent with a fast, uniform phase velocity. In all these cases, the relevant dispersion relation is approximately

$$-\frac{\omega_{pe}^2}{\omega^2 - \omega_{ce}^2} \sin^2\theta - \frac{\omega_{pe}^2}{\omega^2} \cos^2\theta + i\epsilon_I = 0. \tag{4.23}$$

Here ϵ_I is a small imaginary part of the dielectric which drives the instability. For weak

drive, as per usual procedure, ϵ_I is small, and therefore $\omega = \omega_r + i\gamma$, with ω_r deriving from the bulk modes, i.e. $\omega_r = \omega_{ce}\cos\theta$, and $\gamma = -\epsilon_I/(d\epsilon_r/d\omega)|_{\omega_r}$. Here, note that

$$\left[d\epsilon_r/d\omega|_{\omega_r}\right]^{-1} = \frac{\omega_{ce}^3}{2\omega_{pe}^2}\cos\theta\sin^2\theta. \tag{4.24}$$

In general ϵ_I will also have some θ dependence, but the θ-dependence in $d\epsilon_r/d\omega$ already pushes the most unstable modes away from $\theta = 0$, consistent with our measurements.

Kinetic drive mechanisms include Čerenkov instability (inverse Landau damping) due to a small positive slope of the distribution function, temperature-anisotropy instability (i.e. $T_{||} \neq T_\perp$) or even gradients of fast electrons [86]. The anisotropy expected in this case is $T_{||} > T_\perp$ owing to long electron tail that can be drawn out by the strong reconnection electric field; here the instability mechanism derives from the "anomalous" Doppler (AD) resonance between waves and particles with phase velocity $(\omega+\omega_{ce})/k_{||}$ [92]. ϵ_I due to each effect is summarized below:

$$\epsilon_I^C = -\frac{\pi e^2}{\epsilon_0 m_e k^2}\int \left.\frac{\partial f}{\partial v_z}\right|_{\omega/k_z} d^2v_\perp \quad \text{(Čerenkov)}, \tag{4.25}$$

$$\epsilon_I^A = -\frac{\pi e^2}{\epsilon_0 m_e k^2}\int \left(\frac{k_\perp^2 v_\perp^2}{4\,\omega_{ce}^2}\right)\left(\frac{\partial f}{\partial v_z} - \frac{\omega_{ce}}{k_z v_\perp}\frac{\partial f}{\partial v_\perp}\right)_{(\omega+\omega_{ce})/k_z} d^2v_\perp \qquad \text{(AD)}, \tag{4.26}$$

$$\epsilon_I^D = +\frac{\pi e^2}{\epsilon_0 m_e k^2}\int \left(\frac{\mathbf{k}\times\nabla f}{k_z\omega_{ce}}\right)_{\omega/k_z} d^2v_\perp \qquad \text{(Drift)}. \tag{4.27}$$

Here ϵ_I has been calculated based on standard orbit integrals, assuming that $k_\perp\rho_e \ll 1$.

Of these three instability mechanisms, Čerenkov drive is the most consistent with the fairly uniform phase velocity inferred from the measurements; the speed on the positive slope of the presumed bump determines the phase speed. Further, the angle dependence of γ in this case simply follows from $(d\epsilon_R/d\omega)^{-1} \propto \cos\theta\sin^2\theta$, which is maximum at $\theta = 55°$, giving maximum growth at $f = 0.58 f_{ce}$ and a high frequency peak. If this is in fact the drive mechanism, then the presence of such modes implies that electrons with energies above $m_e v_{ph}^2/2 \simeq 1$ keV have been accelerated by the reconnection events. We do not yet have corroborating observations of electrons with energies in this range, but have found fast electrons with energies up to ~250 eV using gridded electron energy analyzers, as discussed in Section 3.3. Also, note that toroidal reconnection electric fields near 15 V/m are near the runaway field and will directly accelerate electrons from rest to 2×10^7 m/s in 10 μs. This

also naturally fits with the observed 10–20 μs time delay between the reconnection events and the observation of the peak of these instabilities (see Figure 4-14).

The other two drive mechanisms do not support the observations as well. First, the drift instability of fast electrons does not lead to a high-frequency peak; instead, as discussed in the last section, this instability preferentially drives lower-hybrid modes with $\theta \simeq 90°$. This is inconsistent with the destabilization of high-frequency Trivelpiece-Gould modes of concern here.

Next, while the anomalous-Doppler effect surely can play a role in the instability of energetic electrons, especially when the bump-on-tail is just marginally unstable, it will not produce an instability spectrum with $\omega/k_{||} \sim 10 v_{te}$ (here v_{te} is the thermal speed of the $\sim$15 eV bulk population). This instability has been studied heavily in the context of fusion research [89, 92], where it was found to have important effects in tokamaks under ohmic heating with large toroidal electric field, or during startup when the density is low. The large electric fields pulled out a long tail to the electron distribution which is first unstable to anomalous-Doppler instabilities.

That research found that the marginal instability of anomalous-Doppler drive is set by competition between the presence of high energy particles at the fast phase velocity $(\omega + \omega_{ce})/k_{||} \simeq \omega_{ce}/k_{||}$ which drive the instability, and Landau damping on the bulk at $\omega/k_{||}$. Even the longest tails have some energy dependence, weakening the instability drive with higher $\omega_{ce}/k_{||}$, an effect which pushes instability to as large a $k_{||}$ as possible, consistent with $\omega/k_{||}$ being past just past the end of the bulk, i.e. at $\omega/k_{||} \gtrsim 3 v_{te}$ or so. Examining our the observations here, we have measured $\omega/k_{||} \approx 2 \times 10^7$ m/s $\simeq 10\ v_{te}$, or about 1 keV. The anomalous-Doppler resonance is therefore near 30 v_{te} for $f \simeq f_{ce}/2$, roughly 10 keV. Therefore, it is difficult to imagine the anomalous-Doppler effect producing the observed dispersion. We have conducted some investigations on the instability of model tail distributions for VTF parameters, and found agreement with the tokamak results. The AD-driven modes are most unstable at oblique angles, $k_{||} \sim k_{\perp}$, and $\omega \sim \omega_{ce}/3$, (so AD instability is also not an explanation of the lower-hybrid waves discussed in the previous section) and peak growth tends to occur with $\omega/k_{||} \simeq 3$–$4\ v_{te}$, just past the end of the bulk distribution.

However, one interesting finding from this research on tokamaks is that the runaway tail distributions were typically *initially* unstable to anomalous-Doppler, but during the quasi-

linear phase of the anomalous-Doppler instability positive-sloped regions were created in the distribution, which was subsequently unstable to Čerenkov instabilities [92]. Therefore these two modes were found to cooperate in removing the energetic tail: the AD tended to isotropize the tail electron distribution, pushing tail electrons to larger $v_\perp$ at constant $v_{||}^2 + v_\perp^2$, and this triggered the Čerenkov instability, which removed the *energy* of the fast electrons, pulling them back into the bulk. (In other experimental work, the AD instability was found to *directly* lead to particle loss—fast electrons were pitch-angle scattered by the waves into orbits where they became trapped in the magnetic ripple and were promptly transported to the walls [93].) In conclusion, the fast uniform phase speed of the observed modes on VTF is not compatible with the AD instability, but it is possible that the AD instability plays an early role in the instability of the fast electrons.

Finally, Fig. 4-15 presents calculated growth rates from the Čerenkov drive on a model distribution with a bump on tail. The bump on tail speed is set so that the parallel phase velocity matches the observed $v_{ph} \simeq 10 v_{te}$. The beam density is assumed to 10^{-4} times the bulk density, consistent with a beam current of 300 A/m^2. The peak growth rate is $\gamma/\omega_{ce} \simeq 10^{-4}$, or about 10^6 s^{-1}, which gives strong growth on the 10–20 μs time scale of the reconnection events.

A remaining question is that the perpendicular group velocity of modes in the electrostatic regime is large. The group velocity of the Trivelpiece-Gould modes satisfies $\mathbf{v_{gr}} \cdot \mathbf{v_{ph}} = 0$, so for modes with $\omega/k_{||} = V_b$ one finds $|\partial\omega/\partial k_\perp| = V_b \cos\theta \sin\theta$ and therefore over most of the spectrum wave packets rapidly transport across the field. For typical propagation angles with $\sin\theta \sim \cos\theta$ the wave packet will transit across the field at roughly the beam velocity, crossing the plasma radius in time short compared to a growth time, which might be estimated as $\lesssim 1$ μs to have observed sufficient growth on the reconnection time scale. This is evident in Fig. 4-15(c), where $k_i \rho_e \simeq 2 \times 10^{-5}$ is found. Using $\rho_e \simeq 200$ μm, this implies a perpendicular growth rate of 0.1 m^{-1}, which requires the waves to traverse the plasma numerous times as they grow.

One way to circumvent this obstacle was considered by Papadopoulos and Palmadesso [90], who considered these beam-driven modes in the lower-hybrid regime, finding that the perpendicular group velocity becomes small near ω_{LH} and therefore $k_i = \gamma/v_{gr,\perp}$ is actually maximum here. Of course, this does not explain the high-frequency peak typically observed in VTF. Furthermore, the temporal growth rate of beam-driven modes in the lower-hybrid

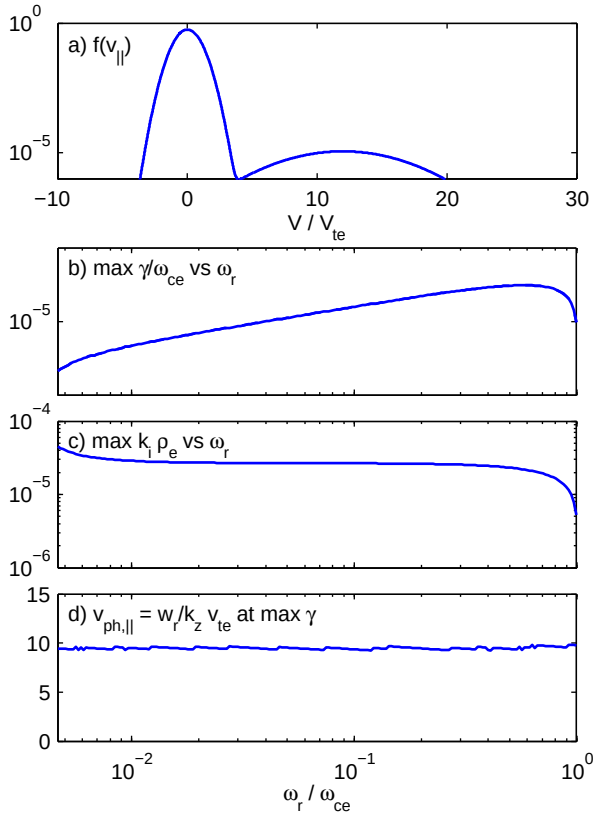

Figure 4-15: Calculated growth rate of Trivelpiece-Gould mode from Čerenkov instability. a) Model distribution with bump on tail. b) Growth rate of Trivelpiece-Gould modes versus ω_r. c) Max perpendicular convective growth rate $k_{\perp,i} = \gamma/V_{gr,\perp}$ versus ω_r d) Parallel phase velocity at maximum growth rate

regime is substantially lower ($\propto \omega$) than for modes near f_{ce}.

A potential resolution is to consider in more detail the transport of the generated waves using ray-tracing. These waves may be reflected from the low-density edge of the plasma and therefore confined, allowing for multiple passes of growth over regions of instability. Using the cold electrostatic dispersion, one can solve for $k_\perp$ for fixed $k_{||}$ and ω. (Simple ray tracing ideas imply that the latter two should be conserved as the waves propagate across the radial cross section: time scales for density evolution and magnetic field evolution are very long, and the parallel length scales are much larger than the perpendicular owing to toroidal symmetry and the strong guide field.) Then,

$$\left(1 - \frac{\omega_{pe}^2}{\omega^2 - \omega_{ce}^2}\right) k_\perp^2 = -\left(1 - \frac{\omega_{pe}^2}{\omega^2}\right) k_{||}^2. \tag{4.28}$$

From this one can show that $k_\perp$ is imaginary and the waves evanescent when ω_{pe}^2 falls below ω^2 (the $P = 0$ cutoff [76]). That is, the waves will be reflected back into the plasma from the low-density edge. For instance, at $f = f_{ce}/2$, the waves are reflected at the critical density $n_{cr} \approx 2 \times 10^{16}$ m^{-3}. This evanescence layer is well known from the study of lower-hybrid heating or current drive on fusion devices. In that case, it is an experimental complication because launched waves must tunnel through the evanescent layer near the antenna before being able to do useful work on the plasma. In the present case, however, the evanescent layer may confine the waves within the plasma.

4.4.3 Electromagnetic effects

Electromagnetic effects may be retained in the dispersion relation through solution of the full plasma conductivity tensor. In the VTF regime, for $\omega_{pe}^2 \gg \omega_{ce}^2$, the electrostatic Trivelpiece-Gould dispersion generalizes to the R-wave dispersion [76],

$$\omega = \omega_{ce} \frac{k_{||} k d_e^2}{1 + k^2 d_e^2}. \tag{4.29}$$

Here d_e is the electron inertial length or skin depth, c/ω_{pe}. This dispersion relation includes Trivelpiece-Gould modes in the limit $kd_e \gg 1$, so the skin-depth is seen to be the critical wavelength at where electromagnetic effects become important. In the opposite limit the electromagnetic whistler waves $\omega = \omega_{ce} k_{||} k d_e^2$ are recovered. (The boundary between

Trivelpiece-Gould modes and whistlers is relevant in other contexts, e.g. in the parametric instability of large amplitude plasma waves [94].)

Interestingly, one finds that the parallel phase-speed of R-modes has a maximum when $kd_e = 1$, at

$$\left.\frac{\omega}{k_{||}}\right|_{max} = \frac{1}{2}\frac{\omega_{ce}}{\omega_{pe}}c = V_{A,e}/2, \tag{4.30}$$

using the "electron-Alfvén" speed $V_{A,e} = (B^2/\mu_0 n m_e)^{1/2}$. This is quite close to our measured velocities: at a density 1×10^{18} m^{-3}, the maximum phase speed $V_{A,e}/2 \simeq 3.3 \times 10^7$ m/s. Alternatively, one could use the observed phase speed to bound the plasma density at $\lesssim 2.3 \times 10^{18}$ m^{-3}, which provides an interesting complement to the Langmuir probe and interferometer measurements.

Further, bearing on the problem of fast perpendicular wave transport of the electrostatic waves discussed above, it is found from the R-wave dispersion that $v_{gr,\perp}$ is identically zero at $kd_e = 1$. Further, $v_{gr,||} = v_{ph,||}$, so modes with this wave vector could stay confined to the plasma, and would propagate in resonance with the electron beams. The single allowed phase-velocity could also explain the high reproducibility of observed phase velocity from shot-to-shot. However, other measurements, discussed below, imply that the modes have $kd_e > 1$, in contradiction with this idea, as appealing as it may be for the reasons discussed.

Finally, at phase speeds below this maximum, two modes can be resonant with a given beam velocity, one a whistler whistler mode and the other a Trivelpiece-Gould. From Eq. 4.29, one finds,

$$\frac{\omega}{k_{||}} = V_{A,e}\frac{kd_e}{1 + k^2 d_e^2}, \tag{4.31}$$

and therefore for a given resonant phase velocity V_b there are two resonant branches, at $k = \omega_{ce}/2V_b \times [1 \pm (1 - 4V_b^2/V_{A,e}^2)^{1/2}]$. In the limit of well-separated roots, $V_b/V_{A,e} \ll 1$, these are the previously discussed Čerenkov root on the Trivelpiece-Gould wave, $k = \omega_{ce}/V_b$, and a new root due to instability of whistlers, $k = (V_b/V_{A,e}) \times (1/d_e)$.

We have compared the growth rates of the two branches by investigating beam-driven instability using the full plasma dispersion tensor. We have found, however, that the higher-frequency, Trivelpiece-Gould branch always has the larger growth rate. The result of this analysis is shown in Fig. 4-16, where instability is due to a cold beam with $V_b/V_{A,e} = 0.3$ (consistent with the observed phase velocity.) The high frequency peak cannot be explained by the whistler branch of the instability.

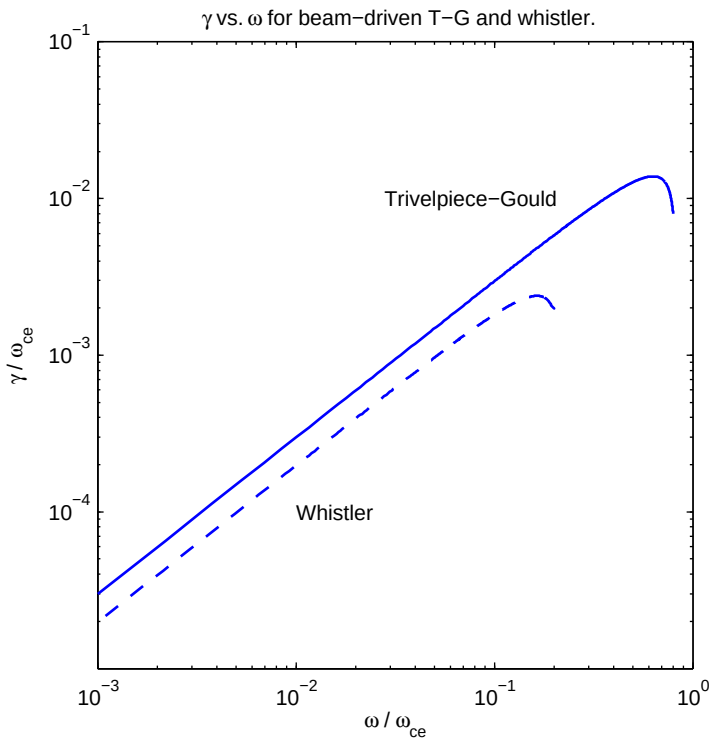

Figure 4-16: Comparison of the growth rates of whistler vs. Trivelpiece-Gould for beam-driven instability.

In order to conclusively discriminate between electromagnetic and electrostatic regimes one requires complete measurement of $|k|$. However, while $k_{||}$ is conclusively measured here, we really have only an estimate for $k_{\perp}$. Still, if one assumes electrostatic dispersion *a priori*, then $k = k_{||} \times (\omega_{ce}/\omega)$, which gives approximately constant $k \simeq 600$ m^{-1} over the whole band. This in combination with d_e of 5 mm at $n = 1 \times 10^{18}$ m^{-3} gives $kd_e \simeq 3$, consistent with electrostatic modes. This k measurement is also consistent with the estimate of $k_{\perp} \simeq 600$ m^{-1} over most of the range, since $\sin\theta = 0.86$ already at $\omega/\omega_{ce} = 1/2$. Finally, observed power in the spectra extends nearly to f_{ce}, while f_{max} for general R-waves will be $f_{ce} \times k^2 d_e^2/(1 + k^2 d_e^2)$, again implying electrostatic modes with $kd_e > 1$.

Overall, the high frequency modes are well understood as Trivelpiece-Gould modes (potentially including electromagnetic effects) driven by velocity space instability of high energy electrons. Simple growth rate calculations predict maximum growth near $f_{ce}/2$, based on the particular instability mechanism. The observation of approximately constant $\omega/k_{||}$ is consistent with Čerenkov drive by a positive slope in the distribution of high energy particles. In this case, the fluctuation observations are actually the first "diagnostic" available in

VTF to imply the existence of runaway electrons ($\mathcal{E} \simeq 1$ keV) produced by the reconnection events. Further proof is a high priority for future experiments.

4.5 Conclusions

We have presented study of electrostatic plasma fluctuations driven during magnetic reconnection events in the low-β, strong-guide magnetic field regime of VTF. The observation of spontaneous reconnection events is inherently interesting as it may help untangle the "trigger" mechanism governing transition from slow reconnection to fast reconnection in other systems. Further, the observed strong time dependence of reconnection rates in VTF is useful for experimentally determining which are the most important mechanisms enabling fast reconnection.

Here we have found strong fluctuations driven during the reconnection events. Modes are studied based on frequency spectra and with wavelength measurements using correlation analysis between multiple probe tips. We have found two broad regimes of modes, first, lower-hybrid modes which appear to be driven by perpendicular relative electron-ion drifts; an intriguing possibility here is the drifts due to perpendicular temperature gradients. (This may be inferred from the filamentation of the fast electrons discussed in the previous chapter.) These modes may also arise due to strong cross-field drifts related to the fast onset or non-axisymmetry of the reconnection events. The second regime is a broad collection of high-frequency modes, up to the electron cyclotron frequency, with fast, uniform phase velocity. The Trivelpiece-Gould modes appear to be driven by velocity-space instability of fast electrons energized by the reconnection events.

However, it has not established that these modes play an essential role in the reconnection process; there appear to be systematic time delays between reconnection events and peak fluctuation power, based on statistics over large number of discharges, and fluctuations persist after the reconnection events have ended. Naive estimates based on quasi-linear theory also do not support their having a large effect.

Chapter 5

Observation of Electron Phase-space Holes

The saturated state of instabilities in plasma is not always a broadband collection of weakly interacting waves. Instead, the instabilities can saturate by forming "coherent structures" in the plasma. This idea extends across plasma physics: for instance, at the edge of fusion devices, such as tokamaks, "filamentary structures," colloquially referred to as "blobs," are observed to be a dominant source of the particle transport. These structures form out of the nonlinear evolution of the drift-mode instabilities at the plasma edge.

Coherent structures can also form from current-driven turbulence. In this chapter we discuss observations of a type of coherent structure, "electron phase-space holes," within the turbulence driven during the reconnection events. Electron phase-space holes [95, 96], occasionally called BGK solitary structures (after the original paper by Bernstein, Greene, and Kruskal [95]), are the self-consistent plasma structures that form when a finite number of particles become trapped in large-amplitude plasma waves. They are well known, from simulations, to form out of bump-on-tail (or two-stream) instabilities when the instability saturates by trapping electrons.

Electron holes have received substantial attention in the space physics community due to a recent generation of spacecraft which has found them to be nearly ubiquitous in the space environment [97–99]. Most recently, they have been observed by spacecraft in conjunction with reconnection both at the Earth's bow-shock [100] and in the magnetotail [101]. They have also been found in reconnection simulations: Drake *et al.* [37] have found electron holes

resulting from electron-ion (Buneman) instability in reconnection simulations, and argued that they were an important source of anomalous resistivity which aided the reconnection process. The work here is the first laboratory study to find them emerge self-consistently from current-driven turbulence.

In this chapter, first the theory of electron holes is reviewed, including recent developments which are useful for the discussion here. We then present our experimental observations, including measurements of the size scale and propagation speed of the structures. The size scale and speed also indicates that the structures are electrostatic. These basic measurements and interpretation as electron holes have been recently published [47]. Finally, we present measurements of the correlation of hole observations with reconnection events and fast electrons, and discuss their potential effects on the reconnection process. However, their effects appear to be small at this point: the holes move too fast to efficiently couple electron and ion momentum and thereby provide anomalous resistivity; instead they likely work to rein in the tail of runaway electrons.

Appendix B discusses in greater detail the hole waveforms observed on the oscilloscope, and reconciles these with the earlier discussion of the RF Langmuir probe response (in Chapter 2). This last aspect provides a measure of calibration of the probe signals and indicates that the holes have peak potentials ϕ up to $k_B T_e/e$, in order of magnitude.

5.1 A review of electron holes

The story of electron holes begins with the theory of Bernstein, Greene, and Kruskal (BGK) [95], which describes nonlinear, exact stationary states of the Vlasov equation. This section will review the original BGK theory, pointing out the most important qualitative ingredients of their theory (and, therefore, electron holes). Later, Berk and collaborators showed that these structures appeared in simulations of the two-stream instability when the instability saturated by particle trapping [102]. The trapping of particles in plasma waves also has a role in the story of Landau-damping in plasma. The formation of a"BGK state"—where initial linear modes have evolved into an ensemble of these BGK structures—can saturate the collisionless damping process [103]. We then review recent theoretical progress and experimental observations, including those by the recent generation of spacecraft.

5.1.1 Basic electron hole theory

Electron holes are isolated positive-potential structures, consisting of a positive-potential spike which has trapped a population of electrons. The presence of trapped particles proves to be a necessary ingredient for the existence of the hole. Therefore, the minimum apparatus necessary is a *nonlinear*, *kinetic* theory. *Kinetic*, because the theory requires both passing and trapped particles, and thus we have to deal with velocity space, and *nonlinear*, because only a finite-sized wave can trap particles. BGK showed how to solve for the electron distribution, consisting of passing and trapped particles, which is self-consistent with a given electrostatic potential $\phi(x)$. Further, the solution is a steady state of the Vlasov-Poisson system, suggesting that the equilibrium can exist for a finite time in the plasma, i.e. it is not simply a clever superposition of waves that will immediately disperse. (Eventually, however, holes will be destroyed either by particle collisions, which will destroy the velocity-space structure, or by instabilities of the hole equilibrium.)

To construct a hole equilibrium, one starts with the 1-D Vlasov equation,

$$\frac{\partial f}{\partial t} + v\frac{\partial f}{\partial x} + \frac{e}{m}\frac{\partial \phi}{\partial x}\frac{\partial f}{\partial v} = 0. \tag{5.1}$$

Here f is the electron distribution function, $f = f(x, v, t)$, and ϕ is the electrostatic potential. (Here we will deal only with the electrons, for simplicity, regarding the ions as a neutralizing background). f is assumed to reach a uniform $f_\infty(v)$ at $x = \pm\infty$, where ϕ is assumed to go to zero. Steady-state solutions, $f = f(x, v)$, are naturally found by demanding $f = f(\mathcal{E})$, where $\mathcal{E} = mv^2/2 - e\phi$ is the energy. f will then acquire its spatial dependence through its dependence on ϕ. The case $\phi < 0$ is not so interesting; that forms a potential hill for the electrons, to which they have a Boltzmann response. Regions where $\phi > 0$ (i.e. inside the positive potential of an electron hole) *are* interesting, for here there are "bound states" with $\mathcal{E} < 0$. Electrons with $\mathcal{E} < 0$ are trapped in the potential of the hole, and they are critical for the construction of holes.

The next step is to demand that the distribution f be self-consistent with the Poisson equation for the electric field:

$$-\nabla^2\phi = \frac{n_0 e}{\epsilon_0}\left(1 - \int f dv\right)$$

$$= \frac{n_0 e}{\epsilon_0}\left(1 - \int_{-e\phi}^{\infty} \frac{f d\mathcal{E}}{\sqrt{\frac{2}{m}(\mathcal{E}+e\phi)}}\right). \tag{5.2}$$

Here, n_0 is the equilibrium density, and the first "1" in parenthesis is due to the neutralizing ion background. There are two ways to view this equation; first, as a differential equation for ϕ, given f, or second, as an integral equation for f, given ϕ. BGK focused mostly on the second. To this end, it is useful to split up the integral over f into two pieces, first from $-e\phi$ to 0, and then from 0 to ∞, i.e. into integrals of the trapped and passing pieces of f, which we will call f_t and f_p. f_p is in principle known since it is just the distribution in the ambient plasma. BGK found a way to invert Eq. 5.2 to solve for f_t given f_p and ϕ. (For further details see Ref. [95]). They thus found that essentially arbitrarily shaped pulses could be supported by an appropriately chosen f_t.

Before proceeding further, it is useful to make a few more observations. Figure 5-1 shows a cartoon of how the BGK solution works. Starting in the top-left, a positive potential spike ϕ is assumed. Moving counterclockwise on the figure, particle orbits in the potential $-e\phi$ are calculated, which includes passing particles and trapped particles. Next, we calculate the density of trapped or passing particles. Note in particular that the density of passing particles inside the potential peak is *less* than in the ambient plasma. Physically, the passing particles speed up as they fall into the potential well $-e\phi$ (because we have 1-D particle orbit dynamics, as is imposed by an infinite magnetic field). As they speed up, their density drops due to continuity. One can see that this is also contained in Eq. 5.2: the integral of f over the untrapped portion ($\mathcal{E} > 0$) is clearly a *decreasing* function of ϕ owing to ϕ in the denominator. The trapped electrons, on the other hand, can balance this effect, since they contribute a positive electron density. Finally, we move to the top right, where we sum the trapped and passing electron densities to find the final density perturbation. This density perturbation must be consistent with the initial potential via the Poisson equation. Here it becomes clear why trapped particles are necessary: for a simple, monopolar ϕ as shown in the top-left, the associated electron density perturbation ($\propto \nabla^2\phi$) has an inverted "Mexican-hat" shape with a negative core, but positive wings. The trapped electrons are necessary to contribute this positive density on the wings.

Note that, despite the presence of the trapped electrons, positive potential spikes have an overall net positive charge, a net *depletion* of electrons. Most importantly, typically an

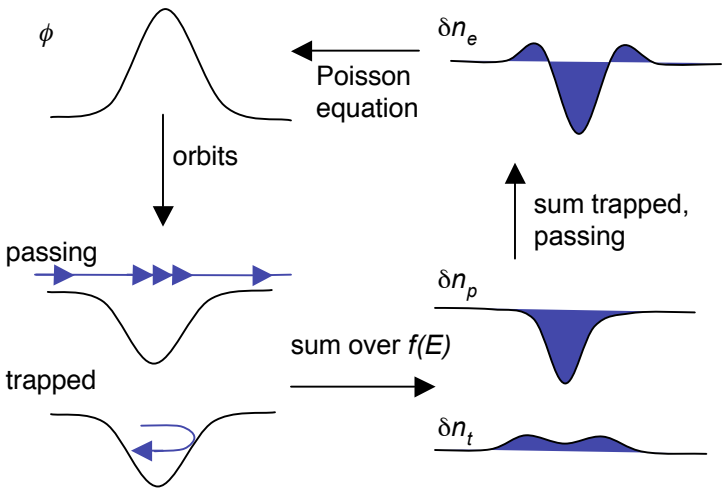

Figure 5-1: Schematic of how a self-consistent electron hole equilibrium works. Orbits are calculated in the potential well $-e\phi$, and consist of trapped and untrapped electrons; the latter connect to a known distribution at ∞. Trapped and untrapped density perturbations are calculated. These are summed to give the total perturbed density, which must be consistent with the initial ϕ via the Poisson equation.

area of phase space (for x within the potential spike, and near $v = 0$—corresponding to the most-deeply-trapped orbits) will have drastically less phase-space-density than for $v = 0$ in the ambient plasma (which is at the peak of the Maxwellian), and therefore appears as a hole or vortex in (x, v) phase. Hence the moniker "electron hole".

An essential question left out by BGK was where such structures can come from. Indeed, this may all have remained a theoretical curiosity, had they not been observed in simulations of the two-stream instability conducted by Berk and collaborators [102, 104]. These were some of the first simulations of the two-stream instability, and were conducted more than 40 years ago. By today's standards, these simulations are quite crude: they took the electron distribution $f(x, v)$ as having only two values, 1 and 0, i.e. electrons present or not. The utility of such a "water-bag" model is that only the boundary needs to be followed, which substantially reduces computational requirements. Despite this crude model, their numerical experiments showed qualitatively the emergence of coherent structures in the turbulence, which they connected to the BGK theory. The instability had grown fast enough to trap particles in the trough of the wave. Interestingly, they also found that primordial holes, which appear once per wavelength out of the initial unstable perturbation, quickly merge or coalesce into larger structures. They found, in fact, that holes are attracted to

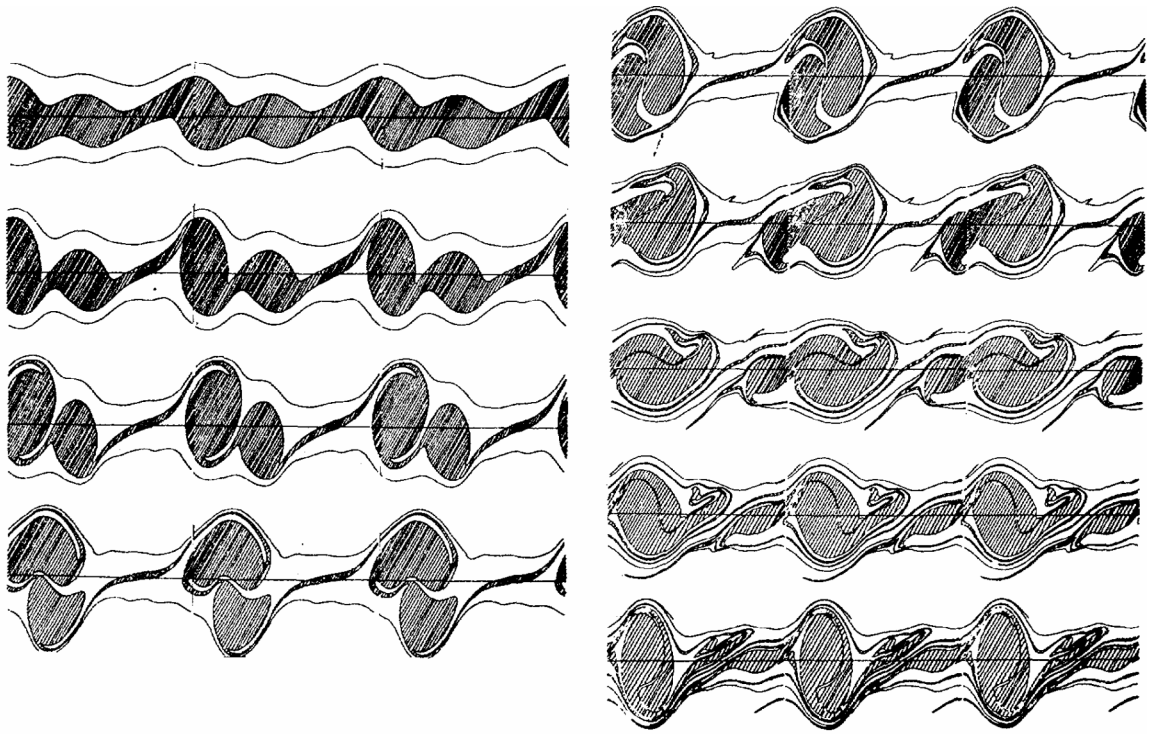

Figure 5-2: Results from an early simulation of the two-stream instability showing electron phase-space hole growth and coalescence into larger hole structures. Shown is (x, v) phase space with position along the x-axis and velocity along the y, and frames are sequential time slices. The shaded black portion indicates where $f = 0$ and is the area of phase space separating the two counter-streaming beams, which have $f = 1$. The other boundary of the beams, at large $|v|$, where f returns to 0, is shown with a simple black line. After Roberts and Berk [102, 104].

one another, which they attributed to a "negative-mass" instability—that is, the holes had net positive charge (as described above), but a net negative mass (based on the depletion of electrons), and therefore would attract one another. Figure 5-2 shows a figure from Roberts and Berk [102] showing the initial growth and then coalescence of electron holes.

Described above is essentially the "minimum physics" of electron holes: nonlinear, electrostatic, kinetic structures that are steady states of the Vlasov equation, the trapping of a population of electrons in the wave trough, and their growth from strong two-stream instabilities. More physics has been incorporated since then, which is discussed below. Some simple extensions include constructing holes which travel at finite speed (one simply transforms into the hole frame, then allows the passing distributions to depend additionally on whether they connect to $x = +\infty$ or $-\infty$.) More challenging has been generalizing

hole theories to 3-D shapes (as will be necessary to describe the holes observed in VTF), and generalizing to finite magnetic field. (The theory above has used strictly 1-D electron dynamics, which is obtained when $B \to \infty$.)

5.1.2 Subsequent theoretical progress

The BGK theory allows for a nearly unlimited set of potential shapes to be realized. This is due to the substantial freedom allowed by being able to choose f_t; really the only constraint within the BGK theory is that $f_t \geq 0$. This is in notable contrast to other types of nonlinear solitary wave theories, such as Korteweg-de Vries (KdV) soliton theory [105]. (KdV is a paradigm theory for large-amplitude, nonlinear solitary waves, or "solitons."*) For KdV solitons, one can derive one-to-one relations between the structure's velocity, amplitude, and spatial width; those solitons have just one free parameter, e.g. the amplitude.

In the BGK theory there is substantially larger latitude for generating structures of different speed, amplitude, width, etc, because of the freedom for choosing f_t. However, there has been some controversy since the original paper as to whether these states are all physical. In particular, BGK theory allows some singular types of distributions: f_t is not required to be continuous. However, because particle collisions are a diffusive process, they can act very effectively on sharp, singular velocity-space structure. Therefore it is not necessarily physical to let f_t be chosen arbitrarily.

This does not destroy the concept of electron holes, however, it merely restricts the space of shapes that can be realized. Schamel (for a review see Ref. [96]) raised this criticism and devised a complementary technique to make progress on this problem. The main ingredients of the holes remained: nonlinear potentials and trapped electrons, but instead of solving for f_t, Schamel began with a specified distribution, including a specified trapped population, and solved for the self-consistent ϕ via the "pseudo-potential technique." Notably, he was still able to find solitary wave solutions. Some interesting results from Schamel were that he found a velocity limit for electron holes of 0.9 v_{te} ($v_{te} = \sqrt{2k_B T_e/m_e}$). Second, he found that, in the small-amplitude limit, the hole structure has a $\mathrm{sech}^4(\cdot)$ shape.

A recent extension to Schamel is the work of Goldman *et al* [106], who similarly required *a priori* to have physical, continuous distribution functions—most importantly continuity

*Of historical note, M. Kruskal is a co-author on both of these solitary wave papers: first BGK's 1957 paper on electron holes [95], and then the landmark Zabusky-Kruskal 1965 paper on KdV solitons [105].

across the trapped-passing boundary. They were able to proceed from the outset in a small (though nonlinear) amplitude limit, and found a few notable results, the first is a relation between the spatial width and speed of the hole, with the hole becoming wide as the speed approaches Schamel's limit. Second, the amplitude and width are independent; the amplitude is essentially a free parameter determined by the "depth" of trapping, i.e. the number of trapped particles. In conclusion, restrictions to the original BGK theory, based on demanding well-behaved, smooth trapped-particle distributions, reduce the space of allowed hole shapes but still leave a larger dimensioned space than, for example, KdV soliton theories.

Complementary theoretical progress has been made on other aspects of electron holes. That which is most relevant for the experimental work reported here are the extensions electron hole theory to greater than one-dimension. The theories above describe 1-D electron holes, i.e. $\phi = \phi(x)$ only, so they are really like sheets of charge. This theoretical work has been driven by space observations of electron holes, which often find holes with 3-D structure.

There are two aspects to this problem. First is the generalization to 3-D hole shapes; this proves to be fairly straightforward as long as the magnetic field is very strong. In that case, the electrons will still have 1-D dynamics, with infinitesimal gyroradius, and behave like beads on a wire. This proves essential, since the electron hole equilibrium requires that the passing electrons, upon entering the hole, speed *up* so that their density can *decrease* (see Fig. 5-1). In higher dimensions, this is not the case: positive potentials will lead to *increased* electron density, which contradicts the charge structure necessary to maintain the hole equilibrium. This issue has been discussed by a few authors, for example Ng and Bhattachargee [107, 108], who provide essentially a proof of this fact: 3-D holes with unmagnetized electrons do not exist.

Provided that magnetized electron dynamics are maintained, it does appear possible to construct 3-D holes. The earliest computational work on this front was undertaken by Saeki and collaborators [109, 110], who also made the original experimental observation of electron holes (discussed further below). In their experiment, holes were launched down a narrow plasma discharge tube, which set a tight perpendicular boundary condition $\phi = 0$ at the chamber wall. Because the tube width turned out to be approximately the same as the parallel hole size, it was an important effect, and this boundary condition was included in

their modeling. Schamel [96] reviews analytic and semi-analytic work on holes in bounded plasmas.

Spacecraft observations also typically find 3-D holes (see Fig. 5-3 below). This has driven further theoretical hole modeling, mostly attempts to find 3-D BGK-like equilibria. Some notable contributions here come from Chen [111, 112] who derived a width-amplitude inequality based on a BGK construction of 3-D, axially-symmetric electron holes [i.e. $\phi = \phi(r, z)$]. Chen has shown that this is straightforward as the problem factors into basically independent 1-D Vlasov equations (in the z-direction). The conclusion that emerges from these investigations is that 3-D holes can exist, provided that the electrons can maintain 1-D, magnetized orbits. Other Vlasov modeling of 3-D hole structures has been discussed by Muschietti [113].

Extension to finite magnetic fields has proven more difficult. The first problematic effect that appears as the magnetic field decreases is the electron-polarization drift, which draws electrons *across* the magnetic field toward the potential peak of the hole. Such drifts can certainly be understood to destroy holes, since they are the first step toward completely demagnetizing the electrons (which was argued above to thwart hole equilibrium). The polarization drift also complicates theoretical modeling, and the criteria that have been proposed for existence of holes in finite fields are not much more detailed than "the polarization drift can be ignored." (see, e.g. Ref. [111]). This condition is fulfilled when the holes are many gyro-radii wide, and this therefore appears to be a requirement for 3-D holes in finite magnetic fields. However, apparently little progress has been made beyond these intuitive first steps; a satisfactorily complete modeling of finite-magnetic field holes (using gyrokinetic theory, for example) appears to be lacking.

Finally, since Berk and collaborators' pioneering work, simulations have made substantial progress studying electron hole formation and dynamics. Most of the progress has appeared recently, driven by the discovery of electron holes in the space environment by spacecraft in the mid-1990's. Some of the main questions that have been tackled since then are the dynamics and stability of holes in higher dimensions. Goldman, Newman, Oppenheim, and collaborators, in a series of papers in the late 1990's, studied hole formation using large-scale particle-in-cell (PIC) simulations, and found that initial "phase-space tubes" decayed due to perpendicular instabilities, getting chopped up into 3-dimensional structures [114, 115]. Other work [116] has also studied the stability of holes in weak

magnetic fields, finding that holes must be multiple gyroradii in diameter for *stability*, in addition to equilibrium as discussed above. However, very few simulations have been carried out in the magnetic field regime matching VTF, where $\omega_{pe} \gg \omega_{ce}$.

5.1.3 Experimental electron hole observations

The recent generation of satellites has opened new doors in the observation of plasma fluctuations. One surprise from this has been the observation of spiky, bipolar electric field structures in many space environments; in many instances these have been identified as electron phase space holes. Spacecraft observe the electric fields associated with the holes, rather than potential, and therefore see a *bipolar* electric field pulse. Apparently, satellites have been encountering these structures for a long time, but only since the mid 1990's has the data acquisition rate on the satellites been fast enough to resolve the spikes. Previously, sample rates were not sufficient to fill out the structure, and the fast spikes appeared simply as a series of random points. Not knowing the source of this randomness, the phenomenon was given the name "Broadband electrostatic noise," or BEN.

However, in 1994, analyzing data from the GEOTAIL spacecraft, Matsumoto *et al* [97], first recognized that BEN actually consisted of bipolar electrostatic structures. Matsumoto *et al* also advanced the idea that these "electrostatic solitary waves," as they termed them, were electron holes resulting from strong two-stream instabilities. Here, a collaboration with computer simulations by Miyake *et al* [117] helped to show how the holes could be generated from a bump-on-tail instability.

Since the GEOTAIL satellite's observation of holes in the deep magnetotail (near $70R_E$), coherent electrostatic structures have been observed in many other parts of the magnetosphere, including the polar auroral zone by the FAST satellite [98, 118], the high-altitude polar magnetosphere by the POLAR spacecraft [119], and the earth bow-shock by the Wind spacecraft [99]. Figure 5-3 shows typical bipolar electric field data measured by POLAR. These have been conclusively identified as positive-potential structures and more specifically as electron holes.

In addition, numerical and analytic work has also advanced the connection between the observed bipolar pulses and electron holes. Most recently, Goldman *et al* [106] have shown that individual bipolar electric field waveforms from the POLAR spacecraft data [120] can be fit well by their small-amplitude electron hole theory described above. Connections

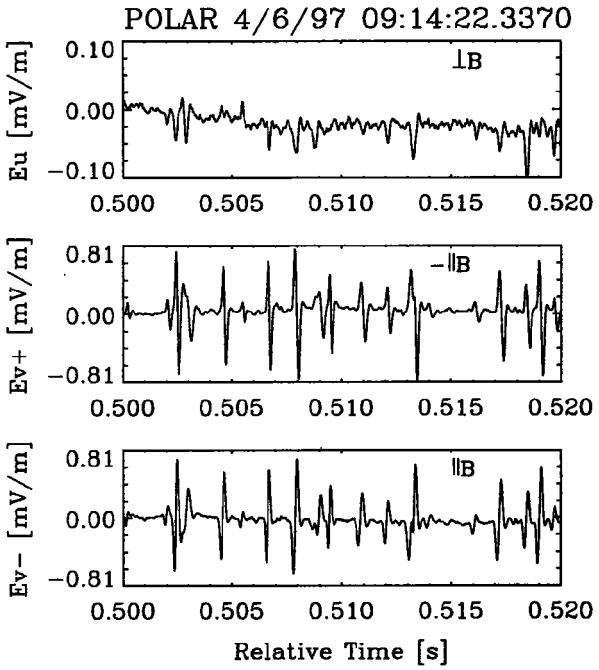

Figure 5-3: Bipolar field structures, which have been identified as electron phase-space holes, as observed by the POLAR spacecraft. E_{v+} and E_{v-} are a pair of oppositely pointing antennas that measure the component of the electric field along the magnetic field. They observe (oppositely-directed) bipolar pulses, and time delays from one to the other can also measure the velocity of the structures. E_u is a perpendicular antenna, which measures the electric field perpendicular to the magnetic field. The unipolar shape is consistent with 3-D electron hole structures crossing the satellite "off-axis." After Franz, 1998 [119].

between spacecraft observations and our own measurements will be made in the discussion section below.

Spacecraft have also now observed electron holes in association with magnetic reconnection. Matsumoto *et al* [100] have observed electron holes during reconnection on the day-side of the earth, and Cattell and collaborators [101] have now also found electron holes associated with magnetotail reconnection. Drake *et al* [37] have also found electron holes in reconnection simulations. These holes arose out of an electron-ion (Buneman) two-stream instability, and were argued to be an important source of anomalous resistivity, speeding the reconnection process in the simulation. The connections between Drake's and our results will be discussed below in Section 5.3. Oppenheim and Dyrud [121] have also studied the anomalous resistivity produced by electron holes.

In laboratory studies of electron holes, Saeki and collaborators [109] made the first controlled study of electron hole equilibria and dynamics. They studied hole propagation down a narrow discharge tube (only a few Debye lengths in diameter), filled with a low-density, Q-machine plasma. Electron holes were directly launched down the plasma by applying a large voltage between sections of the tube boundary. This had the effect of launching both a fast soliton and an electron hole down the discharge tube. (The soliton was a identified as a classical, Korteweg-deVries (KdV) type soliton, whose physics entails the nonlinear extension of the Trivelpiece-Gould mode. It relies on the nonlinearity associated with how electrons bunch in response to a large-amplitude, fast disturbance. It could be distinguished from the electron hole because it had a different polarity, $e\phi < 0$, consistent with bunching of electrons rather than depletion, and it moved faster.) Notably, this group was also able to observe [110, 122] some of the same dynamics seen by Berk *et al* in their numerical simulations (Fig. 5-2), namely the coalescence of two electron holes when one overtook the other. In these experiments, the parallel size of the holes was found to be 15-20 λ_D, and the boundary was an important effect, since the chamber was only a few Debye lengths wide. The 3-D hole shape was therefore set by the boundary, and this effect was included in computer modeling of the experiment.

More recently, Moody and Driscoll [123] have applied similar techniques as Saeki *et al* and found both holes and solitons in non-neutral plasma. The trapping of particles in plasma waves also plays a role in a number of experiments studying the long-time evolution and saturation of Landau damping: the formation of a "BGK-state" of non-damped hole

structures was observed recently by Danielson *et al*[124]. The creation of these BGK-type structures has also been invoked to explain the saturation of Landau-damping in laser-plasma interactions relevant to inertial-confinement fusion [125]. The trapping of electrons in a wave trough has also been studied in detail in recent experiments where an electron beam and a seed wave (near f_{pe}) were simultaneously launched from one end of a chamber [126].

However, no experiment has studied the self-consistent creation of electron holes from current-driven turbulence (i.e. without the use of test waves or direct launch by biasing the boundary). While Langmuir turbulence has been studied for decades, digital oscilloscopes with high bandwidth and digitization rates (> 1 GHz) and long record lengths (~ 1 MSample) have only recently come on the market. This allows direct, time-domain study of fast plasma turbulence. In contrast, previous experiments on Langmuir turbulence relied on frequency domain techniques, e.g. down-mixing of Langmuir probe signals or microwave scattering [127]. In the time domain, an electron hole is a simple, positive-potential spike. However, in the frequency domain, not only does it occupy large bandwidth (from near DC out to the inverse of the hole width), but, crucially, the individual Fourier harmonics are *not* statistically independent. Instead, the phase between the harmonics is fixed so that they can sum to be a delta-function-like signal.

5.2 Spike observations

In addition to the broadband turbulence presented in the previous chapter, it is often seen that the fluctuations during the reconnection events are highly spiky. Figure 5-4 shows the typical time traces of (a) plasma current and (b) toroidal reconnection electric field, and fluctuations (c) showing asymmetric, spiky turbulence. Some individual spikes are visible in Fig. 5-4(d), which zooms in on the 8 μs time period with spiky turbulence. The presence of such spikes is highly interesting; it implies that the turbulence is not simply a broadband collection of waves, but that the turbulence contains coherent structures.

The spikes also are apparent in aggregate measures of the fluctuations: for example, Figure 5-4(e) shows the distribution (pdf) of voltages measured by the probe over this time window, which is skewed and has a positive tail of outliers. The outliers are the spikes. In contrast, if the turbulence was simply a broadband collection of uncorrelated waves,

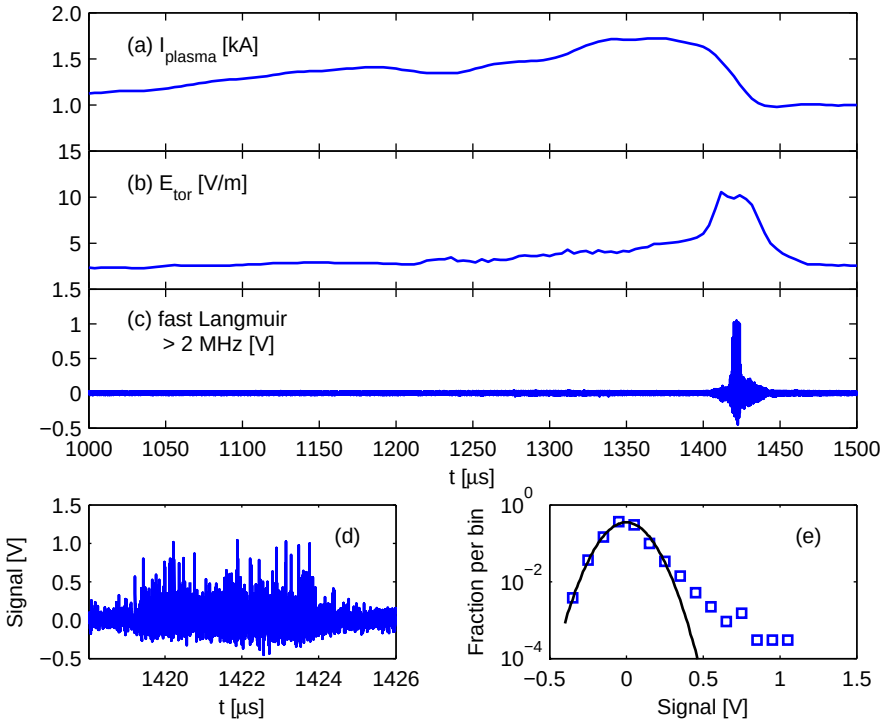

Figure 5-4: An overview of the presence of spiky turbulence seen during reconnection events. (a) Plasma current, showing a sharp drop near 1400 μs from a reconnection event. (b) Associated toroidal, reconnection electric field, showing the associated inductive spike during the reconnection event. (c) Fluctuations observed by a fast Langmuir probe. (d) Zooms in on the time window where positive spikes are evident. (e) Log-histogram of probe voltage measurements over this time window, showing a skewed distribution due to the presence of spikes.

then the distribution of voltage measurements would simply be gaussian. The presence of skewed fluctuation distributions is a common feature of turbulence that includes coherent structures. These spikes are also noticeable simply because they are the largest-amplitude fluctuations seen by Langmuir probes. While typical periods of strong *broadband* fluctuations yield peak (raw) fluctuation amplitudes of around 200 mV, spikes up to 1.5 V have been seen.

This section will describe the initial measurements of spiky turbulence driven during the reconnection events. Individual spikes are studied, and we present measurements of their parallel and perpendicular sizes and propagation speed. Overall, the spikes have been observed with nearly all combinations of fast Langmuir probe (see Figs. 2-8 and 2-9) and oscilloscope. The original measurements of the key properties of the spikes was accomplished with the 60-μm probe array (Fig. 2-8) and a Tektronix 7254 oscilloscope (2.5 GHz bandwidth, 5 GHz sampling). The high bandwidth proves crucial, as the spike waveforms are only about 400 ps wide. This section will mostly describe measurements made in this configuration, however we will include velocity measurements made using using the flexible 300-μm probe array in combination with a Tektronix 72004 oscilloscope (16 GHz bandwidth, 12.5 GHz sampling). Further measurements using this combination appear in Appendix B.2, which discusses some of the finer points of the spike waveforms and their relation to the high-frequency Langmuir probe response.

Figure 5-5(a) shows a short, 10 ns time window of fluctuation measurements during a period of spiky turbulence. The window shown contains two spikes; the blue and green traces are on two separate probes, separated by 4.6 mm in the toroidal direction. The data points, sampled at 5 GS/s, appear as open symbols. Notably, the spikes are well-correlated between the two probe tips, but with a time delay (here about 1.2 ns). Other tests with the probes separated perpendicular to the magnetic field, shown in Fig. 5-5(b), show zero time delay. Therefore, the spikes appear to travel *along* the magnetic field at a finite speed. The excellent correlation arises because the two probe tips see the *same* spike as it passes them by. Furthermore, in Fig 5-5(a), the green trace (square symbols) is from the "upstream" probe—upstream in terms of the electron flow inferred from the total plasma current—indicating that the spikes travel along the magnetic field *with* the electron flow.

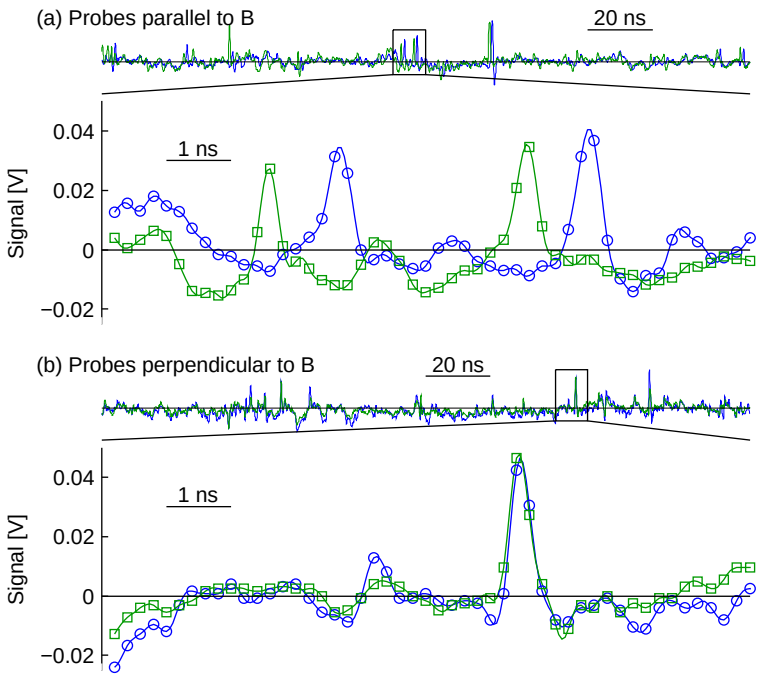

Figure 5-5: Time traces of spikes moving past a pair of fast Langmuir probes, over 100 ns and then zoomed-in on a 10 ns interval. In (a), the probes are separated by 4.6 mm parallel to the magnetic field. In (b), the probes are separated by 0.8 mm perpendicular to the field.

5.2.1 Speed and parallel size

Next, the propagation speed of the spikes is measured from time delays between spikes events on two probe tips. The histogram in Fig. 5-6(a) shows the distribution of measured delays for all spikes observed during this discharge; the typical delay between the two probes is about 1.1 ns. Based on the 4.6 mm probe separation, we find that the spikes travel approximately 4×10^6 m/s. In plasma units this is approximately 1.5–2 v_{te}, where $v_{te} = \sqrt{2kT_e/m_e}$ has been evaluated using the typical temperature of 15 eV. Similar measurements have been repeated with the Tektronix 72004 oscilloscope. An example is shown in Fig. 5-6(b), where we find a roughly similar, supersonic speed of 5.5×10^6 m/s.

Next, the parallel size of the spikes (parallel to $\mathbf{B}$) is estimated based on the inferred speed and the temporal width of the trace. The spikes from Fig. 5-5 have full-width-half-maximum (fwhm) temporal widths of about 500 ps. Figure 5-7 shows the statistics of the parallel widths measured for all spikes found during this discharge; the typical temporal width is about 400 ps. Combining this typical width and the spike velocity, we infer a typical parallel diameter of 1.5 mm. In plasma units, this is 8 gyroradii ($\rho_e = v_{te}/\omega_{ce} \approx$

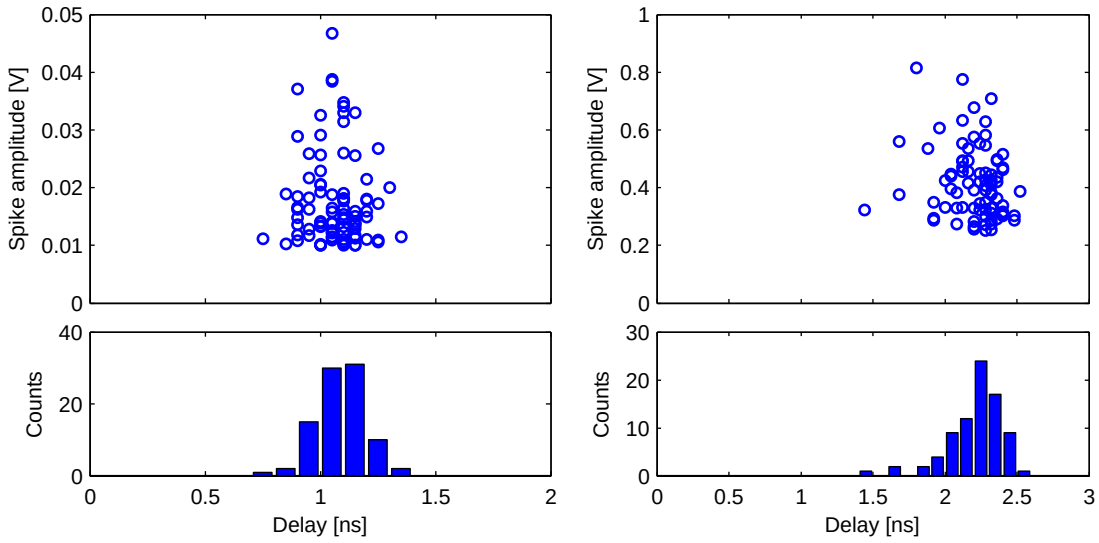

Figure 5-6: Probe-probe delays determine the parallel propagation speed of the spikes. (a) Measurements with the Tektronix 7254 scope and 60-μm probes, with probe separation of 4.6 mm. Inferred speed = 4.6 mm/1.1 ns = 4 $\times$ 10^6 m/s. (b) Measurements with the Tektronix 72004 scope and 300-μm probes, with probe separation of 1.3 cm. Inferred speed = 1.3 cm/2.3 ns = 5.5 $\times$ 10^6 m/s.

200 μm). Alternatively, this is about 60 Debye lengths ($\lambda_D = \sqrt{\epsilon_0 kT_e/ne^2} \approx 25$ μm).

A short note here on measurement accuracy and systematic effects: while the spikes are observed to be much larger than the probe diameter, and thus well resolved by the physical probe, the finite rise-time of the scope (Tektronix 7254) used for these measurements will widen the spikes somewhat. This aspect fits in with a longer story of plasma-probe coupling which is discussed in Appendix B.2. Even accounting for these systematic details, there is large residual scatter due to an apparently heterogeneous mixture of spikes, and it is difficult to measure the width of these structures in the presence of other turbulent fluctuations in the plasma. For now, it is best to understand the measurements as *typical* scale sizes; this has proved adequate for establishing the essential physics of these structures.

5.2.2 Perpendicular size

The perpendicular size of the spikes is measured by experiments with the probe tips separated perpendicular to the magnetic field. Figure 5-8 shows histograms comparing signals observed by pairs of probes at zero time delay. Integrating in the vertical or horizontal directions on any plot gives the single-probe histograms, which are shown in log scale exactly

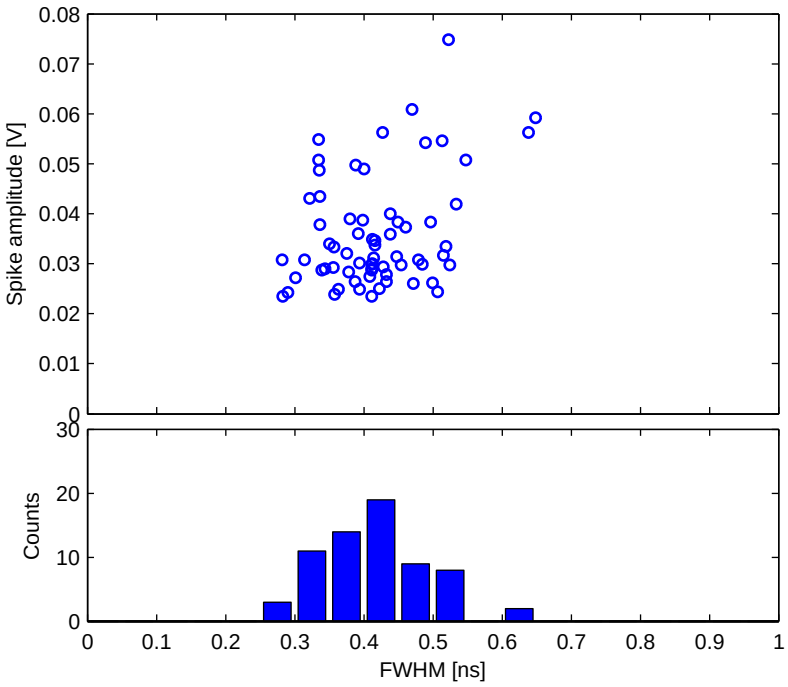

Figure 5-7: Measurement of the spike parallel size from time width (fwhm) of spike traces.

as in Fig. 5-4(e). As noted before, the tail of outliers on the scatter plots and log-histograms (where the log-histograms deviate from being parabolic) are the spikes. As is readily visible from the plots, the spikes (outliers) at $\Delta = 0.8$ mm (top-left) are highly correlated, implying the spikes must be typically larger than 0.8 mm. The same exercise can be repeated for increasing probe separations. Of note, at $\Delta = 4.6$ mm (bottom-right), there is essentially no correlation between the outliers. These measurements thus bracket the typical perpendicular size of the spikes, which we take as 2 mm. As this is similar to the parallel size, the spikes are approximately spherical.

5.2.3 The spikes are electrostatic

From the measurements made thus far, it is possible to show that the spikes observed are *electrostatic* phenomena. This should not come as a surprise, as the last chapter found that electrostatic waves were the *linear* modes most-easily driven unstably in the low-β, VTF plasma. Since it seems likely that the spikes could emerge in the nonlinear phase of those earlier, linear instabilities, we might expect them to also be electrostatic. However, here we present argument based only on the spike observations and physical scaling arguments.

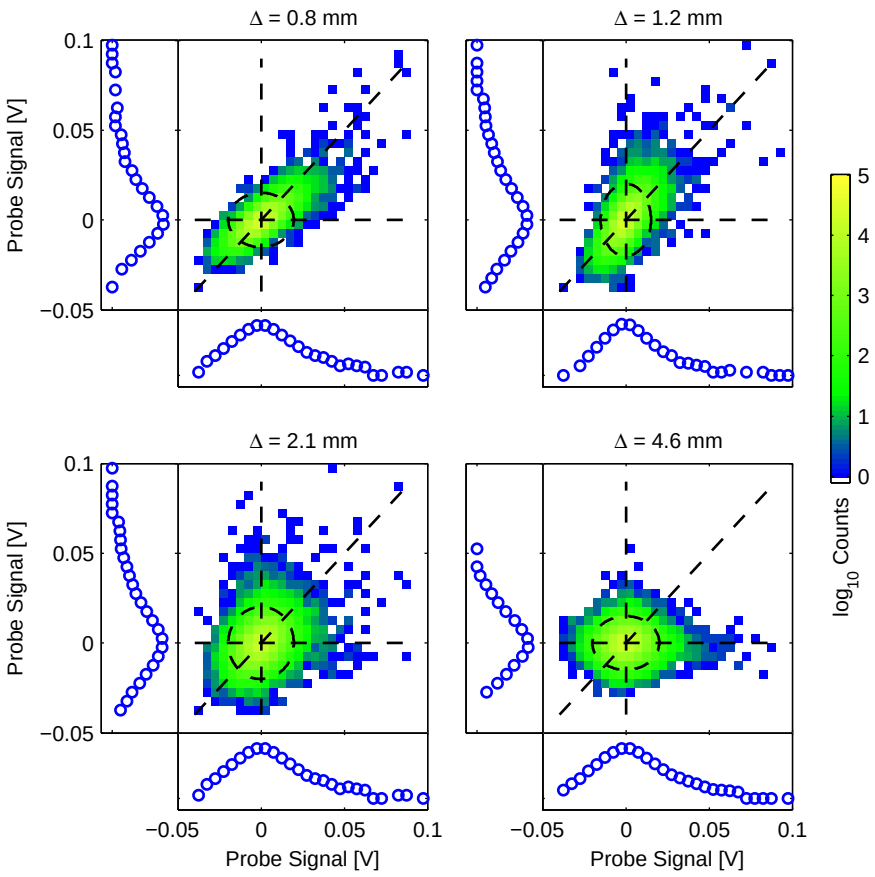

Figure 5-8: Spike perpendicular size inferred from perpendicular correlation. Probe-probe correlation histograms, and corresponding single-probe log-histograms, at zero time delay. The probe separations range from 0.8 mm to 4.6 mm perpendicular to the magnetic field. Excellent correlation is seen at 0.8 mm separation, and none at 5 mm, bracketing the perpendicular size at about 2 mm.

Electrostatic and electromagnetic wave phenomena in plasmas are distinguished by the dominant physics for generating the electric fields associated with the wave [76]. For electrostatic waves, the dominant plasma response is to be bunched by the electric fields, and to therefore create electric fields via a small amount of charge separation. For low-frequency, electromagnetic waves, the dominant plasma response is electric *currents*, which then accounts for the wave electric fields by induction. (Finally, there are also high-frequency electromagnetic waves—those that resort to being standard electromagnetic (light) waves in vacuum—for which the electric fields are generated predominantly by induction though the Maxwell displacement current.)

Following standard procedure, combining Ampere's and Faraday's laws, an electric field associated with a wave will satisfy

$$\nabla \times \nabla \times \mathbf{E} = -\mu_0 \frac{\partial \mathbf{j}}{\partial t} + \frac{1}{c^2} \frac{\partial^2 \mathbf{E}}{\partial t^2}. \tag{5.3}$$

This equation will contain both electrostatic and electromagnetic branches of solutions. The condition for an electrostatic wave is $\mathbf{E} = -\nabla\phi$. Inserting this into the above equation, the left hand side is *zero*. This can only arise when the individual terms of the LHS are *large and canceling*; therefore, the condition for a wave to be electrostatic is that

$$\left| \frac{\omega^2}{c^2} \right| |E|, |\mu_0 \omega j| \ll |k^2||E|. \tag{5.4}$$

Physically, the currents associated with an electrostatic disturbance are not sufficient to account for the electric fields by induction.

To complete this analysis, one must estimate what currents can arise in the plasma in the relevant parameter range to verify that they are small. For the case of the present spike observations, this question is important to answer as it strongly suggests the sort of theory that we should pursue. In the following, we present a scaling analysis based on observed size and speed which shows that the holes are electrostatic.

Here, we will replace k with $1/L$, where L is the characteristic size of the spike. We have shown this to be 1–2 mm, or about 5–10 ρ_e. Similarly, we will replace ω with $1/\tau$, where τ is the time for the spike to go past a volume element of plasma. τ and L are related by the hole speed $V = L/\tau$. Recall that we have found V to be of the order of a few times v_{te}. The analysis is further simplified since we have found that these spikes have roughly unity

aspect ratio, so there is only one length scale in the problem.

What remains is to estimate typical sizes of terms on the right-hand-side of Eq. 5.3. First, the Maxwell displacement current term can be seen to be small if $L^2/\tau^2 = V^2 \ll c^2$. This is well satisfied, since the observed spikes move well below the speed of light, $V/c \sim 1/50$.

Next, we estimate sizes of various currents j on the right hand side. One of the most important of these is the $E \times B$ motion of the electrons in the positive potential of the spike; this carries electrons azimuthally around the spike. This effect gives a current neE/B, which is small if $\mu_0 L^2 ne/\tau B \ll 1$. This simplifies to the condition $(V/v_{Ae})(L/d_e) \ll 1$, where v_{Ae} is the so-called *electron* Alfvén speed $v_{Ae}^2 = B^2/\mu_0 n m_e$, and d_e is the electron skin depth, $d_e = c/\omega_{pe}$. Current also arises from the electron polarization drift, but this is smaller than the $E \times B$ current, so will also be negligible under the same circumstances.

Finally, we can estimate the parallel currents that arise from parallel kicks to the electrons from the hole electric fields. From the electron parallel momentum equation, this is estimated to be $\Delta v \simeq eE\tau/m_e$, giving a current $ne^2\tau/m_e$. This will be negligible if $L^2/d_e^2 \ll 1$.

In summary, we are left with two requirements for holes to be electrostatic: $(L/d_e)(V/v_{Ae}) \ll 1$, and $L^2/d_e^2 \ll 1$. The condition (V/v_{Ae}) is well-satisfied in VTF because of the large guide field and small plasma β, since we have shown $V \simeq 2v_{te}$, and $v_{te}^2/v_{Ae}^2 = \beta \sim 10^{-3}$. Finally, $L^2/d_e^2 \ll 1$ follows because $d_e \simeq 5$ mm at $n \simeq 10^{18}$ m^{-3}, so $L^2/d_e^2 \simeq 0.1$.

Finally, we can connect this back to our earlier linear wave theory: the condition $L^2/d_e^2 \ll 1$ is analogous to the electrostatic condition $k^2 d_e^2 \gg 1$, which separates the electrostatic Trivelpiece-Gould waves ($\omega = \omega_{ce} \cos\theta$) from the electromagnetic whistlers in the cold plasma dispersion relation. As kd_e approaches 1 the mode becomes more electromagnetic, eventually becoming the electromagnetic whistler mode ($\omega = \omega_{ce} k^2 d_e^2 \cos\theta$) when $k^2 d_e^2 \ll 1$.

5.2.4 Observation summary

In summary, we have measured spiky, skewed turbulence driven during the reconnection events. Study of individual spikes has found that they travel along the magnetic field at supersonic speeds, roughly $2 \times v_{te}$. The spikes are all positive-potential, and are electrostatic phenomena. They are a few electron gyroradii in radius, or, equivalently, many 10's of Debye lengths. Their aspect ratio (ratio of size parallel vs. perpendicular to the magnetic field) is approximately spherical.

5.3 Discussion

The spikes measured in VTF fit well into the framework of electron hole theories discussed in Section 5.1. First, we observe positive-potential structures, which is consistent with holes, as positive ϕ is required to trap electrons. Further, electron holes have been documented in many simulations to be the preferred nonlinear structure that grows in the plasma as a result of a strong instability. The observations also are inconsistent with other nonlinear plasma structures, as is discussed in greater detail below. Some aspects of the structure agree well with the available theory for 3-D electron holes, for instance, the typical width of a few gyroradii is just right. On the other hand, their parallel size is large, and they travel quickly compared to available theories, points which are addressed below.

First, the typical perpendicular size of the observed electron holes (a few ρ_e) is in agreement with available space observations and simple theoretical considerations. Franz *et al.* [128] have presented a statistical study of the inferred parallel and perpendicular sizes of electron holes measured by the POLAR spacecraft. The critical parameter here is ω_{pe}/ω_{ce}, or equivalently, ρ_e/λ_D. They found that the perpendicular size transitioned from being a few λ_D when $\omega_{pe}/\omega_{ce} \leq 1$ to being a few ρ_e when $\omega_{pe}/\omega_{ce} \geq 1$. This concurs with our measurements of ρ_e-scale holes, as VTF is in the latter regime, $\omega_{pe}/\omega_{ce} \sim 10$. Further, as discussed in the literature review, theory also predicts that ρ_e sets a minimum perpendicular size: holes depend on a positive potential causing depletion of electrons, which results only when the electrons obey a magnetized, 1-D response along the field lines. To keep the electrons magnetized, the hole's perpendicular size must be at least a few gyroradii. Here, however, we note again that there does not appear to be a complete and satisfactory theory for electron holes at finite magnetic field.

While the perpendicular size seems to be in agreement, the parallel size is larger than most space observations. The typical *parallel* size of holes observed by spacecraft [97, 98, 128] is nearly always a few Debye lengths. This is much narrower than the holes we have observed, which are roughly 60 λ_D wide. However, holes this wide are not theoretically forbidden: in fact, calculations show that holes become wide ($\gg \lambda_D$) when they move at high speeds ($v_{hole} \approx v_{te}$) [106]. This is qualitatively consistent with the measurements here in that we observe holes that are both wide and fast.

Interestingly, based on available theories, the holes appear to move *too* fast. Schamel's

limit [96] (also found by Goldman [106]) for instance is that the speeds should be less than $0.9 \times v_{te}$, whereas we observe closer to $2 \times v_{te}$. However, a major uncertainty here is that this is v_{te} evaluated with our default electron temperature of 15 eV. It is quite likely that the electron temperature increases dramatically during the reconnection events. Measurements with electron energy analyzers, presented in this thesis, have found that the *tail* of the electrons is heated; unfortunately, bulk measurements are not yet available, and it is the bulk temperature that sets the relevant speed. In addition, Schamel's speed limit is based on Maxwellian, bulk distributions, which may not be the relevant electron distributions during the reconnection events, since they are being strongly heated (and energized, presumably enough to drive these strong instabilities). Therefore, it seems best to defer this point of comparison until more complete measurements of the electron distribution, especially the bulk, are available.

One important consequence of the fast velocity of these plasma structures is that they likely do not evolve out of Buneman instability, as did the electron holes observed by Drake *et al* in reconnection particle simulations [37]. Buneman instability is a slow mode, with phase velocities of order a few times the ion sound speed. In fact, Buneman instability is closely related to the more commonplace ion-acoustic instability, the difference being that Buneman occurs when the relative electron-ion drift becomes larger than the electron thermal speed. It is difficult to imagine this situation prevailing in VTF. As we found in Chapter 3, typical electron-ion drift speeds (inferred from the average plasma current) are only 10-20% of the electron thermal speed.

As a result, *electron-electron* instabilities, i.e. bump- or beam-on-tail, seem a much more likely source of these holes. In the previous chapter, we discussed observations of high-frequency Trivelpiece-Gould modes and their source from bump-on-tail instability. The nonlinear evolution of particularly strong beam-driven Trivelpiece-Gould modes is a good candidate for the source of the holes. In this connection, note that the size of the holes is comparable to the wavelength for Trivelpiece-Gould modes ($\omega = \omega_{ce} \cos\theta$) resonantly driven by super-thermal electron beams: $f_{ce} \times L \approx 2 \cdot 10^9 \text{ s}^{-1} \times 2 \text{ mm} \approx 4 \times 10^6 \text{ m/s}$, very close to the observed hole speeds.

5.3.1 Comparison with other theories for nonlinear plasma structures

We have found generally good agreement with the electron-hole based theories. Here we compare with other known nonlinear plasma structures; notably, we have not found other classes of theories which agree with the available measurements.

Two basic classes of theories exist for nonlinear plasma structures, based on the pertinent plasma nonlinearities. The first, "envelope soliton theories," rely on high-frequency plasma waves for this nonlinearity. (For a review, see Ref. [129].) In these structures, a high-frequency "pump-wave" is present, and this pump wave is strong enough to act back onto the plasma bulk by the "pondermotive force." The pondermotive force is an effective force felt by a particle which pushes it away from regions of strong high-frequency fields. When this force is strong enough, enough particles can be pushed away from the region of high frequency waves to locally change the dielectric properties of the plasma. This feedback effect can work to trap the high frequency wave (since waves can be reflected from changes in the dielectric), and thereby create small regions ("envelopes") of intense, strong waves.

If this was the source for the structures we have observed, we would hope to see both the high frequency waves and the slower "low-frequency" modulation of the density and other parameters. However, we have not observed higher frequency components inside the hole structures; they appear to be simply unipolar spikes. However, more confirmation is desirable, as the high frequency waves (ostensibly electron plasma waves, or more specifically upper-hybrid waves) would be very high frequency modes, roughly 10 GHz for our experimental conditions.

To this end, it is important to consider the physics of the envelope in greater detail. In particular, it does not appear that there exists (within available theories) an envelope soliton structure that can travel at the speeds observed in these experiments. The reason is that the envelope in these theories is in fact a low-frequency wave. For example, in the classic Zakharov envelope soliton theory, (which uses electron plasma waves as a pump) the low frequency envelope is an ion-acoustic wave. In the magnetized soliton theory of Porkolab and Goldman [130] (where upper-hybrid oscillations are the pump), the low frequency envelope can be either ion-acoustic waves or Alfvén waves. Crucially, in both cases the low frequency response involves the ions. However, if this is the case the envelope and hence structure will never be able to travel as fast as observed in these experiments (the electron thermal

speed or above). Therefore, it seems unlikely that envelope soliton structures describe the observations, based both on the lack of observed internal pump waves and the inability for available theories to account for the high speed of the observed structures.

The second class of nonlinear, coherent plasma structures do not involve pump waves at all. Instead, the relevant nonlinearities are furnished directly by the equations of motion. This class has two subclasses, based on whether one is dealing with pure fluid theory or kinetic theory. The kinetic theory we have already described in detail—these are the electron (or ion) holes. The fluid theories rely on (abundant) fluid nonlinearities and are mathematical kin to the classical "Korteweg-deVries" (KdV) solitons [105]. In all these theories, a wave-steepening effect associated with the nonlinearity (for example, water waves can travel faster when the water is deeper, therefore peaks will tend to catch up with troughs, working to steepen the wave) balances with a natural dispersing effect of the medium, yielding a coherently propagating structure.

In plasma, these include, for example, ion acoustic solitons, *electron* acoustic solitons, Alfvén solitons, drift wave solitons, and many others. (For a review of solitons in plasma, see Ref. [131].) For the present measurements, most of these can be discounted out of hand, since their velocities or sizes will differ by orders of magnitude from the structures observed here. One which comes closest to matching our observations are Trivelpiece-Gould solitons, as observed and described theoretically by Ikezi and collaborators [132], which were found in concert with Saeki's investigations of electron holes in a discharge tube discussed briefly above. However, as Ikezi *et al* experimentally observed, the Trivelpiece-Gould solitons depend on electron compression for the relevant nonlinearity, and it turns out will always have $e\phi < 0$, contrary to the structures observed here. Another potential candidate, electron acoustic solitons [133], were also once proposed as an explanation for BEN, however are also compressive, requiring $e\phi < 0$. (These structures also require unique plasma conditions, with a dominant, hot plasma component and a *small*, cold component, whose densities satisfy $n_c \ll n_h$. This situation is quite difficult to imagine prevailing in VTF.)

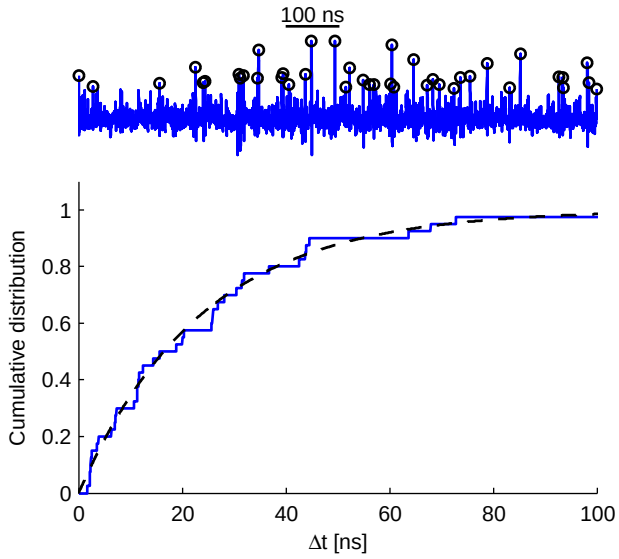

Figure 5-9: Spike-spike correlation studied from the distribution of inter-spike arrivals. (a) Data trace showing identified spike events. Time delays between spikes are measured and sorted (b) *Cumulative* distribution of time-delays between holes, showing total fraction of time delays $\leq \Delta t$. The mean hole-rate was about 40 holes/μs.

5.4 Spike-spike correlations

This section presents an additional set of observations: spike-spike correlations. Up until now we have discussed properties of single spikes—size, shape, and correlations of single spikes between separate probes. Here, we present data on the correlations *between* spikes—the distribution of times between spike arrivals. We find that the arrival of spikes cannot be distinguished from a random, Poisson process.

Figure 5-9 shows an example cumulative distribution of spike arrivals. To generate this, first spikes were identified in the data stream, as shown in Fig. 5-9(a), and from this the set of spike-spike delays are measured. The cumulative distribution of delays is then measured from the data by counting the number of delays less than a time Δt. This is shown as the blue, stair-step curve in Fig. 5-9(b). On the other hand, if the spikes arrive randomly in time (i.e. a *Poisson* process) with average rate r, then the probability of finding two spikes separated by the time range Δt to $\Delta t + dt$ is

$$p\,(\Delta t)dt = r\exp(-r\Delta t)\,dt. \tag{5.5}$$

This is the probability distribution of delays. The cumulative distribution is its integral,

$$C(\Delta t) = 1 - \exp(r\Delta t). \tag{5.6}$$

This theoretical distribution is shown in the dashed line in the figure, having estimated the rate r from the total number of spikes counted in the time window.

Traces like this have been examined for many discharges, and for various time periods within discharges, and this random process appears to be the generic case. However, in general, an exponential curve only prevails if a reasonably short section (typically 1-2 μs) of fluctuation data is studied. Over longer times, i.e. the time scales for reconnection, the rate of holes r is not constant. That leads to a trivial deviation from the exponential theory shown. On the other hand, *intrinsic* correlation phenomena, such as the holes arriving on a cadence, have not been observed. In conclusion, it appears that individual holes are not correlated to one another, and their arrivals at the probe are random, independent events.

Early theoretical work on electron holes by Berk *et al* found that in the initial phase of these instabilities, one primordial hole will grow per wavelength. However, during the non-linear phase of the instabilities, holes will coalesce, yielding fewer, but ultimately stronger holes. This coalescence process was originally found in numerical experiments of Berk *et al* [102], and studied experimentally by Saeki *et al* [109]. These measurements suggest that holes in VTF have undergone enough random coalescence to have lost all imprint of the initial conditions.

5.5 Correlation of electron holes with reconnection

Figure 5-10 shows the statistical connection between holes and reconnection events. To quantify the presence of the holes, we measure the hole-rate, i.e. holes observed by a probe per microsecond. In Fig. 5-10(a) we have aligned the reconnection events for the discharges based on the maximum toroidal electric field. Fig. 5-10(b), shows a 2-D histogram of the associated spike observations, indicating the fraction of discharges which observe the given rate of holes versus time; here the time axis is relative to the peak of the reconnection event. The spikes are clearly associated with the reconnection events, but note the delay between peak electric fields and peak hole observations. These demonstrate a clear correlation between elevated electric fields and hole observations, but suggest that the holes rise in

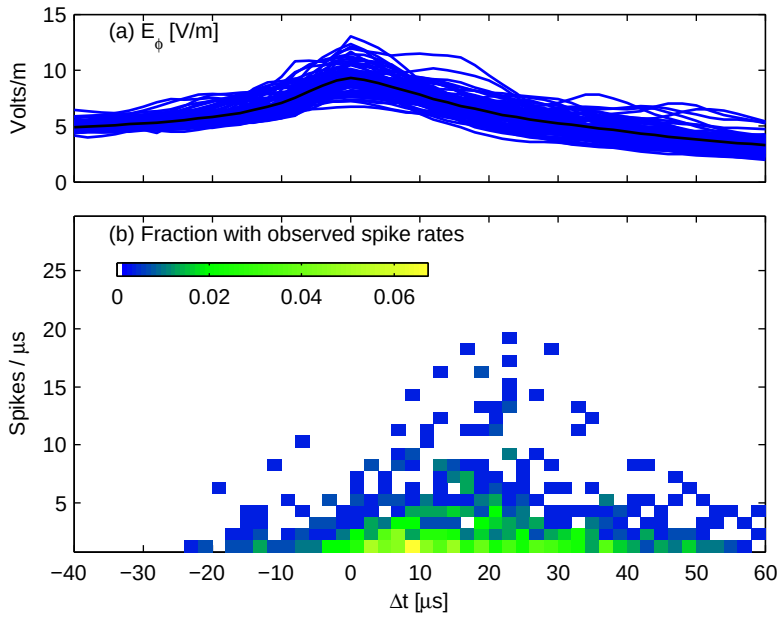

Figure 5-10: Time-correlation of electron holes and reconnection events. (a) Reconnection electric fields for 80 discharges aligned to have peak E_ϕ at $\Delta t = 0$. (b) Histogram of observed spike events, the fraction out of all discharges which observed a given rate of spikes versus time relative to the peak E_ϕ.

consequence to the reconnection events. This fits well with the overall picture that the holes arise from velocity space instability in the electron population due to strong energization by the reconnection events.

Finally, it appears that these holes do not strongly mediate *direct* anomalous resistivity in the plasma. To do so, they will have to effectively transfer momentum from electrons to ions. (The exchange of momentum between holes and electrons is clearly strong—consider electrons trapped inside the hole, whose momentum reverses at each bounce.) While hole-electron interactions can help rein in the tail of the electron distribution, unless momentum is coupled to the ions they will not lead to a change in net electron momentum. However, the ions and holes are weakly coupled due to the fast speed of the holes: $\frac{1}{2}m_i V_{hole}^2$, the ion energy in the hole frame, is huge, of order 10^7 eV. This causes the hole-ion interactions to become a weak, diffusive interaction, much like classical electron-ion collisions.

The following discussion of hole-ion coupling is also discussed by Ergun [98]. To estimate the rate of momentum transfer to ions from the holes, we estimate the change in ion parallel velocity $\Delta v_{||}$ per hole encounter. This is most easily calculated in the hole reference frame, in

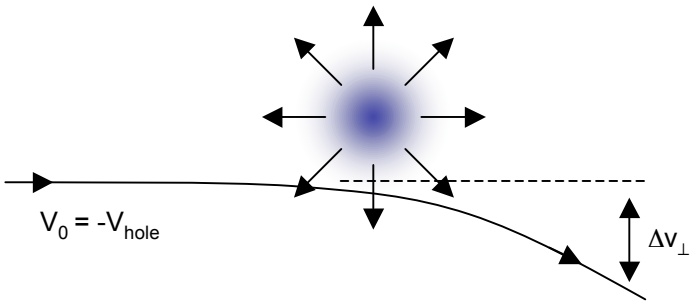

Figure 5-11: Hole-ion interaction: ions impinge on the hole at speed $v_0 = -V_{hole}$, where V_{hole} is the speed of the hole in the lab frame. Ions can be taken at rest in the lab frame as the hole velocities are much larger than any ion speed. Through the collision the ions gain a (small) kick $\Delta v_\perp$ and lose a small amount of parallel speed, $\Delta v_{||} \propto \Delta v_\perp^2$.

which the ion will impinge with a relative velocity $v_0 = -V_{hole}$. A schematic of this process is shown in Figure 5-11. Conservation of energy through the collision gives $2v_0\Delta v_{||} = -\Delta v_\perp^2$. Here the weak coupling comes in: $\Delta v_\perp$ can be estimated based on a straight-line orbit past the hole as

$$\Delta v_\perp \sim \frac{e}{m_i}\int dt\ \nabla\phi \sim \frac{e}{m_i v_0}\int dx\ \nabla\phi \sim \frac{e\phi_0}{m_i v_0}, \tag{5.7}$$

where ϕ_0 is the peak potential associated with the hole. This straight-line calculation is appropriate because $e\phi_0/m_i v_0 \ll v_0$, exactly the weak coupling discussed above: ion energy in the hole frame is much larger than the hole potentials. We have also used the fact that the holes have unity aspect ratio in estimating the integral.

Letting the ion strike r holes per second, we find

$$\begin{aligned} E_{\mathit{eff}} &\sim \frac{m_i}{e} r\Delta v_{||}, \\ &\sim r\frac{e\phi_0^2}{m_i v_0^3}. \end{aligned} \tag{5.8}$$

This expression can be seen to be analogous to our earlier quasi-linear estimate of the resistivity due to fast-phase-velocity linear modes, as presented in the previous chapter and in Appendix A. The change is that $\gamma\langle\tilde{\phi}^2\rangle \to r\phi_0^2$, and v_0 is identified with the wave phase velocity. (Recall that γ is the instability linear growth rate and $\langle\tilde{\phi}^2\rangle$ the fluctuation power.)

Based on this estimate, the momentum transfer from holes to ions is very small, corresponding to $\ll 0.1$ V/m (versus peak reconnection rates of 15 V/m.) This estimate is based on peak hole rates of 20 holes/μs, hole potentials of order 20 V, and hole velocities of order

5×10^6 m/s. Again, the root of the weak coupling is $e\phi/m_i V_{hole}^2 \approx 2 \times 10^{-6} \ll 1$; the ions have a huge amount of energy in the hole frame.

On the other hand, the holes can potentially play an indirect role in resistivity by reining in the tail of the electron distribution, because slow electrons are more collisional than runaways. Future work should continue to study the cause and effect between holes, fast electrons, and magnetic reconnection. In our naive estimate, the observed holes will not likely contribute substantial *direct* anomalous resistivity to the plasma, as their high velocity will limit interaction with ion populations. Instead, since the holes likely evolve from strong electron-electron instabilities they will primarily work to transfer momentum from fast to slow electrons.

5.6 Conclusions

In conclusion, we report the identification of electron holes created during magnetic reconnection. The observation of strong, nonlinear turbulence suggests that the reconnection events are creating sharp beam-on-tail velocity space structures, which have strong growth rates sufficient to trap resonant electrons within the wave troughs.

Detailed study of individual holes has found that their typical sizes are a few ρ_e. The perpendicular size is in agreement with space observations and supports the idea that holes must always be at least a few ρ_e wide in order to retain magnetized electron dynamics. The holes are strongly associated with electron energization, suggested both by their thermal or super-thermal velocities and their statistical connection to reconnection events and subsequent energetic particle production.

Chapter 6

Conclusions

This thesis has presented a study of plasma fluctuations during magnetic reconnection experiments on the Versatile Toroidal Facility. VTF studies magnetic reconnection in a low-β, strong-guide field regime. This is complementary to small-guide field or complete anti-parallel reconnection previously studied in basic laboratory devices, and potentially directly applicable to the sawtooth reconnection problem in tokamaks. The reconnection drive on VTF uses a set of four internal loops to generate poloidal magnetic field in the plasma, then induces a current sheet by rapidly transferring current from the inner pair to the outer pair.

An interesting regime in VTF has been identified with "spontaneous" reconnection events, where the current sheet is observed to be stable for 100's of μs before a reconnection event releases the magnetic energy on a shorter timescale of a few 10's of μs. The reconnection rate is thus observed to be highly variable in time, which is useful for experimentally determining which mechanisms are essential for fast reconnection. It may also suggest answers to the "trigger" question—what causes the onset of fast magnetic reconnection in systems like solar flares or the magnetotail?

This thesis has presented experimental study of electrostatic fluctuations which arise during these magnetic reconnection events. A main aim has been to determine if "anomalous resistivity" due to particle scattering off the fluctuations can be the cause of fast reconnection in VTF. Fluctuations are observed with "fast" Langmuir probes, which are impedance matched and have bandwidth to at least 2 GHz, enabling observation of modes up to the electron cyclotron frequency f_{ce}. Strong, broadband fluctuations, with a frequency

range extending from near f_{LH} to f_{ce} arise during the reconnection events.

Based on wavelength and frequency measurements, two classes of waves are discerned: lower-hybrid waves and Trivelpiece-Gould waves. These two classes have both different dispersion characteristics and different time behavior in response to the reconnection event. The lower-hybrid waves are more tightly-coupled to the reconnection events, and modeling has shown that they can be driven by cross-field currents or gradients which arise during the reconnection events. An interesting possibility is instability due to strong gradients in the (parallel) electron temperature; these gradients are observed, using the energy analyzer probe, in the "filamentation" of the fast electron population. The Trivelpiece-Gould waves, on the other hand, have a very fast phase velocity, $\sim 10\ v_{te}$ and therefore appear to be driven by velocity space instability of a fast electron population driven by the reconnection events. In both of these cases, however, the most likely instability mechanisms are connected to the heating of electrons by the reconnection events.

In addition to broadband fluctuation observations, the high bandwidth of modern oscilloscopes allows direct, *time-domain* observation of fast plasma turbulence. This has enabled the observation of spiky turbulence due to the formation of "electron phase-space holes," within the turbulence on VTF. Electron holes have received substantial attention lately due to observations by the new generation of spacecraft in the earth's magnetosphere. They are understood to arise in the nonlinear evolution of strong, beam-driven instabilities in the plasma, either electron-ion (Buneman) instability or electron-electron (cold beam-on-tail) instability. In either case, they result when the instability grows fast enough to saturate by trapping particles. The super-thermal velocity of the holes observed on VTF implies that they arise from a strong electron-electron (i.e. beam-on-tail) instability.

Overall, however, it cannot be concluded that the fluctuations observed are essential to the reconnection process on VTF. While they likely play a role in reining in the tail of energetic electrons, their fast phase velocity limits the amount of momentum coupling between electrons and ions. Furthermore, fluctuations are found to lag the reconnection events, suggesting that the fluctuations are driven as a consequence of reconnection, rather than a cause. This fits nicely with the picture of a velocity-space drive for the modes, where the chain of causation is: 1) reconnection events create large inductive electric fields; 2) this accelerates and energize electrons; 3) the modes arise from subsequent velocity-space instability.

In addition to comparing the time correlation of the instabilities and the reconnection events, we have also made some preliminary estimates of the anomalous resistivity due to the waves using quasi-linear theory, or in the case of the holes, direct estimates of the momentum transfer from ion-hole collisions. Both of these results, however, did not find a large anomalous resistivity effect. For the electron holes, the effect was very small, but this may be expected because the modes appear to arise from strong *electron-electron* instabilities, and move very fast compared to ions. The effect of the lower-hybrid waves has been estimated to be stronger, with effective electric fields near 1 V/m, but still too small to compete strongly against the typical reconnection electric fields of at least 15 V/m. However, these estimates are quite crude, based on the limitations of quasi-linear theory and the uncertainties in the calibration of the probes.

Future investigations can continue to search for fluctuations during reconnection in VTF. So far, ion acoustic fluctuations have not been observed, but it is possible that they are masked by stronger lower-hybrid fluctuations. Future work could investigate their existence using a modified probe which looks at current fluctuations with a strong, negative probe bias, thereby suppressing the electron component of the fluctuations and focusing on ion (density) fluctuations.

This research also suggests a number of promising roads for more detailed study of the electron distribution function during the reconnection events. This appears to require the construction of energy analyzing probes about a factor of 3–5 smaller than the seven-channel probe described here; this is necessary to resolve the observed "filamentation" of the fast electron populations. Such a probe might work if collectors (rather than grids) are used for electron energy discrimination and all collectors are installed behind a single ion-rejecting grid. It will also be useful to study the bulk of the electron distribution in greater detail, again with multi-channel Langmuir probes integrated into a small area; no grid is required in this case. This work would be useful in concert with further study of electron holes; there are some theoretical predictions of hole speed–size relations [106] but these require knowledge of the bulk electron distribution. Finally, experiments should search for higher-energy runaway production (in the 1 keV range) suggested by the observation of the fast phase-velocity Trivelpiece-Gould modes.

Appendix A

Quasi-linear Theory

This appendix describes the calculation of quasi-linear electron-ion momentum coupling due to wave turbulence. It is the simplest theory to go beyond linear instability theory and estimate the *nonlinear* feedback of the unstable waves back onto the equilibrium quantities. This simple formalism allows for simple estimation of the order-of-magnitude coupling due to the waves. It is covered in greater detail in, e.g. Ref. [30].

In general, the anomalous resistivity or anomalous momentum coupling arises due to correlations between fluctuating quantities in the nonlinear momentum equations. The time average for any single fluctuating quantity such as the electric field will be zero, but due to correlations the time average of the nonlinear product of fluctuating quantities can be finite and therefore affect the "slow" or DC dynamics of the system. To proceed one splits up quantities like the densities, velocities, and electric fields into steady and fluctuating parts: $\mathbf{E} = \bar{\mathbf{E}} + \tilde{\mathbf{E}}$, $n = \bar{n} + \tilde{n}$, etc. These are defined so that $\langle n \rangle = \bar{n}$, where $\langle \cdot \rangle$ is a suitable time- or space-average.

Next, consider the parallel component of the electron momentum equation,

$$nm \left(\frac{\partial v_{||}}{\partial t} + \mathbf{v} \cdot \nabla v_{||} \right) = -eE_{||}n - \nabla p. \tag{A.1}$$

Because this is a *nonlinear* equation, correlations between fluctuating quantities act back onto the DC, or equilibrium pieces. For our purposes here, the most important term here is $E_{||}n$, which describes momentum input to the electron population from electric fields. Accounting for fluctuations,

$$\left\langle E_{||}n \right\rangle = \bar{E}_{||}\bar{n} + \langle \tilde{E}_{||}\tilde{n} \rangle. \tag{A.2}$$

The first term here is the net momentum input from DC fields, such as the reconnecting electric field. Correlated fluctuations, then, also contribute an effective DC electric field

$$E_{||,\mathit{eff}} = \frac{\langle \tilde{n}\tilde{E}_{||}\rangle}{\bar{n}}. \tag{A.3}$$

This may compete against the reconnection electric field. Next, note that correlated fluctuations directly give rise to momentum coupling between electrons and ions: in the simplest case, for fluctuations which are quasi-neutral, $\tilde{n}_i = \tilde{n}_e$. In this case the momentum carried by the waves is small, and the net momentum removed from the electrons ($-e\langle\tilde{E}\tilde{n}_e\rangle$) is given directly to ions ($+e\langle\tilde{E}\tilde{n}_i\rangle$).

This is actually a crucial point, because if one considers in more detail the kinetic (rather than fluid) theory of the interactions of the fluctuations with the electrons, one finds many resonant effects. (For instance, the Trivelpiece-Gould modes of Section 4.4 are found to be resonantly driven by a bump on tail instability of fast electrons.) However, such resonant interactions can simply rearrange the electron distribution function without changing the net momentum. This can have side-effects on resistivity, for instance by restraining the runaway population. However, for simple estimates here we will just calculate how much momentum is directly coupled to the ions.

One final point is that Eq. A.3 is formally exact, and if it was possible to directly measure all quantities simultaneously and perform the necessary averages, one would directly obtain the effective electric field. This is not the case here—note instead that we have not even measured $\tilde{E}$, but rather $\tilde{\phi}$. This is where quasi-linear theory comes in: one uses the properties of *linear* waves to estimate the correlated quantity $\langle\tilde{E}\tilde{n}\rangle$. Based on the discussion above, we calculate the ion density response; this is furthermore useful because it is simpler to calculate than the electron response. The final goal is to relate E_{eff} to $\langle\tilde{\phi}^2\rangle$, the experimentally measured fluctuation power.

First, $\tilde{\phi}$ is Fourier-analyzed. For our averaging operation here we will consider a space-average, and assume that the turbulence statistically homogenous in space. Therefore, $\phi_{\mathbf{k}}$ is defined as

$$\phi_{\mathbf{k}} = \int_{-\infty}^{+\infty} d^3x\, \mathrm{e}^{-i\mathbf{k}\cdot\mathbf{x}}\tilde{\phi}(\mathbf{x}). \tag{A.4}$$

This is related back to $\tilde{\phi}(\mathbf{x})$ through the inverse Fourier transform

$$\tilde{\phi}(\mathbf{x}) = \int_{-\infty}^{+\infty} \frac{d^3k}{(2\pi)^3}\, \mathrm{e}^{+i\mathbf{k}\cdot\mathbf{x}} \phi_{\mathbf{k}}. \tag{A.5}$$

It can be shown that

$$\left\langle \tilde{\phi}^2 \right\rangle = \frac{1}{V}\int d^3x\ \tilde{\phi}(\mathbf{x})^2 = \frac{1}{V}\int_{-\infty}^{+\infty} \frac{d^3k}{(2\pi)^3}\ \phi_{\mathbf{k}}\phi_{-\mathbf{k}}. \tag{A.6}$$

Where the angle brackets are the space average defined above, and V is an averaging volume. Note that because $\tilde{\phi}$ is real, $\phi_{\mathbf{k}}$ has symmetry properties such as $\phi_{\mathbf{k}}^{\dagger} = \phi_{-\mathbf{k}}$, where the dagger indicates complex conjugation.

With these definitions, the evaluation of $\langle \tilde{n}\tilde{E}_{||} \rangle$ proceeds as follows. First, from the ion momentum and continuity equations, assuming cold, unmagnetized ions pertinent for high-frequency waves

$$n_{\mathbf{k}} = \frac{in_0 e}{m_i \omega_{\mathbf{k}}^2} \mathbf{k}\cdot\mathbf{E}_{\mathbf{k}}. \tag{A.7}$$

This is the central assumption of quasi-linear theory. Here, $\omega_{\mathbf{k}}$ is the complex frequency of the mode labeled by $\mathbf{k}$. It will be shown momentarily that an imaginary part of ω is necessary to have a non-zero correlation $\langle \tilde{n}\tilde{E}_{||} \rangle$. On another note, one may consider *kinetic* ions in more detail using the Z-function, but the cold response is actually always an over-estimation and is therefore a useful upper bound. Next, following the space average used in Eq. A.6,

$$\begin{aligned}
\mathbf{E}_{ql} &= \frac{\langle \tilde{n}\tilde{\mathbf{E}} \rangle}{n_0}, \\
&= \frac{1}{V}\frac{e}{m_i}\int \frac{d^3k}{(2\pi)^3}\ \frac{i\mathbf{k}\cdot\mathbf{E}_{\mathbf{k}}\mathbf{E}_{-\mathbf{k}}}{\omega_{\mathbf{k}}^2}, \\
&= \frac{1}{V}\frac{e}{m_i}\int \frac{d^3k}{(2\pi)^3}\ i\mathbf{k}\frac{k^2\phi_{\mathbf{k}}\phi_{-\mathbf{k}}}{\omega_{\mathbf{k}}^2}.
\end{aligned} \tag{A.8}$$

In the last step we have used $\mathbf{E}_{\mathbf{k}} = -i\mathbf{k}\phi_{\mathbf{k}}$. This expression can be verified to be real (for it must be) using the symmetry properties of $\phi_{\mathbf{k}}$ and $\omega_{\mathbf{k}}$. However, this is made manifest by taking the part of $i\omega_{\mathbf{k}}^{-2}$, finding,

$$\Re\left\{\frac{i}{\omega_{\mathbf{k}}^2}\right\} = \frac{1}{2}\left(\frac{i}{\omega_{\mathbf{k}}^2} - \frac{i}{\omega_{\mathbf{k}}^{\dagger 2}}\right) = 2\ \frac{\omega_{r\mathbf{k}}\gamma_{\mathbf{k}}}{|\omega|^4}. \tag{A.9}$$

Therefore, quasi-linear theory predicts that the effective electric field is given by the following integral over the spectrum of waves:

$$\mathbf{E}_{ql} = \frac{1}{V}\frac{2e}{m_i}\int \frac{d^3k}{(2\pi)^3}\frac{\omega_{r\mathbf{k}}\gamma_{\mathbf{k}}}{|\omega|^4}\,\mathbf{k}k^2\,\phi_{\mathbf{k}}\phi_{-\mathbf{k}}. \tag{A.10}$$

In a final step, this integral estimated by replacing factors in the integral with their value at the spectral peak (or at peak growth rate), so that the result can be related back to $\langle\tilde{\phi}^2\rangle$. This yields, for the parallel component of electric field,

$$E_{ql,||} \sim \frac{2e}{m_i}\left[k_{||}k^2\frac{\omega_r\gamma}{|\omega^4|}\right]_{max}\left\langle\tilde{\phi}^2\right\rangle. \tag{A.11}$$

This is the quasi-linear electric field.

Note a few interesting features. First, the coupling is proportional to the growth rate of the waves. (This in turn is based on the pertinent linear theory for their growth). Second, the coupling decreases like v_{ph}^{-3}, where v_{ph} is the phase velocity of the waves, so that the waves become decoupled from the ions when they move with high-velocity. For this reason, the high-frequency Trivelpiece-Gould modes discussed in Chapter 4 have a *very* small interaction with ions. Therefore, to find modes that supply appreciable anomalous resistivity, one must generally find low-phase speed modes which can have a strong interaction with the ions. Finally, E_{eff} here is determined based on waves moving in the positive direction; in this convention, waves moving in the negative direction, i.e. in the electron direction, will interact with the electron flow, and give rise to E_{eff} of the correct sign to counteract a positive DC (i.e. reconnection) electric field. This is the sign of waves observed in the experiment.

Finally, this quasi-linear estimate can also be seen to derive simply from scaling arguments and dimensional analysis. The only "knowledge" one must apply is that E_{eff} be linearly proportional to both the fluctuation power $\langle\tilde{\phi}^2\rangle$ and the wave growth rate. Then, for fast phase velocity waves (and cold ions), there is only one velocity scale in the problem, the wave phase velocity, for use in generating a formula for E_{eff} with the correct units of [V/m]. This uniquely determines the scaling in Eq. A.11. A similar interaction law was derived in Eq. 5.9 for the interaction of ions with the electron holes, which are *nonlinear* turbulent structures. The root of the common scaling is the weak coupling between the ions and fast-phase-velocity modes.

Appendix B

High-frequency Langmuir probe response

Chapter 2 discussed the frequency response of RF Langmuir probes at high frequencies, finding that the plasma-probe coupling can be modeled as a paralleled resistor-capacitor, the "plasma-probe" resistance R_p and capacitance C_p. At high frequencies ($f \gg f_{pi}$), the capacitance is predicted to dominate the coupling. We have conducted some experiments to test these concepts. The agreement between theory and experiment demonstrates an understanding of the behavior of the probes at these frequencies, and provides a measure of how well-calibrated the probe system is.

We present two sets of measurements. In the first, the plasma acts like a broadband noise source, from which the probe response is derived by comparing the amplitudes of normal and purely-capacitively-coupled probes. In the second, we analyze electron hole waveforms in more detail. These are found to generally have a negative "tail" on the trailing edge of the spike waveform, and this is attributed to the capacitive component of the probe response.

B.1 Response to broadband plasma waves

We have tested the high-frequency capacitive coupling effect by comparing two neighboring probes (separation about 2 mm) where one has a teflon "sock" covering the probe tip. The sock blocks direct electrical connection, forcing the probe to have only couple capacitively to the plasma. Figure B-1 shows a schematic of the normal and socked probes, plus high-frequency circuit models. Similar capacitively-coupled Langmuir probes have been described

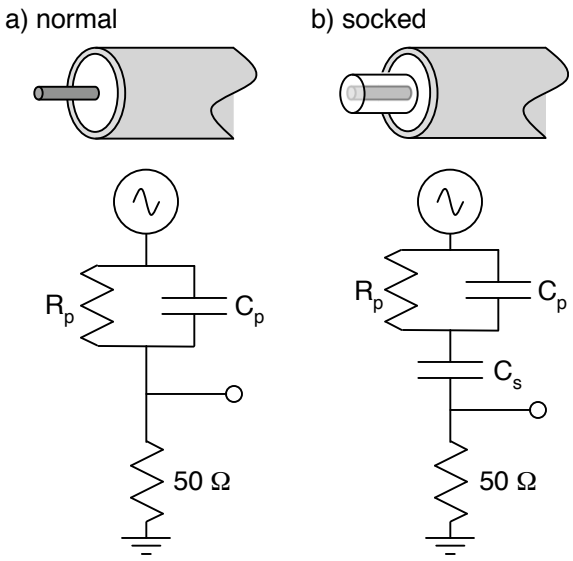

Figure B-1: Picture of normal and socked probe tips. The "sock" is a teflon sleeve with outer diameter = 0.6 mm.

in the literature [134], though there the signal path was not impedance matched and the measurement system was not designed for high-frequency studies.

The typical sock used is a teflon sleeve originally used to insulate a 6 mil wire. Its capacitance is estimated to be about $C_s = 0.32$ pF, based on cylindrical capacitance $\epsilon_r \epsilon_0 2\pi l / \log(b/a)$, where l is the length (2 mm), b/a is the ratio of outer and inner radii (2), and $\epsilon_r = 2$ is the relative dielectric constant of teflon. Because $C_s \approx C_p$, C_s has a strong effect on the response of the probe.

We have already discussed the model plasma-probe transfer function $H(\omega) = V_{out}/V_{in}$ for the normal probe, in Section 2.2.3,

$$H(\omega) = \frac{50}{50 + \dfrac{R_p}{1 + i\omega R_p C_p}} \tag{B.1}$$

With the sock in place, the transfer function $H(\omega) = V_{out}/V_{in}$ becomes instead:

$$H(\omega) = \frac{50}{50 + \dfrac{1}{i\omega C_s} + \dfrac{R_p}{1 + i\omega R_p C_p}} \tag{B.2}$$

The most important effect of C_s is that it allows us to demonstrate that a normal probe has a capacitive response at high frequencies. The socked probe has a high-pass, rising response

across all frequencies. In contrast, as discussed, the normal probe is predicted to have a flat response ($\approx 50/R_p$) at low frequencies, with a rising, capacitive response starting at $1/(2\pi R_p C_p)$. Therefore, the ratio of the two signals is predicted to become *flat* at high frequencies, where both normal and socked probes are in the capacitive regime.

The complex amplitude ratio r of normal to socked probes, according to this model is

$$\begin{aligned} r(\omega) &= \frac{H_{norm}}{H_{sock}} \\ &= \frac{50 + \dfrac{1}{i\omega C_s} + \dfrac{R_p}{1 + i\omega R_p C_p}}{50 + \dfrac{R_p}{1 + i\omega R_p C_p}} \qquad \text{(B.3)} \\ &\approx \frac{1 + i\omega R_p (C_p + C_s)}{i\omega C_s R_p} \qquad \text{(B.4)} \end{aligned}$$

In the last step, we have ignored 50 Ω compared to $R_p/(1 + i\omega R_p C_p)$, which applies up to the very high frequency $1/(2\pi 50 C_p)$. We have also assumed that $R_p C_p$ for the two probes is equal.

In particular, note that the ratio at low frequencies $r \approx 1/(i\omega R_p C_p) \propto 1/f$, since the normal probe is resistive but the socked probe capacitive. In contrast, at high frequencies, the ratio approaches a constant, $(C_p + C_s)/C_s$.

Figure B-2 applies this analysis to typical time traces. Figure B-2(a) shows the fluctuation traces from a normal (blue) and socked (green) probe. The socked probe typically measures much lower amplitudes, because the dominant, low frequency modes (near 10 MHz) are strongly filtered by C_s. Figure B-2(b) shows the power spectrum of the two signals over this time window, and (c) shows the ratio of the two power spectra. We have also fit the model *power* ratio $|r(\omega)|^2$ (from Equation B.3), which is shown as the black curve. Of note, we find from the fit $C_p \approx 0.2$ pF, and $R_p \approx 5$ kΩ. The observed corner frequency is therefore $1/(2\pi R_p C_p) \approx 160$ MHz.

We have performed this analysis for a number of discharges. In order for this analysis to succeed, it is necessary to find time periods with relatively strong fluctuations, so that signals on the socked probe are strong compared to bit noise. It is also necessary to find times when aliasing effects from high frequency modes above 1.25 GHz are weak compared to the lower frequencies.

When these criteria are met, in general we find reasonable agreement between the data

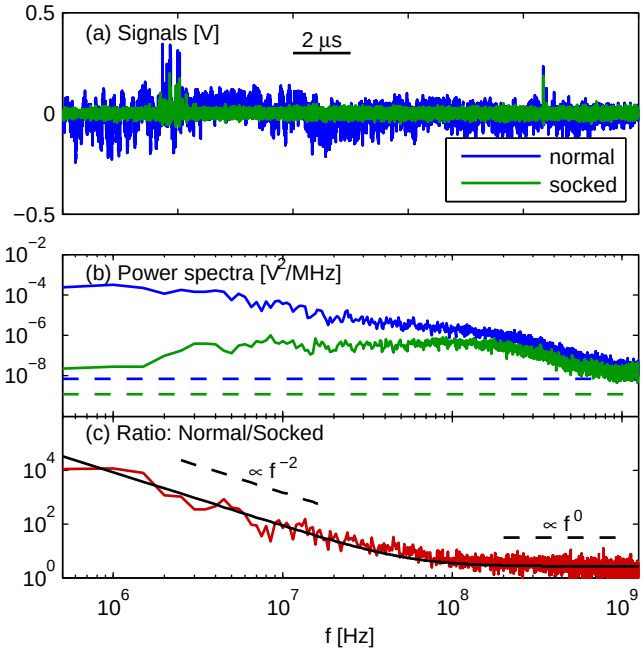

Figure B-2: Test of capacitive probe response at high frequencies. (a) Broadband signals seen by both a normal probe (blue) and a probe with a capacitive sock over the end (green). (b) Power spectra of normal and socked probes. Dashed lines are the (bit)-noise floor for each signal. (c) Ratio of normal to socked spectra. The power ratio at low frequencies $\propto f^{-2}$ because of the extra capacitive response of the sock probe. At high frequencies the ratio becomes flat once the normal probe's response becomes capacitive.

and the models. The fast Langmuir probes clearly exhibit a capacitive response at high frequencies. However, a wide variation of corner frequencies is observed, ranging from 100 to as high as 800 MHz. Notably, most of the variation seems to be attributable to variation in R_p, rather than C_p. This is found because the ratios at high frequencies, which is solely due to C_p/C_s, is relatively constant, while the corner frequency moves around.

These observations are qualitatively consistent with the simple theory presented in Chapter 2. There, the probe-plasma capacitance was shown to be fixed by the structure of the sheath around the probe. The width of the sheath is a few Debye lengths, and changes somewhat weakly with probe bias. On the other hand, the probe-plasma resistance varies more dramatically with plasma parameters and the bias of the probe. First, at the floating potential, the resistance is inversely proportional to plasma density. Second, if the bias moves away from the floating potential, the resistance can change as the bias moves up the (exponential) electron $I(V)$ characteristic. If the probe moves 1 $T_e \approx 15$ V in bias, the resistance will change by a factor of 3. Finally, in general we find corner frequencies typically *above* what was predicted ($\approx 3\ f_{pi}$) in Chapter 2. For our typical estimated plasma densities of 1–2 $\times 10^{18}$ m^{-3}, $3f_{pi} = 100$–150 MHz.

B.2 Detailed electron-hole waveform modeling

As discussed in Chapter 5, the hole waveforms, typically only about 400 *ps* wide, push the bandwidth limits of modern oscilloscopes. The specified risetime of the Tektronix 7254 is about 100 ps (20–80%), so there is definite concern that the oscilloscope can artificially widen the spikes. A pulse generating circuit was therefore constructed from an impedance-matched RF relay (Coto Model 9802) and a short, 2 cm, coax stub charged through a large resistor. Closing the relay generates narrow (nominally 300 ps width) pulses to test the oscilloscope response. Notably, these pulses, as measured by the 7254, were narrower than the width of the smallest holes measured. This provided some confidence that the scope had a bit of headroom beyond the measured spike size, and that the spike widths were not simply set by the oscilloscope bandwidth

Nonetheless, electron hole measurements were subsequently repeated with a faster oscilloscope (Tektronix 72004) that had since become available. The 72004 has a specified 16 GHz analog bandwidth and a 14 ps rise time, far exceeding the bandwidth needed to

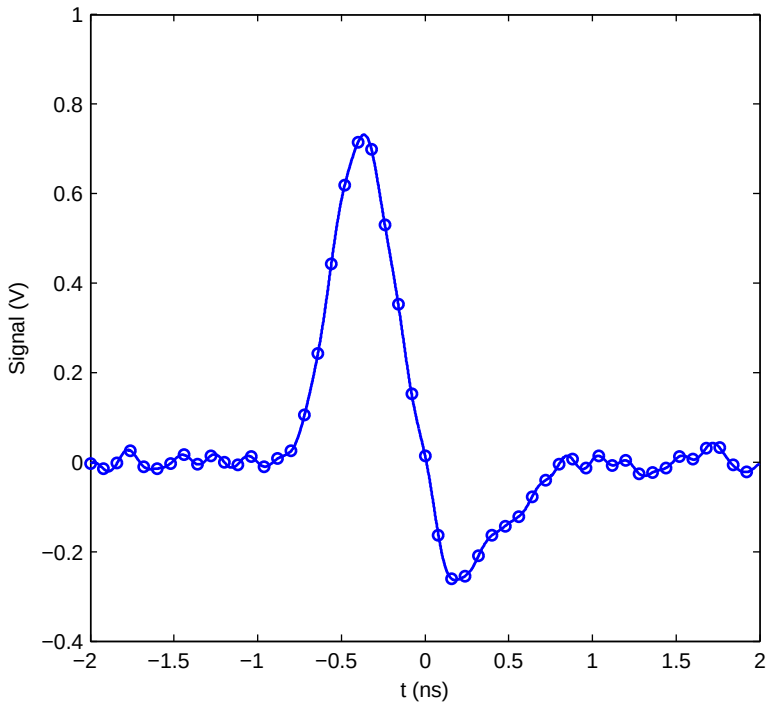

Figure B-3: A well-isolated, clean spike, illustrating the negative tail which appears on the trailing edge of the spike. Open circles are data points sampled at 12.5 GHz.

resolve the 400 ps-wide electron holes. The result of these tests first confirmed that the 7254 measurements were essentially correct. Second, we were able to investigate some interesting features of the hole waveforms, namely a negative "tail" on the trailing edge of the hole, as shown in Fig. B-3. This observation was at first troubling as it deviates from the idealized picture of the probe measuring an (attenuated) replica of the unipolar electron hole waveform.

Here it is shown that the negative tail can be explained by a more detailed account of coupling from the plasma into the probe, namely the "probe sheath capacitance" C_p which gives the probe a rising response at high frequencies. To model this phenomenon, a "natural" hole waveform (in the plasma) is assumed and this is run through the simulated filtering operation of the probe, generating model waveforms recorded by the oscilloscope. It is found that reasonable choices of parameters for the probe model can match the observed spike shapes.

Interestingly, the rising response of Langmuir probes at these high frequencies, compensates, to some extent, for the finite bandwidth of scopes like the 7254, aiding their ability to

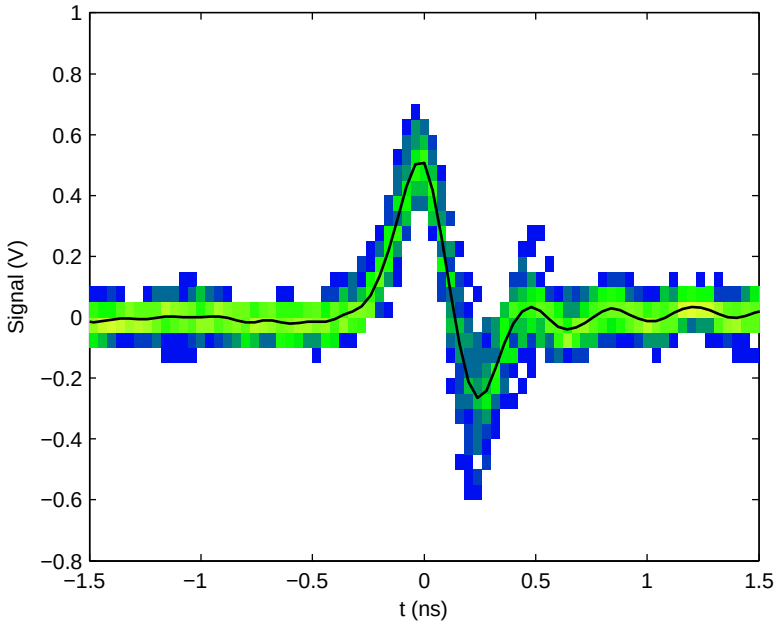

Figure B-4: Observed distribution of hole waveforms. Color indicates fraction of traces landing in a particular voltage-time $(\Delta V, \Delta t)$ bin.

resolve the spikes; effectively it cancels the first "pole" encountered as the 3 dB bandwidth is reached. All data in this section was taken with a Tektronix 72004 oscilloscope, whose 16 GHz analog bandwidth is fast enough to clearly resolve the spikes.

The particular hole waveform shown in Fig. B-3 was large and reasonably isolated from other fluctuations and from other holes, and therefore provides a clean picture of the phenomenon. To show that the tail is a generic phenomenon, Fig. B-4 shows a color histogram and an averaged spike shape. To assemble the data set, holes were identified based on strong local maxima between 0.35 and 0.6 V, and a further subset was taken from those that were cleanly isolated from other large fluctuations, including other spikes. Each spike serves as a "trigger" event and we can assemble a set of spike-traces based on a few ns of data surrounding each spike. The peak of the spike determines the time origin of each individual spike-trace. Linear backgrounds (inferred from data points sufficiently far away from the spike and tail) were subtracted off. Also, the finite rise-time of the coax has also been deconvolved from these measurements [135]. The span of trigger voltages here is a compromise between including enough spikes for good statistics and including too-heterogeneous a collection; approximately 40 spikes were used for this figure. A negative tail, typically about half the magnitude of the positive spike is apparent.

To understand the negative tail on the spike, we return to the high frequency Langmuir probe model. From the model high-frequency probe circuit, we found (Eq. 2.16)

$$V_{out}(\omega) \approx \frac{50}{R_p}\,(1 + i\omega\tau_p)\,V_{in}(\omega). \tag{B.5}$$

Here $\tau_p = R_p C_p$ is the time constant of the Langmuir probe filtering operation, above which the probe begins to have a rising, capacitive response. Transforming this back into the time domain, we find that

$$V_{out}(t) = \frac{50}{R_p}\left(1 + \tau_p \frac{d}{dt}\right) V_{in}(t). \tag{B.6}$$

Note that this response factors into two pieces. First, the prefactor $50/R_p$ affects the overall amplitude, but not the shape. Uncertainty in R_p will translate into uncertainties in establishing an overall calibration to the probe. The second term (in parenthesis), on the other hand, can modify the spike shape. In particular, as $\tau_p d/dt$ becomes finite a negative tail will appear on the spike.

To generate model waveforms to compare with the data, a natural $\mathrm{sech}^4(\cdot)$ spike shape is assumed,

$$V_{in} = \mathrm{sech}^4\left(1.21\frac{t}{\tau_s}\right). \tag{B.7}$$

The numerical coefficients are chosen so that τ_s is the full-width-half-maximum (fwhm) of the spike. The filtered V_{out} can be calculated analytically based on the model Langmuir probe response,

$$V_{out} \propto \left[1 - 4.85\frac{\tau_p}{\tau_s}\tanh\left(1.21\frac{t}{\tau_s}\right)\right]\mathrm{sech}^4\left(1.21\frac{t}{\tau_s}\right). \tag{B.8}$$

Fig. B-5 shows an example filtered spike, based on the sech^4-model and $\tau_p = \tau_s$. Note that an appreciable negative tail exists on the filtered waveform, with the negative excursion of about 1/2 of the spike maximum. The figure also serves to introduce some metrics which we will use to compare the models to the data. Of the various possible ways to measure the spikes, two have proven to be reasonably robust: $\Delta t_{s,a}$, the *apparent* fwhm of the positive portion of the spike; $\mathcal{R}$, the ratio of the upward to downward excursions of the voltage trace. For comparing the observations to models, these metrics are calculated numerically for various ratios τ_p/τ_s, and are plotted in Figure B-6.

The limits can be understood as follows: when $\tau_p \ll \tau_s$, the capacitive part of the

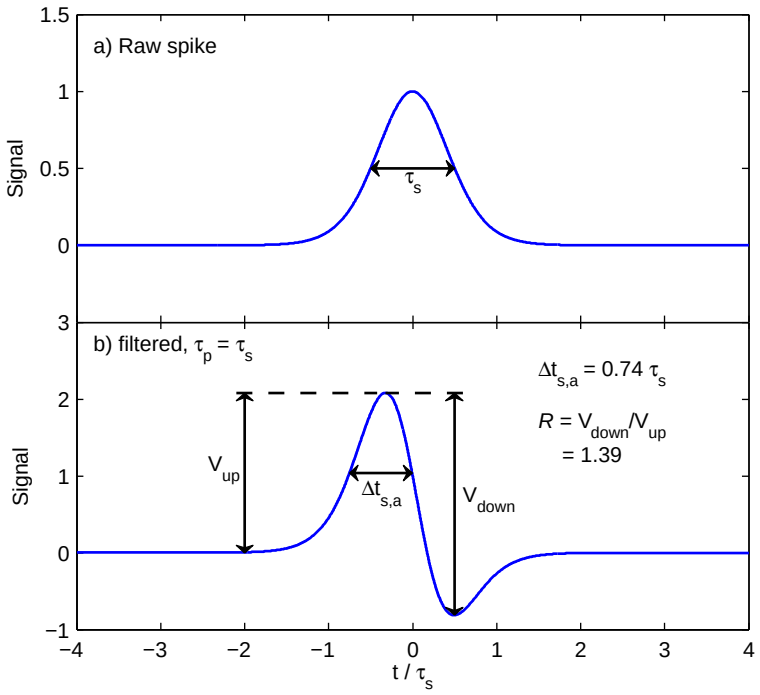

Figure B-5: Model spike waveform and modeled probe-plasma coupling. (a) sech^4-based spike and, (b) an example filtered version using the plasma-probe time constant $\tau_p = 1 \times \tau_s$.

probe coupling is small and the observed waveforms approach the "natural" spike shape, so $\mathcal{R} \to 1$, and $\Delta t_{s,a} \to 1$. On the other hand, as $\tau_p \gg \tau_s$ the observed wave forms will go over to a pure derivative of the spike, so $\mathcal{R} \to 2$. At the same time, $\Delta t_{s,a}$ goes to that of the derivative shapes, which is smaller by about 30%.

Other spike-like shapes (gaussian, sech^2) have been tried with the same procedure, and all are found to be essentially degenerate with one another. Once rescaled to have the same fwhm, all the shapes look very similar to one another, with differences only appearing at their wings. However, that is exactly where the signals are close to zero again, and so differences there can easily be masked by other fluctuations. A result is that, even though the various nonlinear theories predict their own spike shapes, it is difficult to experimentally differentiate between theories based solely on that criterion.

Next, we proceed to compare the theory developed here to our measurements. Figure B-7 shows a scatter plot and binned histograms of $\mathcal{R}$ and $\Delta t_{s,a}$ measured from a collection of spikes. The criteria for selecting spikes to include here is similar to as for Fig. B-4, though here we have used data from multiple shots to increase statistics. Of note, there is

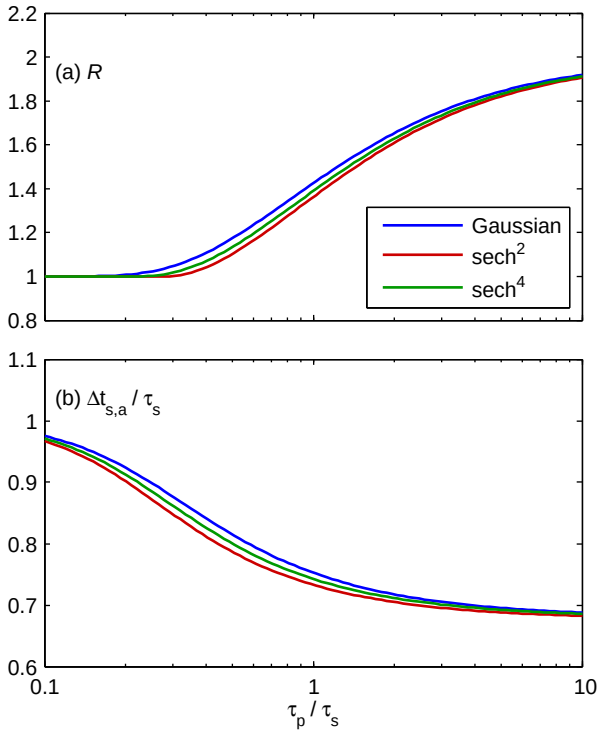

Figure B-6: Metrics of model hole waveform distortion due to capactive plasma-probe coupling, vs. τ_p/τ_s. (a) r = $|V_{max}/V_{min}$, and (b) $\Delta t_{s,a}$, the apparent width of the positive portion of the spike.

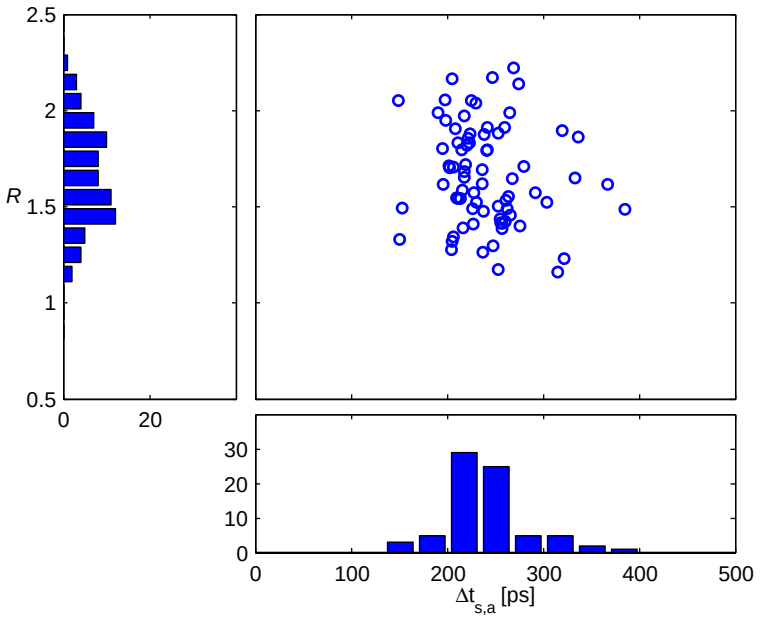

Figure B-7: Distortion metrics on experimentally observed electron holes. $\mathcal{R}$ and $\Delta t_{s,a}$ measured for spikes. The coax response has been deconvolved from the signals before measuring spike parameters. Typical $\mathcal{R}$ is 1.65, and $\Delta t_{s,a} = 240$ ps.

appreciable variation in the observed $\mathcal{R}$; the mean was 1.65, but a wide distribution is seen, varying from at least 1.5 to 1.8. Note that the the same large scatter in inferred $\mathcal{R}$ is also visible in the ensemble in Fig. B-4. The measured $\Delta t_{s,a}$ for these spikes falls in a tighter group around the mean of 240 ps.

Next, from the observed typical $\mathcal{R}$ and $\Delta t_{s,a}$, combined with knowledge of the probe filtering operation shown in Fig. B-6, it is possible to estimate the typical probe filtering parameters. First, the typical $\mathcal{R}$ of 1.65, τ_p/τ_s is estimated to be near 2. However, the wide variation in observed $\mathcal{R}$ gives a corresponding wide range of τ_p/τ_s from 1.5 to 3. There are a few potential interpretations for this. First, it is possible that other turbulence in the plasma adds noise to these measurements and obscures the spike shapes. In addition, τ_p can change due to variations in the plasma-probe coupling: $\tau_p = R_p C_p \propto 1/\omega_{pi}$, and therefore will fluctuate with the (turbulent, fluctuating) plasma density. Finally, note that while we have shown 1 probe here, there are differences (factors of 2) in $\mathcal{R}$ (and thus τ_p/τ_s) for different probes seeing the same spikes.

Nonetheless, based on these measurements, we will proceed to estimate the typical spike width and probe coupling τ_p. First, based on the typical τ_p/τ_s of 2, and typical $\Delta t_{s,a}$

of 240 ps, it is estimated that the typical spike widths τ_s are $\Delta t_{s,a}/0.7 \approx 340$ ps. (see Fig. B-6(b)). This is similar to our early measurements using slower oscilloscopes (as in Fig. 5-7), though slightly smaller. Combining the observed typical speed for these spikes (here, 5.5×10^6 m/s), we find again that the typical spatial widths are about 1.8 mm.

Finally, with the estimated τ_p/τ_s of 2, and now the inferred τ_s of 340 ps, τ_p is estimated to be 660 ps, which corresponds to a plasma-probe corner frequency of 250 MHz. This is roughly in line with what was estimated previously, $\sim 3f_{pi}$ which ranges from 100 to 150 MHz for argon densities of 1–2×10^{18} m^{-3}.

In conclusion, electron holes are positive-potential structures in the plasma, but simple unipolar waveforms are not exclusively observed. Especially when viewed at high-bandwidth, the spike waveforms typically have a negative "tail." However, here we have found that the intrinsic hole shapes *are* unipolar, and that the tail is an artifact of the plasma-probe coupling. Because of a capacitive component to this coupling, the probes have a rising response at high frequencies. Based on simple estimates of this response discussed in Chapter 2, one estimates that the corner frequency of this rising response is around 3 f_{pi}. This estimate is roughly in line with what is required to understand the observed waveforms. However, consistent with the discussion in Section B.1, often the corner frequency is somewhat higher than this value.

Bibliography

[1] E. Priest and T. Forbes. *Magnetic Reconnection: MHD Theory and Applications*. Cambridge University Press, New York, 2000.

[2] D. Biskamp. *Magnetic Reconnection in Plasmas*. Cambridge University Press, Cambridge, 2000.

[3] S. Masuda, T. Kosugi, H. Hara, S. Tsuneta, and Y. Ogawara. A loop-top hard x-ray source in a compact solar flare as evidence for magnetic reconnection. *Nature*, 371:495, 1994.

[4] V. Angelopoulos, J. P. McFadden, D. Larson, C. W. Carlson, S. B. Mende, H. Frey, T. Phan, D. G. Sibeck, K.-H. Glassmeier, U. Auster, E. Donovan, I. R. Mann, J. I. Rae, C. T. Russell, A. Runov, X.-Z. Zhou, and L. Kepko. Tail reconnection triggering substorm onset. *Science*, 321(5891):931–935, 2008.

[5] M. Yamada, F. M. Levinton, N. Pomphrey, R. Budny, J. Manickam, and Y. Nagayama. Investigation of magnetic reconnection during a sawtooth crash in a high-temperature tokamak plasma. *Phys. Plasmas*, 1(10):3269–3276, 1994.

[6] J. P. Freidberg. *Ideal Magnetohydrodynamics*. Plenum, New York, 1987.

[7] S. I. Syrovatskii. Formation of current sheets in a a plasma with a frozen-in strong magnetic field. *Sov. Phys. JETP*, 33:933, 1971.

[8] D. Biskamp. Magnetic reconnection via current sheets. *Phys. Fluids*, 29(5):1520–1531, 1986.

[9] R. L. Stenzel and W. Gekelman. Magnetic field line reconnection experiments, 1. Field topologies. *J. Geophys. Res.*, 86(A2):649–658, 1981.

[10] H. Ji, M. Yamada, S. Hsu, and R. Kulsrud. Experimental test of the Sweet-Parker model of magnetic reconnection. *Phys. Rev. Lett.*, 80(15):3256–3259, 1998.

[11] B. Coppi. Remarks on sequence-of-plasma-instabilities models of solar flares. *Astrophys. J.*, 195:545–552, 1975.

[12] E. N. Parker. Nanoflares and the solar x-ray corona. *Astrophys. J.*, 330:474–479, 1988.

[13] J. Lin. Theories of solar eruptions: a review. *New Astron. Rev.*, 47(2):53–84, 2003.

[14] P. A. Sweet. In B. Lehnert, editor, *Electromagnetic Phenomena in Cosmical Physics*, page 123. Cambridge University Press, New York, 1958.

[15] E. N. Parker. Sweet's mechanism for merging magnetic fields in conducting fluids. *J. Geophys. Res.*, 62(4):509–520, 1957.

[16] H. P. Furth, J. Killeen, and M. N. Rosenbluth. Finite-resistivity instabilities of a sheet pinch. *Phys. Fluids*, 6(4):459–484, 1963.

[17] B. Coppi, G. Laval, and R. Pellat. Dynamics of the geomagnetic tail. *Phys. Rev. Lett.*, 16(26):1207–1210, 1966.

[18] N. F. Loureiro, S. C. Cowley, W. D. Dorland, M. G. Haines, and A. A. Schekochihin. x-point collapse and saturation in the nonlinear tearing mode reconnection. *Phys. Rev. Lett.*, 95(23):235003, 2005.

[19] L. J. Chen, A. Bhattacharjee, P. A. Puhl-Quinn, H. Yang, N. Bessho, S. Imada, S. Muhlbachler, P. W. Daly, B. Lefebvre, Y. Khotyaintsev, A. Vaivads, A. Fazakerley, and E. Georgescu. Observation of energetic electrons within magnetic islands. *Nature Physics*, 4(1):19–23, 2008.

[20] J. Lin, J. Li, T. G. Forbes, Y. K. Ko, J. C. Raymond, , and A. Vourlidas. Features and properties of coronal mass ejection/flare current sheets. *Astrophys. J. Letters*, 658(2):L123–L126, 2007.

[21] W. Gekelman, H. Pfister, and J. R. Kan. Experimental observations of patchy reconnections associated with the three-dimensional tearing instability. *J. Geophys. Res.*, 96(A3):3829–3833, 1991.

[22] J. Birn, J. F. Drake, M. A. Shay, B. N. Rogers, R. E. Denton, M. Hesse, M. Kuznetsova, Z. W. Ma, A. Bhattacharjee, A. Otto, and P. L. Pritchett. Geospace Environmental Modeling (GEM) magnetic reconnection challenge. *J. Geophys. Res.*, 106(A3):3715–3719, 2001.

[23] W. Gekelman, R. L. Stenzel, and N. Wild. Magnetic field line reconnection experiments, 3. Ion acceleration, flows, and anomalous scattering. *J. Geophys. Res.*, 87(A1):101–110, 1982.

[24] Y. Ren, M. Yamada, S. Gerhardt, H. Ji, R. Kulsrud, and A. Kuritsyn. Experimental verification of the Hall effect during magnetic reconnection in a laboratory plasma. *Phys. Rev. Lett.*, 95(5):055003, 2005.

[25] C. D. Cothran, M. Landreman, M. R. Brown, and W. H. Matthaeus. Generalized Ohm's law in a 3-D reconnection experiment. *Geophys. Res. Lett.*, 32(3):L03105, 2005.

[26] A. G. Frank, S. G. Bugrov, and V. S. Markov. Hall currents in a current sheet: Structure and dynamics. *Phys. Plasmas*, 15(9):092102, 2008.

[27] M. Øieroset, T. D. Phan, M. Fujimoto, R. P. Lin, and R. P. Lepping. In situ detection of collisionless reconnection in the earth's magnetotail. *Nature*, 412(6845):414–417, 2001.

[28] R. G. Kleva, J. F. Drake, and F. L. Waelbroeck. Fast reconnection in high temperature plasmas. *Phys. Plasmas*, 2(1):23–34, 1995.

[29] O. Buneman. Instability, turbulence, and conductivity in current-carrying plasma. *Phys. Rev. Lett.*, 1(1):8–9, 1958.

[30] B. B. Kadomtsev. *Plasma Turbulence*. Academic Press, London, 1965.

[31] N. A. Krall and P. C. Liewer. Low-frequency instabilities in magnetic pulses. *Phys. Rev. A*, 4(5):2094–2103, 1971.

[32] J. D. Huba, N. T. Gladd, and K. Papadopoulos. The lower-hybrid-drift instability as a source of anomalous resistivity for magnetic field line reconnection. *Geophys. Res. Lett.*, 4(3):125–128, 1977.

[33] D. Biskamp and E. Schwarz. Localization, the clue to fast magnetic reconnection. *Phys. Plasmas*, 8(11):4729–4731, 2001.

[34] R. M. Kulsrud. Magnetic reconnection: Sweet-Parker versus Petschek. *Earth Planets Space*, 53(6):417–422, 2001.

[35] D. A. Uzdensky and R. M. Kulsrud. Two-dimensional numerical simulation of the resistive reconnection layer. *Phys. Plasmas*, 7(10):4018–4030, 2000.

[36] M. Ugai. Computer studies on powerful magnetic energy conversion by the spontaneous fast reconnection mechanism. *Phys. Plasmas*, 2(2):388–397, 1995.

[37] J. Drake, M. Swisdak, C. Cattell, M. Shay, B. Rogers, and A. Zeiler. Formation of electron holes and particle energization during magnetic reconnection. *Science*, 299:873–877, 2003.

[38] H. Ji, Y. Ren, M. Yamada, S. Dorfman, W. Daughton, and S. P. Gerhardt. New insights into dissipation in the electron layer during magnetic reconnection. *Geophys. Res. Lett.*, 35(13):L13106, 2008.

[39] W. Gekelman and R. L. Stenzel. Magnetic field line reconnection experiments, 6. Magnetic turbulence. *J. Geophys. Res.*, 89(A5):2715–2733, 1984.

[40] T. A. Carter, H. Ji, F. Trintchouk, M. Yamada, and R. M. Kulsrud. Measurement of lower-hybrid drift turbulence in a reconnecting current sheet. *Phys. Rev. Lett.*, 88(1):015001, 2001.

[41] T. A. Carter, M. Yamada, H. Ji, R. M. Kulsrud, and F. Trintchouk. Experimental study of lower-hybrid drift turbulence in a reconnecting current sheet. *Phys. Plasmas*, 9(8):3272–3288, 2002.

[42] H. Ji, S. Terry, M. Yamada, R. Kulsrud, A. Kuritsyn, and Y. Ren. Electromagnetic fluctuations during fast reconnection in a laboratory plasma. *Phys. Rev. Lett.*, 92(11):115001, 2004.

[43] M. Øieroset, R. P. Lin, T. D. Phan, D. E. Larson, and S. D. Bale. Evidence for electron acceleration up to ∼300 keV in the magnetic reconnection diffusion region of earth's magnetotail. *Phys. Rev. Lett.*, 89(19):195001, 2002.

[44] P. V. Savrukhin. Generation of suprathermal electrons during magnetic reconnection at the sawtooth crash and disruption instability in the T-10 tokamak. *Phys. Rev. Lett.*, 86(14):3036–3039, 2001.

[45] M. Brown, C. Cothran, M. Landreman, D. Schlossberg, W. Matthaeus, G. Qin, V. Lukin, and T. Gray. Energetic particles from three-dimensional magnetic reconnection events in the Swarthmore Spheromak Experiment. *Phys. Plasmas*, 9:2077, 2002.

[46] W. Gekelman and R. L. Stenzel. Measurement and instability analysis of three-dimensional anisotropic electron distribution functions. *Phys. Rev. Lett.*, 54(22):2414, 1985.

[47] W. Fox, M. Porkolab, J. Egedal, N. Katz, and A. Le. Laboratory observation of electron phase-space holes during magnetic reconnection. *Phys. Rev. Lett.*, 101(25):255003, 2008.

[48] M. C. Lee, R. J. Riddolls, K. D. Vilece, N. E. Dalrymple, M. J. Rowlands, D. T. Moriarty, K. M. Groves, M. P. Sulzer, and S. P. Kuo. Laboratory reproduction of Arecibo experimental results: HF wave-enhanced Langmuir waves. *Geophys. Res. Lett.*, 24(2):115–118, 1997.

[49] J. Egedal, A. Fasoli, and J. Nazemi. Dynamical plasma response during driven magnetic reconnection. *Phys. Rev. Lett.*, 90(13):135003, 2003.

[50] J. Egedal, W. Fox, M. Porkolab, and A. Fasoli. Eigenmode response to driven magnetic reconnection in a collisionless plasma. *Phys. Plasmas*, 12(5):052107, 2005.

[51] A. Stark, W. Fox, J. Egedal, O. Grulke, and T. Klinger. Laser-induced fluorescence measurement of the ion-energy-distribution function in a collisionless reconnection experiment. *Phys. Rev. Lett.*, 95(23):235005, 2005.

[52] J. Egedal, W. Fox, N. Katz, M. Porkolab, K. Reim, and E. Zhang. Laboratory observations of spontaneous magnetic reconnection. *Phys. Rev. Lett.*, 98(1):015003, 2007.

[53] A. Kesich, J. Bonde, J. Egedal, W. Fox, R. Goodwin, N. Katz, and A. Le. Magnetic flux array for spontaneous magnetic reconnection experiments. *Rev. Sci. Inst.*, 79(6):063505, 2008.

[54] I. H. Hutchinson. *Principles of Plasma Diagnostics*. Cambridge University Press, Cambridge, 2nd edition, 2002.

[55] F. F. Chen. Electric probes. In R. H. Huddlestone and S. L. Leonard, editors, *Plasma Diagnostic Techniques*, chapter 4. Academic Press, 1965.

[56] V. I. Demidov, S. V. Ratynskaia, and K. Rypdal. Electric probes for plasmas: The link between theory and instrument. *Rev. Sci. Inst.*, 73(10):3409–3439, 2002.

[57] F. W. Crawford and R. Grard. Low-frequency impedance characteristics of a Langmuir probe in a plasma. *J. App. Phys.*, 37(1):180–183, 1966.

[58] A. M. Pointu. A model of radio frequency planar discharges. *J. App. Phys.*, 60(12):4113–4118, 1986.

[59] A. M. Pointu. Dynamics of a rf sheath in the range between the ionic and the electronic plasma frequencies. *App. Phys. Lett.*, 50(6):316–317, 1987.

[60] J. D. Swift and M. J. R. Schwar. *Electrical Probes for Plasma Diagnostics*. American Elsevier, New York, 1969.

[61] R. Haug, M. Felden, and D. Schirmann. The grid probe as an ionic diagnostic tool in cesium plasma. *J. App. Phys.*, 39(10):4501–4508, 1968.

[62] S. G. Ingram, B. M. Annaratone, and M. Ohuchi. Design and use of a gridded probe in a low-pressure rf argon discharge. *Rev. Sci. Inst.*, 61(7):1883–1891, 1990.

[63] R. L. Stenzel, W. Gekelman, N. Wild, J. M. Urrutia, and D. Whelan. Directional velocity analyzer for measuring electron distribution functions in plasmas. *Rev. Sci. Inst.*, 54(10):1302–1310, 1983.

[64] G. Donoso and P. Martín. Grid effects on velocity analyzers of variable geometry. *Rev. Sci. Inst.*, 57(8):1501–1506, 1986.

[65] G. Donoso and P. Martín. Space-charge effects in a velocity analyzer of variable geometry. *Rev. Sci. Inst.*, 61(11):3381–3383, 1990.

[66] K. Shadman. Space charge effects downstream from an electric grid in magnetized plasma. *Phys. Plasmas*, 11(11):5075–5084, 2004.

[67] J. D. Jackson. *Classical Electrodynamics*. John Wiley & Sons, New York, 3rd edition, 1998.

[68] M. Mitchner and C. H. Kruger. *Partially Ionized Gases*. Wiley, New York, 1973.

[69] H. C. Straub, P. Renault, B. G. Lindsay, K. A. Smith, and R. F. Stebbings. Absolute partial and total cross sections for electron-impact ionization of argon from threshold to 1000 eV. *Phys. Rev. A*, 52(2):1115–1124, 1995.

[70] P. Helander and D. J. Sigmar. *Collisional Transport in Magnetized Plasmas*. Cambridge University Press, 2002.

[71] D. R. Lide, editor. *CRC Handbook of Chemistry and Physics*. CRC Press, Boca Raton, Florida, 83rd edition, 2002.

[72] M. Gryziński. Classical theory of atomic collisions. i. theory of inelastic collisions. *Phys. Rev. A*, 138(2A):A336–A358, 1965.

[73] H. Dreicer. Electron and ion runaway in a fully ionized gas. I. *Phys. Rev.*, 115(2):238–249, 1959.

[74] E. Gargioni and B. Grosswendt. Electron scattering from argon: Data evaluation and consistency. *Rev. Mod. Phys.*, 80(2), 2008.

[75] R. D. Dubois and M. E. Rudd. Absolute doubly differential cross sections for ejection of secondary electrons from gases by electron impact. ii. 100-500-eV electrons on neon, argon, molecular hydrogen, and molecular nitrogen. *Phys. Rev. A*, 17(3):843–848, 1978.

[76] T. H. Stix. *Waves in Plasmas*. Springer-Verlag, New York, 1992.

[77] H. G. Jenkins and D. G. Watts. *Spectral Analysis and Its Applications*. Holden-Day, San Francisco, 1968.

[78] W. H. Press, S. A. Teukolski, W. T. Vetterling, and B. P. Flannery. *Numerical Recipes in C*. Cambridge University Press, Cambridge, 2nd edition, 1992.

[79] A. B. Mikhailovskii. *Theory of Plasma Instabilities*, volume 1: Instabilities of a Homogeneous Plasma. Consultants Bureau, New York, 1974.

[80] P. M. Bellan and M. Porkolab. Experimental studies of lower hybrid wave propagation. *Phys. Fluids*, 19(7):995–1006, 1976.

[81] E. Ott, J. B. Mcbride, J. H. Orens, and J. P. Boris. Turbulent heating in computer simulations of the modified plasma two-stream instability. *Phys. Rev. Lett.*, 28(2):88–91, 1972.

[82] T. Chang and B. Coppi. Lower hybrid acceleration and ion evolution in the suprauroral region. *Geophys. Res. Lett.*, 8(12):1253–1256, 1981.

[83] R. L. Stenzel. Lower-hybrid turbulence in a nonuniform magnetoplasma. *Phys. Fluids B: Plasma Phys.*, 3(9):2568–2581, 1991.

[84] J. D. Huba, J. F. Drake, and N. T. Gladd. Lower-hybrid-drift instability in field reversed plasmas. *Phys. Fluids*, 23(3):552–561, 1980.

[85] S. Bale, F. Mozer, and T. Phan. Observation of lower hybrid drift instability in the diffusion region at a reconnecting magnetopause. *Geophys. Res. Lett.*, 29:2180, 2002.

[86] A. B. Mikhailovskii. *Theory of Plasma Instabilities*, volume 2: Instabilities of an Inhomogeneous Plasma. Consultants Bureau, New York, 1974.

[87] J. P. Freidberg and R. A. Gerwin. Lower hybrid drift instability at low drift velocities. *Phys. Fluids*, 20(8):1311–1315, 1977.

[88] B. D. Fried and S. D. Conte. *The Plasma Dispersion Function*. Academic Press, New York, 1961.

[89] B. Coppi, F. Pegoraro, R. Pozzoli, and G. Rewoldt. Slide-away distributions and relevant collective modes in high-temperature plasmas. *Nucl. Fusion*, 16(2):309–328, 1976.

[90] K. Papadopoulos and P. Palmadesso. Excitation of lower hybrid waves in a plasma by electron beams. *Phys. Fluids*, 19(4):605–606, 1976.

[91] B. H. Hui, N. K. Winsor, and B. Coppi. Collisional theory of electrical resistivity in trapped electron regimes. *Phys. Fluids*, 20(8):1275–1278, 1977.

[92] V. V. Parail and O. P. Pogutse. The kinetic theory of runaway electron beam instability in a tokamak. *Nucl. Fusion*, 18(3):303–314, 1978.

[93] S. C. Luckhardt, K. I. Chen, M. J. Mayberry, M. Porkolab, Y. Terumichi, G. Bekefi, F. S. Mcdermott, and R. Rohatgi. Particle confinement and the anomalous doppler instability during combined inductive and lower-hybrid current drive. *Phys. Fluids*, 29(6):1985–1993, 1986.

[94] M. Porkolab, V. Arunasalam, and R. A. Ellis. Parametric instability and anomalous heating due to electromagnetic waves in plasma. *Phys. Rev. Lett.*, 29(21):1438–1441, 1972.

[95] I. Bernstein, J. Greene, and M. Kruskal. Exact nonlinear plasma oscillations. *Phys. Rev.*, 108:546–550, 1957.

[96] H. Schamel. Electron holes, ion holes and double layers: Electrostatic phase space structures in theory and experiment. *Phys. Rep.*, 140(3):161–191, 1986.

[97] H. Matsumoto, H. Kojima, T. Miyatake, Y. Omura, M. Okada, I. Nagano, and M. Tsutsui. Electrostatic solitary waves (ESW) in the magnetotail: BEN wave forms observed by GEOTAIL. *Geophys. Res. Lett.*, 21(25):2915–2918, 1994.

[98] R. E. Ergun, C. W. Carlson, J. P. McFadden, F. S. Mozer, L. Muschietti, I. Roth, and R. J. Strangeway. Debye-scale plasma structures associated with magnetic-field-aligned electric fields. *Phys. Rev. Lett.*, 81(4):826, 1998.

[99] S. D. Bale, P. J. Kellogg, D. E. Larson, R. P. Lin, K. Goetz, and R. P. Lepping. Bipolar electrostatic structures in the shock transition region: Evidence of electron phase space holes. *Geophys. Res. Lett.*, 25(15):2929–2932, 1998.

[100] H. Matsumoto, X. H. Deng, H. Kojima, and R. R. Anderson. Observation of electrostatic solitary waves associated with reconnection on the dayside magnetopause boundary. *Geophys. Res. Lett.*, 30(6):1326, 2003.

[101] C. Cattell, J. Dombeck, J. Wygant, J. F. Drake, M. Swisdak, M. L. Goldstein, W. Keith, A. Fazakerley, M. Andrè, E. Lucek, and A. Balogh. Cluster observations of electron holes in association with magnetotail reconnection and comparison to simulations. *J. Geophys. Res.*, 110:A01211, 2005.

[102] K. V. Roberts and H. L. Berk. Nonlinear evolution of a two-stream instability. *Phys. Rev. Lett.*, 19(6):297, 1967.

[103] G. Manfredi. Long-time behavior of nonlinear Landau damping. *Phys. Rev. Lett.*, 79(15):2815, 1997.

[104] H. L. Berk, C. E. Nielsen, and K. V. Roberts. Phase space hydrodynamics of equivalent nonlinear systems: Experimental and computational observations. *Phys. Fluids*, 13(4):980–995, 1970.

[105] N. J. Zabusky and M. D. Kruskal. Interaction of "solitons" in a collisionless plasma and the recurrence of initial states. *Phys. Rev. Lett.*, 15(6):240, 1965.

[106] M. Goldman, D. Newman, and A. Mangeney. Theory of weak bipolar fields and electron holes with applications to space plasmas. *Phys. Rev. Lett.*, 99:145002, 2007.

[107] C. S. Ng and A. Bhattacharjee. Bernstein-Greene-Kruskal modes in a three-dimensional plasma. *Phys. Rev. Lett.*, 95(24), 2005.

[108] C. S. Ng, A. Bhattacharjee, and F. Skiff. Weakly collisional Landau damping and three-dimensional Bernstein-Greene-Kruskal modes: New results on old problems. *Phys. Plasmas*, 13(5):055903, 2006.

[109] K. Saeki, P. Michelsen, H. L. Pécseli, and J. J. Rasmussen. Formation and coalescence of electron solitary holes. *Phys. Rev. Lett.*, 42(8):501, 1979.

[110] J. P. Lynov, P. Michelsen, H. L. Pécseli, J. J. Rasmussen, K. Saeki, and V. A. Turikov. Observations of solitary structures in a magnetized, plasma loaded waveguide. *Physica Scripta*, 20(3-4):328–335, 1979.

[111] L.-J. Chen, D. J. Thouless, and J.-M. Tang. Bernstein-Greene-Kruskal solitary waves in three-dimensional magnetized plasma. *Phys. Rev. E*, 69(5):055401, 2004.

[112] L. J. Chen, J. Pickett, P. Kintner, J. Franz, and D. Gurnett. On the width-amplitude inequality of electron phase space holes. *J. Geophys. Res.*, 110:A09211, 2005.

[113] L. Muschietti, I. Roth, C. W. Carlson, and M. Berthomier. Modeling stretched solitary waves along magnetic field lines. *Nonlin. Processes Geophys.*, 9:101–109, 2002.

[114] M. Oppenheim, G. Vetoulis, D. L. Newman, and M. V. Goldman. Evolution of electron phasespace holes in 3D. *Geophys. Res. Lett.*, 28(9):1891–1894, 2001.

[115] D. L. Newman, M. V. Goldman, M. Spector, and F. Perez. Dynamics and instability of electron phase-space tubes. *Phys. Rev. Lett.*, 86(7):1239, 2001.

[116] L. Muschietti, I. Roth, C. Carlson, and R. Ergun. Transverse instability of magnetized electron holes. *Phys. Rev. Lett.*, 85:94–97, 2000.

[117] T. Miyake, Y. Omura, H. Matsumoto, and H. Kojima. Two-dimensional computer simulations of electrostatic solitary waves observed by Geotail spacecraft. *J. Geophys. Res.*, 103(A6):11841–11850, 1998.

[118] R. E. Ergun, C. W. Carlson, J. P. McFadden, F. S. Mozer, G. T. Delory, W. Peria, C. C. Chaston, M. Temerin, I. Roth, L. Muschietti, R. Elphic, R. Strangeway, R. Pfaff, C. A. Cattell, D. Klumpar, E. Shelley, W. Peterson, E. Moebius, and L. Kistler. FAST satellite observations of large-amplitude solitary structures. *Geophys. Res. Lett.*, 25(12):2041–2044, 1998.

[119] J. R. Franz, P. M. Kintner, and J. S. Pickett. Polar observations of coherent electric field structures. *Geophys. Res. Lett.*, 25(8):1277–1280, 1998.

[120] J. R. Franz, P. M. Kintner, J. S. Pickett, and L. J. Chen. Properties of small-amplitude electron phase-space holes observed by Polar. *J. Geophys. Res.*, 110:A09212, 2005.

[121] L. Dyrud and M. Oppenheim. Electron holes, ion waves, and anomalous resistivity in space plasmas. *J. Geophys. Res.*, 111:A01302, 2006.

[122] P. Guio, S. Børve, L. K. S. Daldorff, J. P. Lynov, P. Michelsen, H. L. Pécseli, J. J. Rasmussen, K. Saeki, and J. Trulsen. Phase space vortices in collisionless plasmas. *Nonlin. Processes Geophys.*, 10:75–86, 2003.

[123] J. D. Moody and C. F. Driscoll. Rarefaction waves, solitons, and holes in a pure electron plasma. *Phys. Plasmas*, 2(12):4482–4493, 1995.

[124] J. R. Danielson, F. Anderegg, and C. F. Driscoll. Measurement of Landau damping and the evolution to a BGK equilibrium. *Phys. Rev. Lett.*, 92(24):245003, 2004.

[125] D. S. Montgomery, J. A. Cobble, J. C. Fernández, R. J. Focia, R. P. Johnson, R. N. Legalloudec, H. A. Rose, and D. A. Russell. Recent Trident single hot spot experiments: Evidence for kinetic effects, and observation of Langmuir decay instability cascade. *Phys. Plasmas*, 9(5):2311–2320, 2002.

[126] T. Takeda and K. Yamagiwa. Dynamics of electron-beam holes induced by self-trapping. *Phys. Lett. A*, 339(1-2):118–122, 2005.

[127] V. Arunasalam, M. A. Heald, and J. Sinnis. Microwave scattering from unstable electron plasma waves. *Phys. Fluids*, 14(6):1194–1203, 1971.

[128] J. R. Franz, P. M. Kintner, C. E. Seyler, J. S. Pickett, and J. D. Scudder. On the perpendicular scale of electron phase-space holes. *Geophys. Res. Lett.*, 27(2):169–172, 2000.

[129] M. V. Goldman. Strong turbulence of plasma waves. *Rev. Mod. Phys.*, 56(4):709, 1984.

[130] M. Porkolab and M. V. Goldman. Upper-hybrid solitons and oscillating-two-stream instabilities. *Phys. Fluids*, 19(6):872–881, 1976.

[131] K. E. Lonngren. Soliton experiments in plasmas. *Plasma Phys.*, 25(9):943–982, 1983.

[132] H. Ikezi, P. J. Barrett, R. B. White, and A. Y. Wong. Electron plasma waves and free-streaming electron bursts. *Phys. Fluids*, 14(9):1997–2005, 1971.

[133] N. Dubouloz, R. Pottelette, M. Malingre, and R. A. Treumann. Generation of broadband electrostatic noise by electron acoustic solitons. *Geophys. Res. Lett.*, 18(2):155–158, 1991.

[134] J. A. Schmidt. High impedance Langmuir probes. *Rev. Sci. Inst.*, 39(9):1297–1299, 1968.

[135] R. E. Matick. *Transmission Lines for Digital and Communications Networks*. IEEE Press, New York, 1995.